Dissertation

submitted to the
Combined Faculties for the Natural Sciences and for Mathematics
of the Ruperto-Carola University of Heidelberg, Germany
for the degree of
Doctor of Natural Sciences

presented by

Diplom-Physicist Stefan Umbreit
born in: Rudolstadt/Schwarza, Thüringen

Oral examination: 29$^{\text{th}}$ June 2005

The Theory of the Formation of Brown Dwarfs

Referees: **Prof. Dr. Thomas Henning**
Priv. Doz. Dr. Andreas Just

Theory of the Formation of Brown Dwarfs

We investigate the dynamical decay of non-hierarchical accreting triple systems and its implications on the ejection model as Brown Dwarf formation scenario. A modified chain-regularization scheme is used to integrate the equations of motion, that also allows for mass changes over time as well as for momentum transfer from the accreted gas mass onto the bodies. We integrate an ensemble of triple systems within a certain volume with different accretion rates, assuming several prescriptions of how momentum is transferred onto the bodies. We follow their evolution until the systems have decayed. We find that the formation probability of Brown Dwarfs depends strongly on the assumed momentum transfer which is related to the motion of the gas. Due to ongoing accretion and consequent shrinkage of the systems, the median escape velocity is increased by a factor of 2 and the binary separations are decreased by a factor of 5 compared with non-accreting systems. Furthermore, the obtained semi-major axis distribution drops off sharply to either side of the median, which is also supported by observations. However, the disks around the ejected Brown Dwarfs seem to have too low accretion rates and masses to account for many of the observed disks in typical low-mass star-forming regions. We conclude that accretion of gas and the kinematic properties of the accreted gas during dynamical interactions strongly influence the abundance as well as the dynamical properties of Brown Dwarfs and, that the ejection scenario seems to be a promising scenario to produce both, very close Brown Dwarf binaries as well as single Brown Dwarfs, whereas it seems less likely to find very long-lived accretion disks around them.

Theorie der Enstehung Bauner Zwerge

Wir untersuchen den dynamischen Zerfall nicht-hierarchischer akkretierender Drei-Körper-Systeme und deren Bedeutung für das "Ejection Scenario" als Entstehungs-Szenario Brauner Zwerge. Die Bewegungsgleichungen werden mit einer modifizierten CHAIN-Regularisierungs-Methode integriert, die ebenfalls die Änderung der Masse der einzelnen Körper sowie den Impulstransport des akkretierten Gases auf die Körper berücksichtigt. Wir simulieren viele statistisch, innerhalb eines gewissen Volumens, erzeugte Drei-Körper-Systeme mit unterschiedlichen Akkretionsraten, wobei wir dabei unterschiedliche Möglichkeiten, wie das akkretierte Gas dessen Impuls auf die Körper überträgt, annehmen. Wir verfolgen die Entwicklung der Drei-Körper-Systeme bis sie zerfallen sind. Wir fanden, dass die Enstehungswahrscheinlichkeit Brauner Zwerge sehr stark abhängig ist vom angenommenen Impulsübertrag, der mit der Bewegung des Gases zusammenhängt. Wegen der permanenten Akkretion und der damit verbundenen Schrumpfung der Drei-Körper-Systeme, wurde im Vergleich mit nicht-akkretierenden Systemen der Median der Entweichgeschwindigkeiten um einen Faktor 2 vergrössert und die Abstände der Doppelsysteme um einen Faktor 5 verringert. Desweiteren fanden wir heraus, dass die erhaltene Bahn-Halbachsen-Verteilung sehr steil zu beiden Seiten des Median abfällt, was auch mit entsprechenden Beobachtungen übereinstimmt. Jedoch finden wir auch, dass die Akkretionsscheiben um unsere Braunen Zwerge zu geringe Massen und Akkretionsraten aufweisen, um viele der beobachteten Scheiben in typischen Entstehungsregionen von Sternen mit niedriger Masse zu erklären. Wir kommen zu dem Schluss, dass die Gasakkretion und die kinematischen Eigenschaften des akkretierten Gases während der dynamischen Wechselwirkung sehr stark die Häufigkeit als auch die dynamischen Eigenschaften der Braunen Zwerge beeinflusst, und, dass das "Ejection Scenario" ein vielversprechenden Modell ist, dass sowohl sehr enge Doppelsysteme als auch viele einzelne Braune Zwerge erzeugen kann, während es eher unwahrscheinlich ist, dass man um diese herausgeschleuderten Braunen Zwerge Akkretionsscheiben mit grosser Lebensdauer finden kann.

Contents

Chapter 1

Introduction

Since their first detection 10 years ago (Nakajima et al., 1995) many Brown Dwarfs have been detected ever since (e.g. Basri, 2000). Brown Dwarfs, known as 'failed stars' which have not enough mass to start hydrogen burning as in normal stars, were found at many different star-formation sites such as Taurus (Briceño et al., 2002), Orion (e.g. Muench et al., 2002; Béjar et al., 1999), Ophiuchus (e.g. Allen et al., 2002), and the Chamaeleon cloud (e.g. López Martí et al., 2004; Comerón et al., 2000), as cluster members (Moraux et al., 2002; Bouvier et al., 1998; Martín et al., 1998) and as free-floating objects (Kirkpatrick et al., 1999, 2000). Based on the frequency of detection it is widely believed that they should be as common as low-mass stars. In addition to their similar abundance many of them also show accretion features similar to ordinary TT stars and it was even possible to detect circumstellar disks around them (Jayawardhana et al., 2003; Pascucci et al., 2003; Klein et al., 2003; Apai et al., 2002; Natta & Testi, 2001). Also some of them are known to form binary and higher order systems (Bouy et al., 2003).

Based on these results it is tempting to claim that Brown Dwarfs may have been formed like ordinary low mass TT stars. In this picture it is assumed that the collapse of a gravitationally unstable molecular cloud core forms a single object (see e.g. Shu, 1977), or perhaps a small multiple system, but the final mass of the object is primarily dependent on the mass of the pre-stellar core. From this it would follow that stars form from the collapse of higher-mass molecular cloud cores, while Brown Dwarfs form from very dense low-mass ones. This idea is also consistent with observations of Motte et al. (1998), who found that there is a striking similarity between the distribution of core masses and the distribution of stellar masses in the ρ Ophiuchus molecular cloud. In addition, as such objects are surrounded by accretion disks (see e.g. Lin & Pringle (1990)), the accretion features of Brown Dwarfs, i.e. mainly Hα emission, are readily accounted for. It should be, therefore, no surprise that these accretion features seem to vanish after the same time as in T Tauri stars (see e.g. Liu et al. (2003)), although it is certainly not a strong argument for a T Tauri-like formation of Brown Dwarfs, given the complex physics of circumstellar disks.

Indeed most of the observed properties of Brown Dwarfs can be understood by assuming that Brown Dwarfs form like T Tauri stars. The only feature that lacks a clear understanding are

the properties of Brown Dwarf binaries. Kroupa et al. (2003) argue that if Brown Dwarfs are formed like low-mass stars they should have the same pairing statistics and binary properties, scaled down to the substellar regime. On the contrary, from recent surveys of Close et al. (2003), Gizis et al. (2003), Bouy et al. (2003) and Martín et al. (2003), as well as from the model calculation of the standard star-formation scenario of Kroupa et al. (2003), it has been found that the observed properties of Brown Dwarf binaries are not a natural extension of the trends seen among stars with decreasing primary mass. Therefore Kroupa et al. (2003) come to the conclusion that Brown Dwarfs may not be formed with the same scaled down properties as stars and further infer that, in order to form Brown Dwarfs, their accretion phase must be interrupted by other (external) processes. Which process this actually can be is currently under vivid debate.

Reipurth & Clarke (2001) suggested that the ejection of fragments from unstable multiple systems out of their surrounding molecular cloud may lead to an early end of the accretion process of the fragments and, consequently, leave some of them substellar. This formation scenario is constantly challenged by observational studies (Briceño et al., 2002; Natta & Testi, 2001). They argue that because accretion features are observed around objects with an age of up to 10 Myr, which is about the lifetime of disks around T Tauri stars, close collisions, required for the ejection of fragments, cannot have happened as they tend to truncate the disks, severely limiting their lifetime, which in turn should make the frequency of detection much lower than actually observed. On the other hand the amount of material that is stripped off the disk is also sensitive to the eccentricity of the perturber orbit. For instance strongly hyperbolic encounters are known to be much less destructive than parabolic ones which are assumed to be the most likely encounter orbit in larger clusters (Ostriker (1994); Larson (1990)). For accreting small-N clusters the encounter parameters are not well known and certainly need to be studied in greater detail. Based on these uncertainties, we belive that the ejection scenario cannot be ruled out completely but needs more accurate modeling in order to provide better predictions.

It is therefore our aim to explore under which conditions Brown Dwarfs form in accreting triple systems and derive statistics of escaping Brown Dwarfs and binaries which can then be compared to observations. For this we further investigate the ejection scenario by means of N-body calculations where the bodies are gaining mass according to a given accretion rate. In order to address the problem of the life-time of Brown Dwarf disks we also carry out simulations of disk collisions in such decaying accreting triple systems that produce Brown Dwarfs by ejection and can then compare our results with observations. From these simulations we can also make predictions about the disk masses and surface density profiles, which can then be used to further constrain possible formation scenarios by observations.

In Chapter 2 we give a brief overview of the existing Brown Dwarf formation scenarios. In Chapter 3 we explain the method which allows us to investigate decaying accreting triple systems numerically. We will then apply this method in Chapter 4 to obtain statistics of ejected Brown Dwarfs and Brown Dwarf binaries in dependence of the initial conditions and accretion prescriptions. From these results we will find initial conditions that produce binary Brown Dwarf properties which are in agreement with observations. We, therefore, use these initial conditions for our further modeling of disk collisions in accreting triple systems and follow the further evolution of such highly perturbed disks by means of hydrodynamical simulations in

Chapter 5. From the results we can finally draw some first conclusions about the expected life-time, mass, and surface density profile of the disks around the ejected Brown Dwarfs. Our main results are then summarized and discussed in Chapter 6.

Chapter 2

Brown Dwarf Formation Scenarios

This chapter gives a brief summary of some of the ideas that have been suggested on how Brown Dwarfs can be formed.

2.1 The Photo-Erosion model

It has been suggested that the strong, ionizing UV radiation of hot O and B stars might be responsible for the increased number of Brown Dwarfs in Orion (Kroupa & Bouvier, 2003). The basic mechanism is laid out in Whitworth & Zinnecker (2004) and the following summary can also be found in Whitworth & Goodwin (2005). This model starts with a standard pre-stellar core, which would, if it remains undisturbed, form an intermediate- or high-mass star. As this core is overrun by the hot ionizing radiation of a massive star, an ionization front starts to propagate into the core, 'photo eroding' it. At the same time a compression wave is launched in front of the ionization front. When the compression wave reaches the center, a protostar is created, which then grows by accretion. At the same time an expansion wave is reflected and propagates outwards, setting up the inflow which feeds accretion onto the central star. The outward propagating expansion wave soon meets the inward propagating ionization front, and shortly thereafter the ionization front find itself ionizing gas which is too tightly bound to the protostar that it cannot be unbound by the act of ionization. All the material that was within the ionization front at this time ends up in the protostar. On the basis of a simple semi-analytic treatment, Whitworth & Zinnecker (2004) show that the final mass is given by

$$M \simeq 0.01\mathrm{M}_{\odot} \left(\frac{a_I}{0.3\mathrm{km\,s^{-1}}}\right)^6 \times \left(\frac{\dot{\aleph}_{\mathrm{LyC}}}{10^{50}\mathrm{s^{-1}}}\right)^{-1/3} \left(\frac{n_0}{10^3\mathrm{cm^{-3}}}\right)^{-1/3},$$

where a_I is the isothermal sound speed in the neutral gas of the core, $\dot{\aleph}_{\mathrm{LyC}}$ is the rate at which the star(s) exciting the HII region emit hydrogen-ionizing photons, and n_0 is the density in the ambient HII region. The Brown Dwarfs formed in this way are likely to be single and should have no difficulty retaining a disk (Whitworth & Goodwin, 2005).

This mechanism is quite effective, as it produces Brown Dwarfs for a wide range of conditions. However, for low-mass star forming regions harboring Brown Dwarfs, like the Chamaeleon cloud, there must be a different process at work because of the generally low abundance of higher mass stars and because it is expected that photo evaporation is only efficient in the vicinity of massive stars (Kroupa & Bouvier, 2003).

2.2 Fragmentation of a Massive Disk

It has been suggested, by many different authors, that substellar objects can be formed by fragmentation of massive circumstellar disks (Lin et al., 1998; Boss, 2001; Boffin et al., 1998; Watkins et al., 1998a,b; Pickett et al., 2000). However, as far as single isolated disks are concerned, the question whether they will fragment is not easily answered. From simulations of Pickett et al. (2000) it became clear that only under idealized conditions, where the disk is assumed to be locally isothermal implying extremely efficient cooling, the disk disrupted and formed low-mass fragments. However, thermal and tidal effects prevented permanent condensations to form in massive disks, despite the vigorous growth of the spiral instabilities. For older, larger but less massive protostellar disks they find that only if the expansion of the disk in response to gravitational instabilities is restricted, long-lived condensations form. Furthermore, they find that a more realistic adiabatic evolution leads to vertical and radial expansion of the disk but no clump formation. It seems therfore unlikely that the fragmentation of an isolated massive disk is an efficient way to produce Brown Dwarfs.

However, if a massive protostellar disk interacts impulsively with another disk, or with a naked star, then it can be launched directly into the non-linear regime of gravitational instability and fragmentation is then much more likely, as simulations of Boffin et al. (1998), Watkins et al. (1998a,b) and Lin et al. (1998) suggest. Such interactions could be quite frequent in the dense proto-cluster environments where stars are born (Bate et al., 2002a, 2003). According to the calculations of Boffin et al. (1998) and Watkins et al. (1998a,b), the impulsively triggered fragmentation of disks seems to be a good mechanism to produce Brown Dwarf companions, provided the effective shear viscosity is high enough.

In the simulations of Bate et al. (2002a) and also in the collapse calculations of molecular cloud cores of Lang (2003) such a collision produced much more companions initially, which then became unbound from the central star because of gravitational interaction with the other fragments in the disk. This way it was also possible to form single free-floating Brown Dwarfs. As their simulations further show, this scenario is able to explain the increased number of low-mass Brown Dwarfs with a mass at around $0.02 M_{\odot}$ as reported by Lada & Lada (2003).

It, therefore, appears that collisions with massive disks and the subsequent disk fragmentation is a very promising scenario to produce single Brown Dwarfs as well as Brown Dwarfs companions to stars. In addition, it should be also possible that the Brown Dwarf companions can have disks. However, it seems less likely that the single ejected Brown Dwarfs possess disks with long life-times, as these must also have suffered a more or less close collision similar as in the ejection scenario of Reipurth & Clarke (2001), but further modeling of such perturbed disks is required to justify this assumption.

2.3 Opacity-limited Fragmentation in a Shock Compressed Layer

An efficient way to form very low-mass objects is by the fragmentation of a two-dimensional shock-compressed layer, as found by Boyd & Whitworth (2005). The following summary follows closely the one given in Whitworth & Goodwin (2005).

The fragmentation of a two-dimensional shock-compressed layer is more relevant to the contemporary picture of 'star-formation in a crossing time' as presented, e.g. in Elmegreen (2000). In this picture star-formation occurs in molecular clouds wherever two or more turbulent flows of sufficient density collide with sufficient ram pressure to produce the shock-compressed layer out of which pre-stellar cores can condense. This 2D fragmentation has the advantage that the fastest-condensing fragment has finite size, that is, smaller or faster fragments condense out on larger time-scales. In the model of Boyd & Whitworth (2005) the continuing inflow of matter into the fragment is also taken into account, which allows to identify the smallest fragment which can cool radiatively fast enough to dispose both the work being done by compression of the fragment, and the energy being dissipated at the accretion shock. They find that for shocked gas with a temperature of ~ 10K and no turbulence, i.e. the velocity dispersion of the gas is equal to the isothermal sound speed, $0.2\mathrm{km\,s^{-1}}$, the smallest fragment that can condense out has a mass less than $0.003\mathrm{M}_\odot$, and fragments with masses below $0.005\mathrm{M}_\odot$ condense out for a wide range of pre-shock densities and shock speeds.

The efficient and fast formation of such very low-mass fragments makes this model the primary choice for the explanation of free-floating planetary mass objects found in surveys of young cluster (e.g. Zapatero Osorio et al., 2002). However, to account for the properties of more massive Brown Dwarfs these condensations need to be followed further, which requires some additional modeling efforts.

2.4 Brown Dwarf Formation by Supersonic Turbulence in Molecular Clouds

Padoan & Nordlund (2004) suggest that Brown Dwarfs are formed directly by the process of turbulent fragmentation. They described this process as follows: The gas densities and velocity fields in star-forming clouds are highly non-linear because of the presence of supersonic turbulence. The turbulent kinetic energy is typically 100 times larger than the gas thermal energy, and the gas is roughly isothermal, so that very large compressions due to a complex network of interacting shocks cannot be avoided. Dense cores of any size can be formed in the turbulent flow, independent of the Jeans mass. Those cores that are massive and dense enough to be larger than their Jeans mass collapse into protostars, while smaller subcritical ones reexpand into the turbulent flow.

Based on a simple model of Padoan & Nordlund (2002) the authors are able to relate the power spectrum of the turbulence, which is a power-law, to the distribution of the core masses. The core mass distribution then turns out to be a power-law that is close to the Salpeter stellar initial mass function (IMF) (Salpeter, 1955) if the power-law index β of the power spectrum

is chosen as in Boldyrev et al. (2002) with $\beta = 1.74$. This value is also consistent with the observed velocity dispersion-size Larson relation (Larson, 1981). Since massive cores are usually larger than their Jeans mass, we can expect that the high-mass end of the core mass distribution also represents the the mass distribution of the collapsing cores.

On the other hand, for low-mass cores the probability of the cores to be dense enough to collapse is determined by the statistical distribution of core density. In order to compute the collapse probability of low-mass cores the authors assume that the distribution of core density can be approximated by the log-normal probability density function of the turbulent gas density and that the core densities and masses are statistically independent. Because of the nature of the log-normal probability distribution function, even very small substellar cores have a finite chance to be dense enough to collapse. This probability increases with increasing Mach number. Therefore, we will get more Brown Dwarfs relative to stars in molecular clouds with a stronger turbulent velocity field.

The resulting mass distribution of collapsing cores is found to be a power-law for masses larger than $1M_{\odot}$ when typical parameters for molecular clouds are used. At smaller masses the mass distribution flattens, reaches a maximum at a fraction of a solar mass, and then decreases with decreasing stellar mass. For plausible values of the Mach number and gas density that should be appropriate for dense cluster-forming regions inside molecular cloud complexes, Padoan & Nordlund (2004) find very good agreement of their stellar mass function with the IMF of the young star-forming cluster IC348 observed by Luhman et al. (2003). The model is also able to explain the very different abundances of Brown Dwarfs relative to stars in Taurus and Orion, if the turbulent velocity dispersion or the average gas density in Taurus is decreased by a factor of 2 relative to Orion. Such a decrease is also consistent with the lower velocity dispersion and density found in Taurus compared to Orion (Padoan & Nordlund, 2004).

However, apart from predicting the overall abundance and general form of the IMF, this model cannot make any further predictions about the properties of Brown Dwarfs, like kinematics and multiplicity.

2.5 Brown Dwarfs by Ejection

The basic idea behind the ejection scenario is that protostars are born primarily in groups and clusters and gravitational interactions in these dense systems may significantly influence, if not completely determine, the final stellar and substellar mass spectrum (Klessen, 2001; Bonnell et al., 1997, 2001). The underlying mechanism is, that the ejection of some cluster members out of their surrounding cloud core, that is caused by the decay of the non-hierarchical multiple system they initially form in, reduces, if not inhibits, the further accretion of those objects, thereby limiting their mass. In this picture the final mass of an object is correlated with the time it is bound to its parent cluster, a correlation that was also recently found by Bate & Bonnell (2004) in their simulation of large fragmenting molecular clouds. Thus it follows, that in order to form Brown Dwarfs they must be ejected early in order to stop the accretion process duly.

Such dynamical interactions between pre-stellar objects are generally thought to play an important role during the earliest stages of star-formation. It has been shown that the dynamical decay of bound, non-hierarchical, small-N multiple systems is able to explain the reduction of the mean distances between pre-stellar objects from typically a few 100AU, at a time they start to fragment out of their parental molecular cloud core, down to the typical distances of pre-stellar and stellar binaries of a few 10AU (Sterzik & Durisen, 1998; van Albada, 1968). From an observational point of view it as been argued for a long time that stars frequently form in clusters which then disperse within a few dynamical time scales (Zinnecker et al., 1993). This is also supported by direct detections of very young and dense small-N clusters (Lada & Lada, 1991) and by the fact that in star-forming regions the fraction of binaries and bound multiple systems decreases rapidly with time, implying significant orbital evolution during the formation process (Lada & Lada, 1991). On the theoretical side, Burkert & Bodenheimer (1993), Burkert et al. (1997) and many more have demonstrated that the fragmentation of a turbulent cloud core leads almost always to the formation of multiple fragments in a non-hierarchical, unstable configuration that decays after some crossing times, confirming these assumptions.

Therefore, it seems that the assumed initial conditions for the ejection scenario, consisting of compact non-hierarchical small-N cluster, are frequently met in the earliest stages of star-formation, making it rather likely for an early ejection to occur. However, the theoretical predictions of the ejection model are so far either only qualitatively given, as the prediction of disk sizes and life-times (Reipurth & Clarke, 2001), or if quantitatively then with rather low statistics, as the binary fractions and separations (Bate et al., 2003; Delgado-Donate et al., 2003, 2004; Bate & Bonnell, 2004), with the exception of the substellar IMF (Padoan & Nordlund, 2004; Delgado-Donate et al., 2004; Bate & Bonnell, 2004).

This gave us the motivation to investigate the ejection scenario by means of statistical N-body experiments with the focus on Brown Dwarf disk and binary properties.

Chapter 3

The Numerical Treatment of the Few-Body Problem

In this chapter we want to briefly outline the numerical techniques that are necessary to investigate strongly interacting, non-hierarchical few-body systems. Most of the following discussion is based on the theory as presented by Stiefel & Scheifele (1971), whereas for the description of the CHAIN-algorithm we follow closely Mikkola & Aarseth (1990) and Mikkola & Aarseth (1993).

3.1 Regularization of the Newtonian Equations of Motion in the Two-Body Problem

Numerical calculations of gravitationally, strongly interacting point-masses were always challenged because as soon as two bodies get very close to each other, usually called a near collision, large gravitational forces arise and their orbits are sharply bent. During a numerical integration the only way to overcome this difficulty is to use a small step length and many steps of integration during the phase of close approach. Because of truncation and round-off errors the numerical precision after near collision will be rather poor.

These difficulties are related to the singularity of the Newtonian potential at the positions of the gravitating masses, characterized by the occurrence of infinite velocities. We are thus interested in transforming the singular differential equations into regular ones, and we call this procedure regularization.

In the following discussion we consider the two-body motion in the center of mass frame, which allows us to write the equations of motion as

$$\frac{d\vec{v}}{dt} = \frac{K}{r^2}\frac{\vec{r}}{r} \tag{3.1}$$

with $\vec{v} = \vec{v_1} - \vec{v_2}$, $\vec{r} = \vec{r_1} - \vec{r_2}$, $r = |\vec{r}|$, $K = G(M_1 + M_2)$, where $\vec{v_{1,2}}$, $\vec{r_{1,2}}$ and $M_{1,2}$ are the velocities, position vectors and masses of the two bodies respectively, and G is the constant of gravity.

3.1.1 One-Dimensional Motion

The essential steps in order to transform the Newtonian equations into non-singular differential equations can be best described if we restrict the motion of the particles to one dimension. Obviously, under such circumstances the particles do collide with each other, provided their velocities are not always directed away from each other. By assuming, $r \geq 0$ the equations of motion and the energy $-h_k$ can be written as

$$\frac{dv}{dt} + \frac{K}{r^2} = 0, \qquad \frac{K}{r} - \frac{1}{2}v^2 = h_k \tag{3.2}$$

and h_k is a constant.

3.1.1.1 First step of regularization

Our first aim is to obtain regular functions describing the motion. The basic idea for performing this, is to compensate for the infinite increase of the velocity at collision by multiplying v with an appropriate scaling factor which vanishes at collision. Such a factor is the distance r itself. A new independent variable s is adopted such that the velocity with respect to s is rv or

$$\frac{dr}{ds} = r\frac{dr}{dt}\,. \tag{3.3}$$

Consequently the new variable s, called fictitious time, is defined by

$$dt = r\,ds.$$

Transformation from ordinary to fictitious time is performed by

$$\frac{d}{dt} = \frac{1}{r}ds,$$

$$\frac{d^2}{dt^2} = \frac{r\frac{d^2}{ds^2} - \frac{dr}{ds}\frac{d}{ds}}{r^3}.$$

The equations 3.2 of motion and of energy are thus transformed into

$$rr'' - r'^2 + Kr = 0 \tag{3.4}$$

$$r'^2 = 2\left(Kr - h_k r^2\right) \tag{3.5}$$

where a prime indicates differentiation with respect to s. The latter relation implies $x'(0) = 0$ at collision.

3.1.1.2 Second Step of Regularization

The equation 3.4 of motion is still singular as can be seen by rewriting it as

$$r'' = \frac{r'^2}{r} - K\,.$$

At collision the right hand side appears in the undetermined form $\left(\frac{0}{0} - K\right)$. However, if we insert equation 3.5 into 3.4, giving the result

$$r" + 2h_k r = K\,, \tag{3.6}$$

we obtain an elementary differential equation that is perfectly regular.

3.1.1.3 The Harmonic Oscillator

After the second step of regularization we introduce a new coordinate u defined by

$$r = u^2. \tag{3.7}$$

For the one-dimensional example this is not really necessary as we already obtained a regular differential equation of motion. However, for the three-dimensional motion a similar coordinate transformation is necessary to lead to success. If the transformation 3.7 is substituted into the energy equation 3.5 the differential equation

$$2u'^2 = K - h_k u^2 \tag{3.8}$$

is obtained and by using this result the equation 3.4 of motion are transformed into

$$u" + \frac{h_k}{2} u = 0\,. \tag{3.9}$$

For a positive value of h_k this is the differential equation of a harmonic oscillator with the frequency $\sqrt{\frac{h_k}{2}}$. For any value of h_k the nonlinear problem 3.2 of Kepler motion is now reduced to the linear differential equation 3.9.

3.1.2 Generalization to Three-Dimensional Motion

We introduce a fictitious time s analogous to the one-dimensional case with the same transformation as in equation 3.3, noting now that $r = |\overrightarrow{r}|$, i.e. r is the three-dimensional distance between the bodies. Using this fictitious time s as independent variable the equations 3.1 of motion become

$$r\overrightarrow{r}" - r'\overrightarrow{r}' + K\overrightarrow{r} = 0\,, \tag{3.10}$$

where $t' = r$. By taking into account the relation

$$v^2 = (\overrightarrow{v}, \overrightarrow{v}) = \frac{1}{r^2}(\overrightarrow{r}', \overrightarrow{r}') = \frac{1}{r^2}\left|\overrightarrow{r}'\right|^2\,,$$

the energy equation may be written

$$h_k = \frac{K}{r} - \frac{1}{2r^2}\left|\overrightarrow{r}'\right|^2\,.$$

The original equations of motion 3.1 form a system of three differential equations for the unknown components r_x, r_y, r_z in cartesian coordinates as functions of t. The total order is

six. These equations are replaced by the system 3.10 for the unknowns t, r_x, r_y, r_z as functions of s and the total order is seven. Thus we should always consider the ordinary time t as a fourth coordinate of the particles to be determined during the motion. Similar to the one-dimensional case, the equation 3.10 is still singular and needs to be regularized. In the one-dimensional case we performed this by inserting into the corresponding equation of motion the energy equation, but in the three-dimensional case at hand this does not lead us anywhere. As it turns out, we first have to apply a coordinate transformation similar to 3.7 and then need to write the energy equation and the equations of motion with the new coordinate $\vec{u}$ before we can substitute them into each other.

A suitable coordinate transformation has been found by Kustaanheimo & Stiefel (1965) and can be written in matrix notation as

$$\overrightarrow{r} = L(\overrightarrow{u})\,\overrightarrow{u} \tag{3.11}$$

with

$$L(\overrightarrow{u}) = \begin{pmatrix} u_1 & -u_2 & -u_3 & u_4 \\ u_2 & u_1 & -u_4 & -u_3 \\ u_3 & u_4 & u_1 & u_2 \\ u_4 & -u_3 & u_2 & -u_1 \end{pmatrix} \tag{3.12}$$

where $\vec{u}$ is now a four dimensional vector. Here we want to note that we used the convention that a physical vector (r_x, r_y, r_z) is automatically supplemented to a 4-vector $\overrightarrow{r}$ by adding a fourth component of value zero. Equation 3.11 is called the KS-transformation. This matrix has the following important properties:

1. $L(\overrightarrow{u})$ is orthogonal
$$L^T(\overrightarrow{u})L(\overrightarrow{u}) = rE$$
with L^T being L transposed and E being the unity matrix.

2. The elements of $L(\overrightarrow{u})$ are linear and homogeneous functions functions of the components u_i thus
$$L(\overrightarrow{u})' = L(\overrightarrow{u}')$$
where the prime denotes differentiation with respect to s.

3. The first column of $L(\overrightarrow{u})$ is the position vector $\overrightarrow{u}$.

4. When two vectors $\overrightarrow{u}, \overrightarrow{v}$ satisfy the bilinear relation
$$u_4v_1 - u_3v_2 + u_2v_3 - u_1v_4 = 0$$
then
$$L(\overrightarrow{u})\,\overrightarrow{v} = L(\overrightarrow{v})\,\overrightarrow{u}\,.$$

From these properties it follows that

$$r' = 2L(\overrightarrow{u})\,\overrightarrow{u}'\,. \tag{3.13}$$

Without going into the detailed derivation of the corresponding energy equation and equations of motion written in terms of the new variable $\vec{u}$, we simply give them here and refer to Stiefel & Scheifele (1971) for a thorough derivation. The energy relation reads

$$h_k = \frac{K - 2\,|\overrightarrow{u}'|^2}{|\overrightarrow{u}|^2}$$

and the equations of motion become

$$\overrightarrow{u}'' + \frac{\frac{K}{2} - (\overrightarrow{u}', \overrightarrow{u}')}{(\overrightarrow{u}, \overrightarrow{u})}\,\overrightarrow{u} = 0$$

which finally leads through substitution to the regularized equations

$$\overrightarrow{u}'' + \frac{h_k}{2}\overrightarrow{u} = 0\,. \tag{3.14}$$

These regularized equations of motion then need to be accompanied by the equation for the physical time to completely determine the solution

$$t' = (\overrightarrow{u}, \overrightarrow{u})\,. \tag{3.15}$$

If we also consider external perturbations, e.g. perturbations of a third body, the right hand side of equation 3.14 is no longer zero and equation 3.16 becomes instead

$$\overrightarrow{u}'' + \frac{h_k}{2}\overrightarrow{u} = \frac{|\overrightarrow{u}|^2}{2}\left(-\frac{1}{2}\frac{\partial V}{\partial \overrightarrow{u}} + L^T(\overrightarrow{u})\overrightarrow{F}\right) \tag{3.16}$$

where we have splitted the perturbing force into a part that can be described as a derivative from a perturbing potential $V(t, \overrightarrow{r})$ and another force $\overrightarrow{F}$ that does not have a potential. In this case, equations 3.16 and 3.15 need to be accompanied by the equation for the energy

$$h_k' = \left(\frac{\partial V}{\partial \overrightarrow{u}}\,,\,\overrightarrow{u}'\right) - 2\left(\overrightarrow{u}'\,, L^T\overrightarrow{F}\right)\,.$$

We thus arrived from the singular three-dimensional Newtonian equations of total order six to the regularized equations of total order ten.

3.2 Multiple Regularization

In the preceding section we have considered the regularization of the equations of motion of two bodies and also gave an expression for the treatment of the perturbed two body motion. Here, it is important to note that these perturbations are not formally required to be small, but can be arbitrarily large. However, for large perturbations the regularized time step is required to be sufficiently small. This can, in extreme cases, counterbalance the gain in accuracy we achieved by introducing the regularized equations of motion, as the influence of round-off errors, because of the greater number of time steps, increases. If this perturbation is due to a third body, this

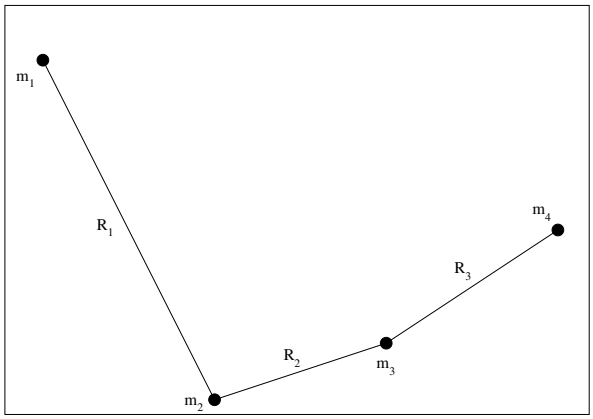

Figure 3.1: A four-particle regularization chain, where R_1, R_2, R_3 are the interparticle distances and m_1, m_2, m_3, m_4 are the masses of the bodies.

problem can be avoided by selecting a new regularized pair which incorporates the perturber. However, for bound triple systems we want to investigate here, the complicated nature of the motion of closely interacting triple systems would make it then necessary to frequently select a new pair during the integration, involving many transformations from regularized coordinates to physical ones and vice versa. These additional transformations during the integration will, once again, lead to a loss off accuracy by introducing further round-off errors and will also degrade the efficiency of the algorithm.

Therefore, it is desirable to find a way to avoid frequent switching of the dominant interacting pair, which led to the introduction of multiple regularization methods. By multiple regularization it is understood that at least two separations in a compact multiple system are treated specially to remove the two-body singularity. The method we used for our few-body experiments is the so called 'chain'-method and is presented in the following sections.

3.2.1 The Chain Regularization

The main principle of the chain method is based on the observation that in an N-body system we can make a chain of interparticle vectors such that all the bodies are connected. Subsequently all the interactions included in this vector chain can be regularized. An example of such a chain is given in Fig. 3.1. The chain is constructed in such a way as to include the smallest interparticle distances and, thus, the dominant two-body forces, while the other less dominant contributions are left in their singular form. Here we only want to briefly outline the basic steps required to obtain the equations of motion in the new chain coordinates and refer the reader to Mikkola & Aarseth (1993) for the full and rather complex expressions.

We obtain the equations of motion in terms of the regularized chain variables from the original ones by a canonical transformation. For this we consider the N-body Hamiltonian

$$H = \sum \frac{1}{2m_i} |\overrightarrow{p_i}|^2 - \sum_{i \neq j} \frac{m_i m_j}{|\overrightarrow{r_i} - \overrightarrow{r_j}|} = T - U$$

where $\overrightarrow{p_i}$ and $\overrightarrow{r_i}$ are the physical momenta and coordinates of the mass-points m_i, and T and U are the kinetic energy and the negative of the potential energy respectively. Here, and subsequently, we use units in which the gravitational constant $G = 1$ and assume that the frame of reference is that of the center of mass. Furthermore we only consider the case of an unperturbed Hamiltonian, as in this thesis we did not consider any external perturbations.

After selecting the chain vectors connecting the N mass points, we relabel these points 1, 2, ..., N along the chain as shown in Fig. 3.1. The next step is to adopt the new canonical coordinates

$$\begin{aligned} \vec{R}_1 &= \vec{r}_2 - \vec{r}_1, \\ \vec{R}_2 &= \vec{r}_3 - \vec{r}_2, \\ &\vdots \\ \vec{R}_{N-1} &= \vec{r}_N - \vec{r}_{N-1} \end{aligned} \tag{3.17}$$

while the corresponding canonical momenta $\overrightarrow{W}_i$ are related to old momenta $\vec{p}_i$ by the generating function

$$S = \sum_{i=1}^{N-1} \overrightarrow{W}_i \cdot (\vec{r}_{i+1} - \vec{r}_i)$$

which gives the old momenta in terms of the new ones by $\vec{p}_i = \partial S / \partial \vec{r}_i$. Thus, the relative momentum vectors $\overrightarrow{W}_i$ are obtained recursively by

$$\overrightarrow{W}_k = \overrightarrow{W}_{k-1} - \vec{p}_k\,, \qquad (k = 2,\, ...,\, N-2) \tag{3.18}$$

with $\overrightarrow{W}_1 = -\vec{p}_1$ and $\overrightarrow{W}_N = \vec{p}_N$. The momenta $\overrightarrow{W}_i$and corresponding relative coordinates $\vec{R}_i$ are substituted into the Hamiltonian which becomes

$$\begin{aligned} H &= \frac{1}{2} \sum_{k=1}^{N-1} \left(\frac{1}{m_k} + \frac{1}{m_{k+1}} \right) \overrightarrow{W}_k^2 - \sum_{k=2}^{N} \frac{1}{m_k} \overrightarrow{W}_{k-1} \cdot \overrightarrow{W}_k \\ &\quad - \sum_{k=1}^{N-1} \frac{m_k m_{k+1}}{R_k} - \sum_{1 \le i \le j-2}^{N} \frac{m_i m_j}{R_{ij}} \end{aligned} \tag{3.19}$$

where the non-chained distances are given by $R_{ij} = |\vec{r}_j - \vec{r}_i| = \left| \sum_{i \le k' \le j} \vec{R}_{k'} \right|$ and the m_i are the masses of the particles.

In order to regularize the Hamiltonian 3.19, we proceed, as we did in section 3.1.2, by first applying a time transformation and then substituting the KS-transformed coordinates and momenta. However, here we employ a different time transformation suggested by Mikkola & Aarseth (1990), which leads to a much better accuracy for the numerical integration. It is given by

$$t' = \frac{1}{T + U}$$

where the term $(T + U)$ is the Lagrangian of our multiple system. After applying this time transformation to the Hamiltonian 3.19 we obtain a Hamiltonian of the form $\Gamma = (H - E)/(T +$

U) (see Stiefel & Scheifele, 1971), where E is here the numerical value of the Hamiltonian H evaluated from the initial conditions. The transformations

$$\begin{aligned} \vec{R}_i &= L(\vec{Q}_i)\,\vec{Q}_i \\ \vec{W}_i &= \frac{L(\vec{Q}_i)\,\vec{P}_i}{2\left|\vec{Q}_i\right|^2} \end{aligned} \tag{3.20}$$

define the Hamiltonian in terms of the KS-transformed positions $\vec{Q}_i$ and momenta $\vec{P}_i$ (compare to relations 3.11 and 3.13), where L denotes the KS-matrix 3.12. The regularized Hamiltonian Γ is then given by

$$\begin{aligned} \Gamma = \frac{1}{(T+U)} \Bigg(& \frac{1}{4}\sum_{k=1}^{N-1}\left(\frac{1}{m_k}+\frac{1}{m_{k+1}}\right)\frac{\vec{P}_k^2}{\left|\vec{Q}_k\right|^2} - \sum_{k=1}^{N-1}\frac{m_k m_{k+1}}{\left|\vec{Q}_k\right|^2} \\ & + \frac{1}{4}\sum_{k=2}^{N}\frac{1}{m_k}\frac{\vec{P}_{k-1}^t L^t(\vec{Q}_{k-1})\,L(\vec{Q}_k)\vec{P}_k^t}{\left|\vec{Q}_{k-1}\right|^2\left|\vec{Q}_k\right|^2} - \sum_{1\le i\le j-2}^{N}\frac{m_i m_j}{R_{ij}} - E \Bigg), \end{aligned} \tag{3.21}$$

where $\vec{P}_k^t$ and L^t are the transposed forms of the momentum vectors and the KS-matrix L. From the regularized Hamiltonian we obtain the equations of motion by the Hamiltonian equations

$$\vec{Q}_k' = \frac{\partial\Gamma}{\partial\vec{P}_k}, \qquad \vec{P}_k' = -\frac{\partial\Gamma}{\partial\vec{Q}_k} \tag{3.22}$$

where a prime denotes differentiation with respect to the fictitious time s. The explicit expressions for $\vec{Q}_k'$ and $\vec{P}_k'$ together with the Lagrangian $(T+U)$ as function of the KS-transformed variables are given in Mikkola & Aarseth (1993). The differentiation with respect to $\vec{Q}_k$of the part of the Hamiltonian 3.21 that contains the non-chained distances R_{ij} can be carried out by exploiting that $\vec{Q}$ is the KS-transform of $\vec{R}$, with $\vec{R} = L(\vec{Q})\,\vec{Q}$, and the non-chained potential U_{nc} is $U_{nc} = U(\vec{R})$, thus a function of $\vec{R}$. The derivative $\partial U_{nc}/\partial\vec{Q}$ can then be written in the form $\partial U_{nc}/\partial\vec{Q} = 2\,L^t(\vec{Q})\partial U_{nc}/\partial\vec{R}$ (see also Stiefel & Scheifele, 1971). For the unperturbed chain, the equations of motion 3.22 then only need to be accompanied by the time equation

$$t' = \frac{1}{T+U} \tag{3.23}$$

making the system of regularized differential equations complete. In order to recover the relative coordinates and momenta from the solution, the relations 3.20 are used.

3.2.2 Algorithmic Implementation

The implementation of the chain regularization consists of the following main steps:

1. Determine the numerical value of the total energy E and of the Lagrangian $(T+U)$.

2. Find the chain indices, i.e. the particle indices along the chain.
3. Form the chained vectors $\vec{R}_k$, $\overrightarrow{W}_k$ (relations 3.17 and 3.18) and transform them to KS-variables $\vec{Q}_k$, $\vec{P}_k$ (using the inverse of relations 3.20).
4. Advance $\vec{Q}_k$, $\vec{P}_k$ and t by one ficticious time step (see equations 3.22 and 3.23).
5. Check if we have to switch the chain and if so, find the new chain indices and reconstruct the chain vectors $\vec{R}_k$, $\overrightarrow{W}_k$ and KS-variables $\vec{Q}_k$, $\vec{P}_k$. Otherwise leave the chain vectors and KS-variables untouched.
6. Repeat point 4 to 5 until we reached a given physical time or some other stopping condition.
7. Transform the KS-variables $\vec{Q}_k$ and $\vec{P}_k$ back to the physical chain vectors $\vec{R}_K$,$\overrightarrow{W}_k$ and then further to the physical variables $\vec{r}_i$ and $\vec{w}_i$ using the same relations as in point 3.

An important part of the implementation of the chain regularization method is the chain selection procedure, which must ensure that the dominant two-body motions are included. Before the calculation can begin the chain needs to be constructed. First the shortest inter-particle vector is is determined. Then we proceed by searching for the particle which is closest to either end of the known chain. This operation is repeated until all the particles have been included. To facilitate the procedure, it is beneficial to sort all the distances and perform a sequential search for the missing terms. The main steps to construct a new chain are as follows:

1. Find the new chain and reconstruct the chain vectors
   (a) Transformation of the KS-variables $\vec{Q}_k$ and $\vec{P}_k$ to physical variables $\vec{R}_k$ and $\overrightarrow{W}_k$, and further to $\vec{r}_i$, $\vec{w}_i$
   (b) evaluation and sorting of all mutual distances $\vec{r}_{ij} = |\vec{r}_i - \vec{r}_j|$ for $i \neq j$ and $i, j = 1, \ldots, N$
   (c) relabeling of particle indices along the new chain
   (d) formation of new chain vectors $\vec{R}_k$ and $\overrightarrow{W}_k$.
   (e) transformation to KS-variables $\vec{Q}_k$ and $\vec{P}_k$.

It is necessary to check after every integration step if the dominant two-body interactions are included (point 5 in the chain algorithm). This is because one integration step typically involves $\simeq 50$ derivative evaluations using the Bulirsch-Stoer method (Bulirsch & Stoer, 1966) and to integrate a close two-body encounter without regularizations is extremely inefficient and leads to a significant loss of accuracy. However, repeating the chain construction after every step might be time consuming and not always necessary. This especially applies to the case when we have one close pair and a third particle that is at a much wider distance. In this case we only have to make sure that the shortest distance between the pair is contained in the chain, while it is not necessary to require that always the shorter distance of the other

two much larger distances is included in it. This chain can then be integrated without any modification as long as the close pair and the other particle is well separated.

The actual decision-making algorithm in point 5 of the chain algorithm is simplified, if we consider only three- and four-body systems, as we will do throughout this thesis. Then the following simple geometrical consideration is sufficient: adopt the new chain if the smallest distance is not regularized or the second smallest distance coincides with the separation between the first and last chain member. An existing chain is therefore maintained during very close two-body encounters when a temporary transformation to physical variables and consequent chain reconstruction might lead to loss of accuracy caused by round-off errors.

The actual numerical integration is carried out by the extrapolation method of Bulirsch & Stoer (1966). This method also provides estimates of the local error. An integration step is considered to be successful if this local error is less than a pre-defined tolerance. In the chain algorithm this tolerance is specified with respect to the total energy. As shown in Mikkola & Aarseth (1990) we can write for the energy error $\delta H = |H - E|$

$$\frac{|H - E|}{(T + U)} \sim \epsilon$$

where ϵ is the maximum relative error of the coordinates and momenta. By comparing to the regularized Hamiltonian $\Gamma = (H - E)/(T + U)$ it turns out that the error condition is a condition on the numerical value of Γitself, leading to $\delta\Gamma \sim \epsilon$. In order to calculate the error in Γ we can write

$$\begin{aligned} \delta\Gamma &= \sum \left(\frac{\partial \Gamma}{\partial \vec{P}_k} \cdot \delta\vec{P}_k + \frac{\partial \Gamma}{\partial \vec{Q}_k} \cdot \delta\vec{Q}_k \right) \\ &= \sum \left(\vec{Q}'_k \cdot \delta\vec{P}_k - \vec{P}'_k \cdot \delta\vec{Q}_k \right). \end{aligned}$$

As it can be seen, we can use the energy conservation check without additional computational overhead, because the coefficients $\vec{Q}'_k$ and $\vec{P}'_k$ are readily available after the integration step, which also applies to the $\delta\vec{P}_k$ and $\delta\vec{Q}_k$ values, as they are estimated by the Bulirsch-Stoer method. In practice we require that every individual term in the above expression is, in absolute value, less than the specified tolerance.

3.2.3 Implementing Accretion

To allow for mass changes within the regularized chain integration is not straightforward as we are faced with the difficulty that the above positions and momenta are defined relative to the center of mass, which changes if the masses change. In addition, the inclusion of accretion into a multiple regularization scheme has been tried by many different groups more than 20 years ago without success (private communication Hans Scholl, 2004). Therefore, the only way to investigate accreting triple systems as we want to do in this thesis, is to first carry out a chain step leaving the masses of the bodies constant and then update the masses according to a given user-supplied expression. After that we have to update the center of mass and its velocity as well as the individual momenta of the bodies and the total energy of the system. How the

velocities have to be changed depends on the momentum transfer the accreted gas carries onto the bodies. In the code we treat two extreme cases of gas motion, one where we assume that the gas is at rest with respect to the reference frame, and one where we assume that the gas is always moving with the same velocity and direction of the corresponding accreting body. In the latter case the momentum of the bodies increases while the velocities remain unchanged during the mass growth, whereas in the former, the momentum remains unchanged and the velocities are reduced. For a physical justification we refer the reader to Chapter 4 as we are here only concerned with implementation issues.

The main chain algorithm from section 3.2.2 is modified as follows:

1. Determine the numerical value of the total energy E and of the Lagrangian $(T + U)$.
2. Find the chain indices, i.e. the particle indices along the chain.
3. Form the chained vectors $\vec{R}_k$, $\overrightarrow{W}_k$ and transform them to KS-variables $\vec{Q}_k$, $\vec{P}_k$.
4. *Compute accretion effects.*
5. Advance $\vec{Q}_k$, $\vec{P}_k$ and t by one ficticious time step (see equations 3.22 and 3.23).
6. Check if we have to switch the chain and if so, find the new chain indices and reconstruct the chain vectors $\vec{R}_k$, $\overrightarrow{W}_k$ and KS-variables $\vec{Q}_k$, $\vec{P}_k$.
7. Repeat point 4 to 6 until we reached a given physical time or some other stopping condition.
8. Transform the KS-variables $\vec{Q}_k$ and $\vec{P}_k$ back to the physical chain vectors $\vec{R}_K$,$\overrightarrow{W}_k$ and then further to the physical variables $\vec{r}_i$ and $\vec{w}_i$.

The accretion procedure takes as input argument the current time and the time difference since its last invocation and returns the new masses, relative coordinates, momenta and the total energy to the main routine. For the chain vectors the same chain as the previously generated is used. This is justified as long as the time steps or accretion rates are sufficiently small so that the effect of mass growth does not significantly deform this chain. The algorithm is as follows:

1. Compute accretion effects.
   (a) Transform the KS-variables back to the physical chain vectors and then further to the physical variables $\vec{r}_i$ and $\vec{w}_i$.
   (b) Calculate the new masses according to a user supplied expression.
   (c) Change the velocities according to an assumed momentum transfer prescription (user supplied).
   (d) Update the center of mass and velocity.
   (e) Update the physical chain vectors using the same chain as previously generated.

(f) Transform the physical chain vectors to the KS-transformed variables.

(g) Update the total energy of the system.

(h) Return the new chain variables, energy and masses.

As it will be shown in Chapter 4, for the accretion rates and initial conditions of the triple systems used in our simulations, we find that this implementation of accretion leads to a time-dependent total energy that matches our analytical predictions very well (see section 4.2.2). Our implementation, therefore, seems to be correct for our purposes.

Chapter 4

The Decay of Accreting Triple Systems as Brown Dwarf Formation Scenario

In this chapter we employ the chain method as explained in Chapter 3 in order to investigate the decay of accreting triple systems and their relation to the ejection scenario as Brown Dwarf formation scenario. We consider the statistics of the properties of single and binary Brown Dwarfs that formed by ejection in dependence of the accretion rate and gas motion of the accreted gas. We then compare the obtained Brown Dwarf properties to observations and can thus draw conclusions about the viability of the ejection scenario as Brown Dwarf formation scenario.

In section 4.1 we briefly highlight some interesting theoretical studies that have been recently done regarding decaying multiples and their relation to Brown Dwarf formation as well as other Brown Dwarf formation scenarios. In section 4.2 we show what we can expect from the results of the evolution of accreting multiple systems, in section 4.3 we explain the initial setup as well as the methodology of our simulations, in section 4.4 we present and discuss our results and, finally, in section 4.5 we present our conclusions obtained so far.

4.1 Previous Numerical Studies on Brown Dwarf Formation

Bate et al. (2002a) were the first who could follow the fragmentation of a massive cloud, subject to a turbulent velocity field, down to substellar masses and therefore were able to draw conclusions about how Brown Dwarfs form. They find that their Brown Dwarfs formed mainly through instabilities in massive circumstellar disks and, to a lower amount, as ejected embryos from unstable small-N clusters, confirming these Brown Dwarf formation channels. Lang (2003) carried out a similar study but instead of focusing on an entire turbulent molecular cloud he studied many realizations of a collapsing cloud core and its fragmentation. In both studies the number of Brown Dwarfs did not exceed 100 and there were only a few Brown Dwarf binaries. Their low frequency of less than 10% is in contradiction with the observed one of $\approx 20\%$ by Close et al. (2003) and Bouy et al. (2003). The reason for this is not very clear

yet. Bate et al. (2003) argue that the disruption of wider Brown Dwarf binaries due to the closeness of the encounters in their simulation (< 20AU) and exchange interactions with stars, which replace the lower-mass substellar members with more massive stellar objects, reduce significantly the number of Brown Dwarf binaries. However, we cannot exclude the possibility that the softening of the gravitational potential of the fragments, which is of the order of 10AU in their simulation, limits the formation of close Brown Dwarf binaries with semi-major axis $\leq$ 10AU, due to the lower absolute value of the potential energy at those radii compared to the non-softened potential, which should result in wider binary pairs. The greater semi-major axis of those binaries also reduces the probability that they survive subsequent gravitational interactions with the cluster. Given the low absolute numbers of Brown Dwarf binaries in these simulations it is impossible to obtain any firm statistical result about Brown Dwarf binaries and to compare them to the observations.

Kroupa & Bouvier (2003) discuss various scenarios of Brown Dwarf formation. They try to explain the different abundances of Brown Dwarfs seen by Briceño et al. (2002) in the Taurus region and the known one in the Orion nebula cluster (Muench et al., 2002; Luhman et al., 2000) by estimating the kinematics of Brown Dwarfs resulting from the different formation models. They find that the ejection scenario is able to reproduce the number of Brown Dwarfs per star consistently if one assumes that in both clusters the same number of Brown Dwarfs are produced per star and the velocity dispersion of the ejection process is about 2 km$\cdot$s^{-1}. These results have the disadvantage that they are in disagreement with the estimated Brown Dwarf abundance in the galactic field, if this abundance is not overestimated (Kroupa & Bouvier, 2003). If one, on the other hand, drops the assumption that the Brown Dwarf production rate is independent of the environment and assumes a velocity dispersion of 3km$\cdot$s^{-1} of the ejected Brown Dwarfs, they find that low-mass tranquil star-forming regions are more efficient in producing Brown Dwarfs than the ones like the Orion nebula cluster (ONC). This is also true even if one adds the Brown Dwarfs formed by photo-evaporation in the ONC.

The question whether the ejection scenario is able to reproduce the high abundance as well as the binary properties of Brown Dwarfs has been addressed by various authors. Sterzik & Durisen (2003) calculate pairing and binary statistics by integrating many small-N clusters neglecting hydrodynamical interaction by the remaining gas as well as any ongoing accretion. They constrain their initial conditions by a modified clump mass spectrum of Motte et al. (1998), which determines the total masses of the clusters, and a composite single star mass spectrum (SMS) which comprises a recently observed one for Brown Dwarfs (Béjar et al., 2001; Chabrier, 2002) as well as one for hydrogen-burning stars (Kroupa et al., 1993). They find broad agreement between their results and observations of Brown Dwarf binaries, concluding that, once Brown Dwarfs have formed in sufficient numbers as to fit the observed Brown-Dwarf-IMF of the galactic field, the subsequent decay of the emerging multiple systems with the given constraints can explain their binary properties. They also point out that, because they scale their results by fixing the virial speed for all systems choosing $v_{vir} = 3.3$ km$\cdot$s^{-1}, their Brown Dwarf systems are already in a very compact configuration close to the final binary separations. Indeed for a triple Brown Dwarf system, all having masses of $0.08 M_\odot$ one gets a very small Hénon radius R_H, which is a measure of the mean interparticle distance, with a value of $R_H \approx 10$ AU. Of course in initially higher order systems the interparticle distances can be larger, but even for a system of 6 Brown Dwarfs R_H is still as small as 20 AU. This scaling is motivated by the observed mass versus size relation of molecular cloud

cores that imply that the specific energy and hence the virial speed is a constant and of about the previously mentioned value. Sterzik & Durisen (2003) simply assume the same relation between the size of the emerging cluster and its total mass. The findings of Sterzik & Durisen (2003) therefore imply that from a purely dynamical point of view Brown Dwarfs must have formed in extremely compact configurations in order to explain the observed Brown Dwarf binary separations of, e.g. Close et al. (2003). It still has to be shown that fragments, which will eventually become Brown Dwarfs, are initially mostly formed within such small volumes. Simulations of Boss (2001) seem to support this view. Bate et al. (2002b) argue in contrary that at the time the isothermal collapse of a fragment ends and the gas starts to heat up and finally halts the collapse, the radii of these fragments should be at least 5 AU and their separations consequently $\gtrsim$ 10 AU. They also find in their numerical simulation no binary fragments forming with a lower initial separation. Also Bate et al. (2002a) reported that their ejected Brown Dwarfs were still undergoing significant accretion before the time of ejection, therefore contradicting the notion of Brown Dwarfs being "frozen" out of the gas with their final masses. Furthermore this makes it possible that fragments start out further apart with lower masses and much lower virial speed, and, due to their growing masses, finally reach the required compactness to produce tight binaries. Given these difficulties and the ease at which close binaries are formed if one includes mass growth during the dynamical interactions of the fragments, accretion seems to us the major ingredient to form close Brown Dwarf binaries.

Delgado-Donate et al. (2003) focus on accreting multiple system by placing 5 accreting seeds inside a molecular cloud core following their evolution in response to the gravitational potential of the gas as well as the mutual gravitational interaction between the seeds. They find that Brown Dwarfs, once an appropriate mass function for the parent cloud cores is chosen, are readily formed if dynamical interactions with an unstable multiple system are drawn into account. Even though they came to better statistical results on this formation scenario by integrating 100 realizations of a multiple system in a cloud, they got only a few Brown Dwarf binaries. They conclude that if the binary fraction among Brown Dwarfs turns out to be low, it can easily be explained by these simulations. On the other hand if the binary fraction turns out to be high, they infer that the core mass function must extend down into the substellar regime (the core mass function of Motte et al. (1998) they were using has a lower cut off of $0.25 M_{\odot}$). Because of their low Brown Dwarf binary statistics they cannot draw any further conclusions on the properties of Brown Dwarf binaries.

Given the computational expense of a full hydrodynamical simulation and the necessity to include mass growth of the fragments it is certainly appropriate to treat the gas accretion and interaction in an approximate fashion by assuming a certain accretion rate and specifying *ad hoc* the momentum the accreted mass adds to the stellar embryos. This approach was shown to be a good approximation in Bonnell et al. (1997) if one assumes that the gas is at rest and the bodies are not moving with significantly supersonic velocities. This modeling of dynamical interaction of the fragments allows for a better statistical description of the resulting Brown Dwarf properties, including binaries, because of the increased number of systems that can be integrated within a reasonable amount of time. It also quantifies the influence which accretion has on the dynamical evolution of multiple systems.

4.2 Analytical Predictions

4.2.1 The Toy Model

Our analytical model calculations are mainly based on the toy model of Reipurth & Clarke (2001) that we want to discuss here briefly. These calculations are mainly estimates of timescales of the physical processes involved.

At first it is assumed that a flattened cloud is collapsing and the central region accretes mass at a constant rate of $\dot{M}_{infall} \sim 6 \times 10^{-6} (T/10\mathrm{K})^{\frac{3}{2}} \mathrm{M}_{\odot}\mathrm{yr}^{-1}$. This value was obtained by numerical simulations of Hartmann, Calvet, & Boss (1996) who found a period of nearly constant mass accretion onto the central region that lasted about 1 free-fall time which corresponds to $\approx 10^5$yr in this case. For the following discussion we will consider all physical processes on this time scale. The central part of the cloud is assumed to fragment into 3 fragments and the infalling mass is equally distributed amongst them. The choice of 3 fragments is motivated by the fact that a triple system is the smallest possible cluster with the ability to decay into smaller-N systems, and therefore was chosen as starting point for their investigation. The typical time scale of such a multiple system is the so-called crossing time t_{cr}, for which Reipurth & Clarke (2001) use a simplified expression. As it will turn out these simplifications have a strong impact on the number of Brown Dwarfs formed, so we therefore want to explicitely show which approximations were used. The crossing time is defined as (Anosova, 1986)

$$t_{cr} = \frac{G \sqrt{\sum_i M_i} \sum_{i \neq j} M_i M_j}{(-2E)^{3/2}}, \tag{4.1}$$

where E is the total Energy and G the gravitational constant. This expression can be simplified if one sets $M_i = M$ for all i and assumes virial equilibrium. We then get

$$t_{cr} = \frac{3^{3/2}}{\sqrt{G\,M \left(\sum_{i \neq j} \left(\frac{1}{r_{ij}} \right) \right)^3}}, \tag{4.2}$$

where r_{ij} is the distance between the body i and j. For three bodies and $r_{ij} = R$ for all $i \neq j$, this further reduces to

$$t_{cr} \sim 0.16 \sqrt{\frac{(R/\mathrm{AU})^3}{M/\mathrm{M}_{\odot}}}. \tag{4.3}$$

This was used in the discussion of Reipurth & Clarke (2001) and will be refered as the $R = const.$-approximation for the rest of this paper.

Only a few triple systems are known to be stable while all the other decay after some time, ejecting a single body and a binary system into opposite directions. Reipurth & Clarke (2001) now want to estimate how many systems have decayed before their masses grow beyond the hydrogen-burning limit, which is, for our discussion, set to $0.08\,\mathrm{M}_{\odot}$. The time of such a decay

can only be described stochastically. Anosova (1986) find that the number of systems that have not yet decayed at a time t is roughly an exponential function over time, characterized by the half life of the decay τ. The half life has to be determined numerically and Sterzik & Durisen (1995) found in their simulations of decaying multiple systems that 95% of their systems have decayed after $100t_{cr}$, giving $\tau \approx 23.1\,t_{cr}$. To account for the increasing masses of the fragments the mass M is considered to be a function of time and, for simplicity, this function is further assumed to be linear. The mass growth decreases t_{cr} and therefore τ, increasing the probability that a triple system decays after a time t. Plugging in the time dependence of M into t_{cr} and assuming a quite conservative value for R, with $R = 200\,\mathrm{AU}$, results in a decay function as shown by Reipurth & Clarke (2001, Fig. 1). In this figure it is also accounted for that, at the beginning of the formation of the fragments, their interaction potential is, due to their small masses, still low compared to the potential of the surrounding gas. Therefore the fragments do not interact significantly until a time T_i which, in absence of any detailed hydrodynamical calculations, cannot be reliably determined and was therefore set to a time when $M = 0.04\mathrm{M}_{\odot}$. This value is quite "pessimistic", as it significantly reduces the time interval within which the fragments have to decay before they reach the hydrogen burning limit. In this calculation a third of the systems have decayed before they reached that mass limit and consequently became Brown Dwarfs. At this point we find it is worth pointing out that lower accretion rates result in a higher abundance of Brown Dwarfs, although the decay of the triple systems happens a lot later.

This result shows, according to Reipurth & Clarke (2001), that the ejection scenario is able to produce many Brown Dwarfs even under quite "pessimistic" assumptions and should be therefore very efficient in more realistic situations. So they argue that, for instance, the time the fragments need to reach the hydrogen burning limit greatly increased if the mass is distributed amongst more than three bodies, resulting in a lower accretion rate for each Brown Dwarf. Also, they note, the accretion process is stopped earlier if the infalling gas is not equally distributed among the bodies. A mass difference between them tends to drive out the lower-mass member by mass segregation, whereby this body accretes even less material because of the lower gas densities in the outer regions of the cloud. This process drives it even further out by mass segregation and so forth. This scenario has been named 'competetive accretion' and was investigated by Bonnell et al. (2001). We find that the average distance and mass is also a very conservative choice compared to the one suggested by Sterzik & Durisen (2003), who effectively place three bodies with a mass of $0.08\,\mathrm{M}_{\odot}$ inside a volume of 10 AU as pointed out in section 4.1.

While the initial conditions seem to be "pessimistic" in order to produce Brown Dwarfs, there is one assumption that was too optimistic for triple systems, namely the half life of the decay. Our own simulations of 1000 decaying triple systems suggest, that only about 55% of all the systems have decayed after $100\,t_{cr}$, making $\tau \approx 87\,t_{cr}$. Repeating the previous calculation with the new τ yields a Brown Dwarf formation probability of only 13%, making the ejection scenario much less probable if only three fragments are involved. We want to show, however, that the rather low probability of forming Brown Dwarfs from unstable triple systems is a dramatic understatement of how efficient this particular model is. The key point that has been left out in the previous calculation is the fact that while the fragments are growing in mass the whole multiple system shrinks in size, making R a function of time. But to account for this effect we first need to have a closer look at the change of energy of an accreting triple

system which also requires some consideration on how mass is accreted onto the bodies.

4.2.2 The Energy of Accreting Multiples

To obtain an expression for the energy of accreting bodies we first have to consider how much momentum the infalling gas carries onto them. The first case we want to look at is accretion of gas at rest, which means that the momentum of the fragments is not changed when the mass is increased. The change of the momentum is therefore only due to the gravitational force between the bodies. The Newtonian equations therefore read

$$\frac{dM_i}{dt} \cdot \mathbf{v_i} + \frac{d\mathbf{v_i}}{dt} \cdot M_i = G \sum_{i \neq j} \left(\frac{M_i M_j}{r_{ij}^2} \frac{\mathbf{r_{ij}}}{r_{ij}} \right). \tag{4.4}$$

The difference to the equations of motion with constant masses is the term $dM_i/dt \cdot \mathbf{v_i}$ which can also be seen as an additional velocity dependent friction term, and thus will be treated like an external force in the following discussion. In the cluster simulations of Bonnell et al. (1997) this approximation was shown to reflect the evolution of the total energy of the cluster over time of their fully hydrodynamical calculation sufficiently well as long as the bodies do not move significantly supersonic. As we expect our fragments to move with a speed of the order of 1 km/s, which is about 4 times higher than the typical sound speed of a cold molecular cloud core, this approximation should still be an underestimate.

To derive the energy equation for multiple systems, accreting gas at rest, we multiply both sides of equation 4.4 with $\mathbf{v_i}$ and rearrange it to give

$$\frac{dE}{dt} = -\sum_i \left(\frac{dM_i}{dt} \frac{v_i^2}{2} \right) - G \sum_{i \neq j} \left(\frac{d(M_i M_j)/dt}{r_{ij}} \right) \tag{4.5}$$

with

$$E = \sum_i \left(\frac{M_i}{2} v_i^2 \right) - G \sum_{i \neq j} \left(\frac{M_i M_j}{r_{ij}} \right). \tag{4.6}$$

Splitting up E in kinetic and potential Energy, E_{kin} and E_{pot}, equation 4.5 becomes

$$\frac{dE}{dt} = -\frac{\dot{M}}{M} E_{kin} + 2 \frac{\dot{M}}{M} E_{pot} \tag{4.7}$$

where we set $M_i = M$ and $\dot{M}_i = \dot{M}$ for all i as we will only consider equal mass systems in this paper. Assuming virial equilibrium, that gives

$$\frac{1}{2} E_{pot} = E \tag{4.8}$$

and

$$E_{kin} = -E\,, \tag{4.9}$$

finally leads to

$$\frac{dE}{dt} = 5 \cdot \frac{\dot{M}(t)}{M(t)} E. \tag{4.10}$$

This is a linear first-order differential equation with time varying parameters and has the solution

$$E(t) = E_0 \cdot \exp\left(\int_0^t 5 \cdot \frac{\dot{M}(u)}{M(u)}\, du\right). \tag{4.11}$$

By setting $M = \dot{M} \cdot t + M_0$ and $\dot{M} = const.$ we obtain the final energy equation for our model with accretion of gas at rest

$$E(t) = E_0 \cdot \left(\frac{\dot{M}}{M_0} t + 1\right)^5. \tag{4.12}$$

As is easily seen the energy depends strongly on the accretion rate $\dot{M}$ and decreases, due to $E_0 < 0$, with the 5^{th} power of t, making the system shrink extremely quickly. This expression also shows that the typical time scale at which the systems shrinks goes with $\sim \left(\dot{M}/M_0\right)^5$, i.e. with the accretion time scale to the power of 5 for accretion of gas at rest.

If we compare this with the toy model of Reipurth & Clarke (2001) where the energy equation reads

$$E(t) = -3\,G\,\frac{\left(\dot{M} \cdot t + M_0\right)^2}{R} \tag{4.13}$$

with constant R, it can be clearly seen that we get a less steep dependence on t and $\dot{M}$ if only the mass growth but not the time dependence of R is considered, underestimating the compactness of accreting multiple systems, which in turn makes the decay times too long.

We also want to see how the energy decreases if the gas is not at rest. For simplicity we assume that the accreted mass is moving at the same speed and direction as the bodies, thus leaving the velocities of them unchanged. While it cannot be expected that this type of accretion is a physically reasonable choice it should nevertheless show the influence of gas motion on our results. The equations of motion remain unchanged and the energy relation reads

$$\frac{dE}{dt} = +\frac{\dot{M}}{M} E_{kin} + 2\,\frac{\dot{M}}{M} E_{pot} \tag{4.14}$$

and repeating the steps we did to obtain $E(t)$ for the accretion of gas at rest, we finally get

$$E(t) = E_0 \cdot \left(\frac{\dot{M}}{M_0} \cdot t + 1\right)^3 \tag{4.15}$$

which differs from the solution with accretion of gas at rest only in the value of the exponent. Now the energy depends less strongly on the accretion rate and t as the typical time scale at which the system shrinks goes only with the 3^{rd} power of the accretion time scale. We should therefore expect, on average, longer decay times than we would get in the case of accretion of gas at rest but still shorter time scales as in the toy model of Reipurth & Clarke (2001). For illustration, we can also assume that the gas has always the same velocity but the opposite direction as the fragments. This would lead to a value of the exponent of 7, resulting in an even stronger decrease of the total energy and therefore to even shorter decay times as in the 'accretion-of-gas-at-rest' model.

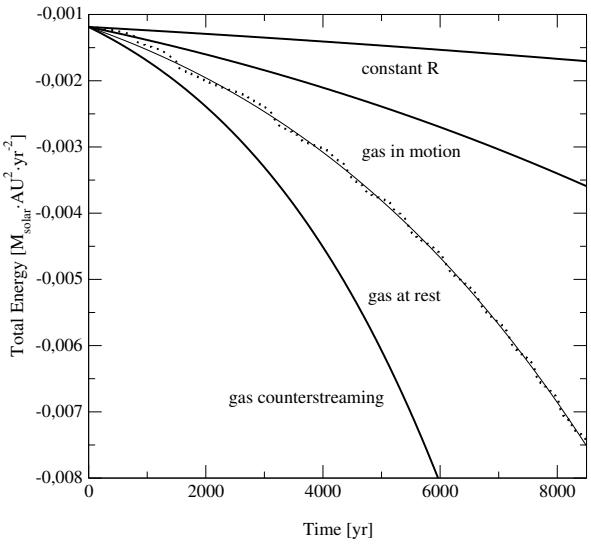

Figure 4.1: Comparison of the numerical solution (dotted line) of an accreting triple system accreting gas at rest with the analytic solution. In addition the analytical solution for accretion of gas in motion and of counterstreaming gas, as well as the solution using the approximation $R = const.$ (Reipurth & Clarke, 2001) are shown. It can be clearly seen that the latter approximation underestimates the absolute value of the total energy by an order of magnitude.

To show the validity of our calculations, we integrate the equations of motion numerically as will be described in section 4.3 and plot the total energy over time which is shown in Fig. 4.1. The numerical solution seems to oscillate a little around the equilibrium solution indicating that the system does not strictly remain virialised. This effect was to be expected as the virial theorem is not strictly valid here because the velocities of the bodies are not limited at close collision (see e.g. Landau & Lifshitz 1969, chapter 10). Despite these deviations our numerical solution matches the predicted energy curve very well. These oscillations seem to be a general property of strongly gravitationally interacting triple systems as they were also seen in the study of Anosova et al. (1989) in the virial coefficient k, defined as $k = E_{kin}/\left|E_{pot}\right|$which is for Newtonian interactions 1/2. A comparison of their Fig. 3 with our deviations from the expected energy curve show qualitatively the same behavior as they both oscillate around an equilibrium solution. It should be mentioned that we start with zero velocities and therefore are, at the beginning, not in virial equilibrium. This explains why at the beginning the numerical solution is always above the analytical value. At later times (here after about 2000 yr), which correspond to the first two collisions, the numerical solution lies on average close to our analytical estimate. Also shown in Fig. 4.1 is the assumed energy curve used by Reipurth & Clarke (2001) which differs by one order of magnitude from our results, regarding accretion of gas at rest.

4.2.3 The Expected Formation Probability of Brown Dwarfs

Since we found that both our analytically and numerically obtained $E(t)$ agree very well, we now want to use the analytical solution to obtain the formation probability of Brown Dwarfs

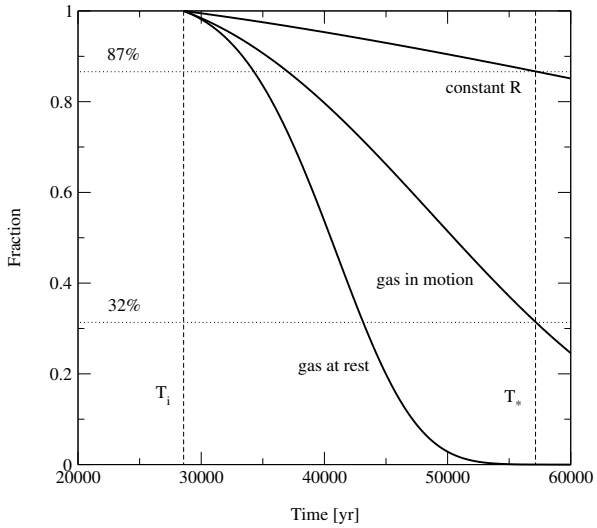

Figure 4.2: The probability that an equal mass triple system has not yet decayed after a time t for the different models. T_* is the time when the fragments reach the Brown Dwarf limit of $M = 0.08\mathrm{M}_\odot$ and T_i is the time the fragments effectively start to interact with each other, which was chosen to be the time when they reach $0.04\mathrm{M}_\odot$.

repeating the steps done by Reipurth & Clarke (2001), but using the proper half life of the decay for triple systems of $\tau = 87 t_{cr}$ as obtained from our calculations. The result is shown in Fig. 4.2. As it was to be expected from the energy curves of the previous section, the $R = const.$-approximation underestimates significantly the number of Brown Dwarfs. The approximation of 'gas in motion' leads to a six times higher number of Brown Dwarfs and with the 'gas at rest'-approximation almost all ejected fragments should be Brown Dwarfs. For our numerical investigation that follows, however, we do not expect that all ejected fragments have a mass lower than $0.08\mathrm{M}_\odot$. We find that there is a significant number of meta-stable and stable systems with extremely long decay times, challenging the assumption that the number of systems that have not yet decayed is a simple exponential function over time (Binney & Tremaine, 1987). Furthermore, the determination of the half life of the decay is not unique, because counting the number of systems that have not yet decayed after any other time as $100 t_{cr}$ gives very diverse values of τ, sometimes deviating by a factor of more than 2. Clearly the question of how to obtain statistically the number of decayed systems as a function of time needs to be investigated more thoroughly. For this reason the decay curves as shown in Fig. 4.2 are expected to deviate quite a bit from our numerical results, but we do not expect this deviation to be an order of magnitude.

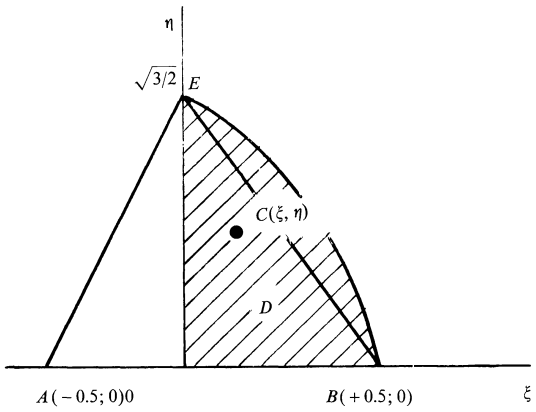

Figure 4.3: Initial configuration of the triple systems (taken from Anosova, 1986). The components of the triple systems are placed at the points $A\,(-0.5, 0)$, $B\,(+0.5, 0)$, and $C\,(\xi, \eta)$. The point C is chosen randomly within the region D.

4.3 Simulations

4.3.1 Initial Conditions

In order to investigate the ejection scenario numerically we integrate a large number (1000) of realizations of triple systems with an initial mass of $0.04\mathrm{M}_{\odot}$ and with constant mass growth $\dot{M}$. To cover all geometrically possible initial configurations we follow the approach of Anosova (1986), illustrated in Fig. 4.3, where all three bodies are initially in the $x-y$-plane and two bodies are always placed at $x = -0.5$, $y = 0$ and $x = 0.5$, $y = 0$. The position of the third body is randomly chosen within a region lying in the positive quadrant and embraced by a unit circle around the point $x = -0.5$, $y = 0$ (region D in Fig. 4.3). This arrangement of the bodies has been proven to be a representative sample for statistical studies of unstable triple systems by Anosova & Orlov (1994). We then multiply the initial position vectors by 200 AU to give the desired maximum separation.

The initial velocities of the cluster members are usually derived from the kinematical properties of the surrounding molecular cloud core. Since the observed ratio of rotational to potential energy of molecular cloud cores, β, has been found to be low for most of the cloud cores, with a value of $\beta = 0.02$ (Goodman et al., 1993), we do, for simplicity, neglect any possible initial uniform rotation of our clusters. This decreases the lifetime of our triple systems, but we do not expect this effect to be significant for our main results. We also neglect any random motion the fragments could have due to the thermal as well as the turbulent energy of the cloud. This approximation seems justified as the temperatures of molecular cloud cores are rather low and, because the turbulent velocities are thought to be subsonic at the time fragmentation starts, the turbulent velocities must be rather low as well. However, as it was shown in section 4.2.2 most of our triple systems reached their virial equilibrium state quickly. Thus most of the observed collapse of the system is due to its dissipative energy change rather than virialisation,

which is why our results will not change significantly as a function of initial velocities of the fragments. So, for simplicity, all our fragments start with zero velocities getting the maximum value of v_{vir} for a given three body geometry.

Our choice of initial positions and velocities results in a range of total energies and consequently virial speeds with most of them having values between 0.6 and $0.8\,\mathrm{km}\cdot\mathrm{s}^{-1}$. In this range the distribution of v_{vir} is nearly flat. Thus our initial conditions are, apart from the absolute value, very similar to the ones favored by Sterzik & Durisen (1998) and used by Sterzik & Durisen (2003).

During the integration the fragments accrete mass at a given rate which we will vary to investigate the influence of $\dot{M}$ on our results. For $\dot{M}$ we choose 1, 2 and 5 times the value suggested by Reipurth & Clarke (2001) of $\dot{M}_{RC} \approx 1.4 \cdot 10^{-6}\,\mathrm{M}_\odot \cdot \mathrm{yr}^{-1}$ per fragment for a cloud with a temperature of 10 K. We further assume a certain radius around the origin outside of which the accretion of the fragments is stopped if the system has decayed. This radius serves as an 'effective' cloud radius, determining the region where the bodies accrete a significant amount of gas. Because we only stop the accretion of a single body if the triple system has decayed, we can investigate accreting equal mass systems and limit the influence of the rather artificial geometry of the accretion region. Otherwise the geometry of the accretion region would have strong effects on our results through unequal accretion, which would not be modeled reasonably in this case. In order to decide whether a system has decayed, we employ two simple escape criteria. First, we require that the escaper and the binary are unbound with respect to each other, i.e. the total energy of the binary, treated as one body, and the escaper is positive. Second, we require that the distance between the escaper and the center of mass of the binary is more than $7 \cdot d_0$ with d_0 being the initial mean harmonic distance. Hence our cloud radius has to be larger than $7 \cdot 2/3\, d_{0,max} \approx 462\,\mathrm{AU}$ because as soon as the escaper reaches the end of the accretion region we have to decide whether the system has decayed and consequently whether we have to stop any further accretion or not. The value of the minimum cloud radius was obtained by taking into account that the escaper has twice the speed of the binary and both are moving in opposite directions. Our cloud radius was chosen to be $R_{cl} = 600\,\mathrm{AU}$ and for comparison we also performed some runs with higher R_{cl} but found, that our results do not vary significantly even if we increase this value by a factor of 2.

As outlined in section 4.2.2, we will investigate two cases of momentum transfer during mass growth, one with zero momentum transfer (gas is at rest) and one with a momentum that does not change the velocity of the bodies, corresponding to gas that is accreted while having the same direction and absolute value of the velocity as the bodies. The latter case is there to unambiguously see the effect when the bodies pick up momentum during accretion.

The integration of the equations of motion are performed with the chain code of Mikkola & Aarseth (1993) with our modifications as described in Chapter 3. This code gives sufficiently low errors in the total energy budget. This is a necessary requirement as the total energy directly relates to the ejection velocities, binary separations and decay times we want to investigate. In our test calculations of constant-mass triple systems we observed a median relative error in energy of 10^{-12}.

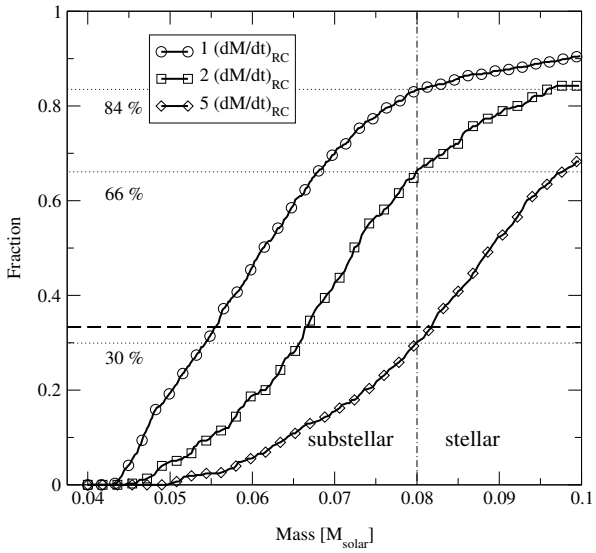

Figure 4.4: Fraction of systems that ejected a single member with a mass lower than a given mass m. Shown are the results for different accretion rates in multiples of $1.4\,10^{-6}\,\mathrm{M}_{\odot}\mathrm{yr}^{-1}$ of gas at rest. The dashed line represents the estimate of Reipurth & Clarke (2001) of ejected embryos with a lower mass than $0.08\,\mathrm{M}_{\odot}$. It can be clearly seen that only if the accretion rate is 5 times the value suggested by Reipurth & Clarke (2001) the number of Brown Dwarfs match their estimate.

4.4 Results

4.4.1 Number of Brown Dwarfs

In Fig. 4.4 the fraction of systems, accreting gas at rest, that ejected a single member with a mass lower than a given mass m is shown. As indicative from the discussion in section 4.2.3 the number of Brown Dwarfs in our simulation is lower (84%) than the analytically obtained value (nearly 100%). Since we measured the mass of the ejected embryo at the cloud edge, the masses are generally higher than at the time of decay which was predicted in our analytical model. This difference, however, is only of the order of a few percent and can, therefore, not explain the gap between our numerical and analytical results. Furthermore, the influence of the accretion radius on the decay times of the systems turned out to be negligible. Nevertheless, the fraction of systems that produced Brown Dwarfs is almost three times higher than was assumed by Reipurth & Clarke (2001) and more than six times higher as in the $R = const.$-approximation for triple systems. Considering that in reality the accretion process is likely to be competitive, increasing the formation probability of Brown Dwarfs, as outlined in section 4.2, our numerical results seem to confirm that the ejection scenario can be very efficient even if one only considers three fragments. It must be mentioned that the "accretion-of-gas-at-rest approximation" is only valid if the fragments are moving at subsonic velocities (Bonnell et al., 1997). However, the average velocity of our bodies is of the order of a few $\mathrm{km{\cdot}s}^{-1}$. Therefore we still underestimate the decrease in energy of the systems, as additional drag forces from the gas, caused by the bodies exciting wakes in their passage, are not taken into account.

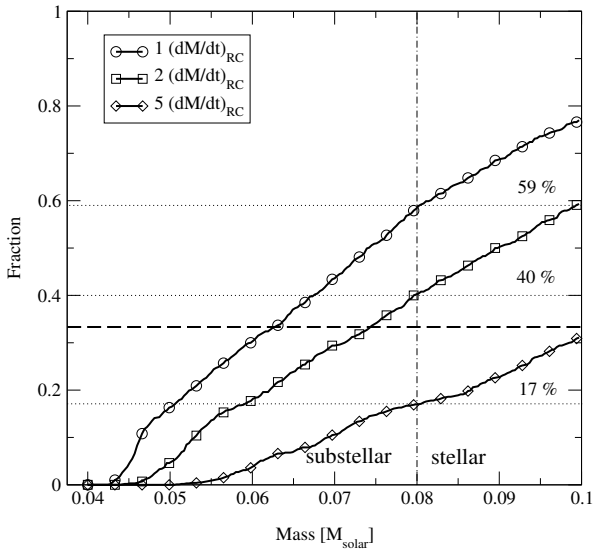

Figure 4.5: Fraction of systems that ejected a single member with a mass lower than a given mass m. Shown are the results for different rates of accretion of gas in 'extreme' motion in multiples of $1.4\,10^{-6}\,\mathrm{M}_{\odot}\mathrm{yr}^{-1}$. The dashed line represents the estimate of Reipurth & Clarke (2001) of ejected embryos with a lower mass than $0.08\,\mathrm{M}_{\odot}$. As in the case of accretion of gas at rest, the number of Brown Dwarfs in our simulation is significantly higher than they assumed.

We also show in Fig. 4.4 the number of Brown Dwarfs obtained at higher accretion rates. It can be seen that the number of Brown Dwarfs decreases with increasing $\dot{M}$ and only if the accretion rate is 5 times the value suggested by Reipurth & Clarke (2001) one gets about the same number of Brown Dwarfs as they obtained. This once more demonstrates that the shrinkage of the system, reflected by the time dependence of R, and the interaction with the gas decreases greatly the total energy of the triple system at a given $\dot{M}$ and, therefore, increases the decay probability before the hydrogen-burning limit is reached. It also shows that the decay curve over the time t cannot be expressed by a single exponential because of the significant gap between our analytical and numerical results.

Fig. 4.5 shows the fraction of ejected fragments with a lower mass than a given mass m, accreting gas in 'extreme' motion. As in the case of accretion of gas at rest, the number of Brown Dwarfs in our simulations is lower than we expected from our analytical calculations. The difference, however, of about 9% is considerably smaller than the difference in the case of accretion of gas at rest, which was 18%. Increasing the accretion rate causes the number of Brown Dwarfs to decrease and in this case a little more than twice the suggested value of $\dot{M}$ is necessary to obtain the same number of Brown Dwarfs as anticipated by Reipurth & Clarke (2001).

4.4.2 Decay Times

In Fig. 4.6 the cumulative distribution of the decay times of accreting triple systems is shown

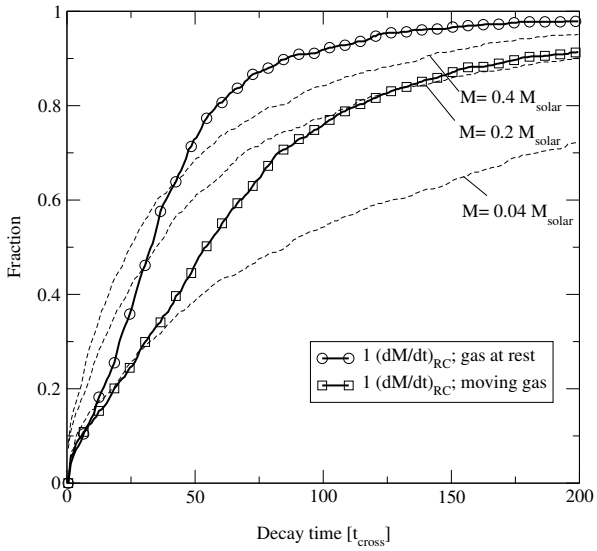

Figure 4.6: Fraction of systems that decayed before a time t in initial ($M = M_0$) crossing times. The solid lines represent the results for triples accreting gas at rest (open circles) and for triples accreting gas in motion (open squares). For comparison the results of decaying triple systems with constant mass of $M = 0.04$, 0.2, $0.4\,\mathrm{M}_\odot$ are also shown (dashed lines).

and compared to those of decaying systems of constant mass. As it was expected due to the decrease in total energy over time, the decay probability of accreting triples quickly exceeds the time for a constant mass of $M = 0.04\,\mathrm{M}_\odot$ and after some crossing times even those with $M = 0.2\,\mathrm{M}_\odot$ and $M = 0.4\,\mathrm{M}_\odot$. The different slopes of the curves for the different accretion models reflect the different time dependence on the total energy. Due to the different time dependence, the decay probability of the triple systems accreting gas at rest is generally higher than that of the triple systems accreting gas in motion. It is worth pointing out that the maximum fragment mass reached in our experiments with accretion is still lower than $0.4\,\mathrm{M}_\odot$ for the accretion of gas at rest model and lower than $0.2\,\mathrm{M}_\odot$ in the case of accretion of gas in motion. This might look counterintuitive because, on average, lower-mass but accreting triple systems seem to decay earlier than heavier non-accreting systems. However this is a direct consequence of the time dependence of R explained in section 4.2.2.

4.4.3 Escape Velocities

Fig. 4.7 shows the distribution of escape velocities of ejected Brown Dwarfs which are higher than a certain velocity v. Compared to constant-mass systems, the escape velocities are considerably higher for triple systems accreting gas at rest with the median of the distribution being boosted up by a factor of two and more, depending on the accretion rate.

In our simulation more than 28% of the escaping Brown Dwarfs have a larger velocity than $2\mathrm{km}\cdot\mathrm{s}^{-1}$ as opposed to only 10% in the case of constant-mass systems with $M = 0.08$. One also finds that there is a tendency towards higher escape velocities with higher accretion rates

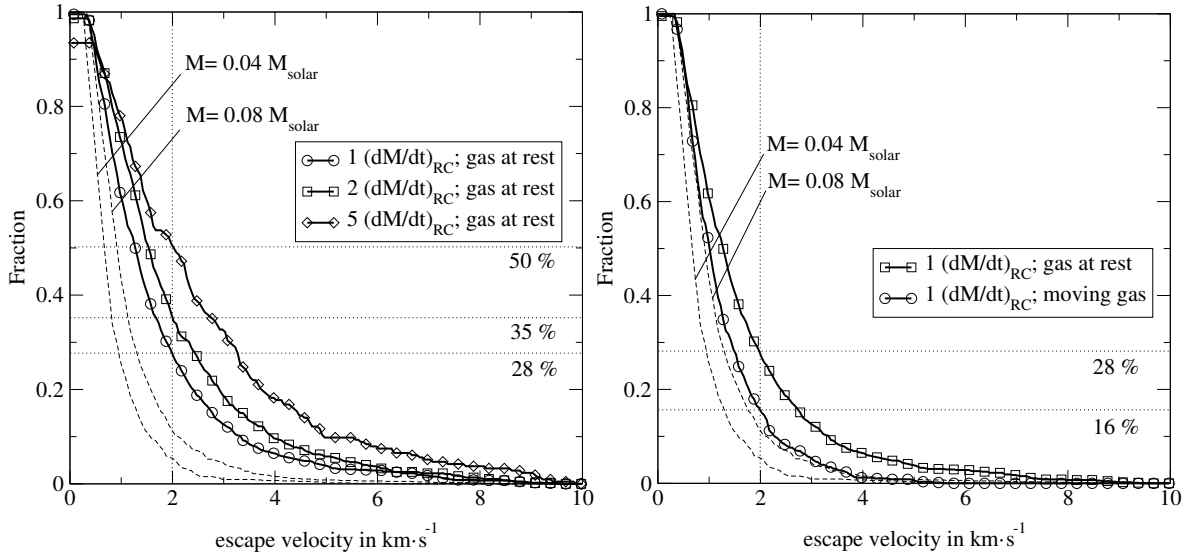

Figure 4.7: Fraction of systems, producing a single ejected Brown Dwarf with a speed larger than a given velocity v for different accretion rates (a) and different accretion models (b). Also shown are the results for systems of constant mass (dashed lines).

with more massive Brown Dwarfs being formed at higher $\dot{M}$. Half of the Brown Dwarfs that formed at an accretion rate of $5\dot{M}_{RC}$ obtain an escape velocity of more than $2\,\mathrm{km}\cdot\mathrm{s}^{-1}$. For systems that accrete gas in 'extreme' motion, the escape velocities are only marginally higher than the velocities for systems of constant mass with $M = 0.08\,\mathrm{M}_{\odot}$. The difference to the escape velocities from systems accreting gas at rest is a direct consequence of the, on average, lower absolute value of the total energy at decay time of the systems accreting gas in motion. In all cases the escape velocities of Brown Dwarfs are always higher if they have been ejected from accreting triples even if compared to the ones from the most massive equal-mass Brown Dwarf system with constant mass.

These results have a direct implication for the abundance of Brown Dwarfs in stellar systems as discussed by Kroupa & Bouvier (2003). As we find almost more than a third of the escapers having velocities exceeding $2\,\mathrm{km}\cdot\mathrm{s}^{-1}$, they should easily escape their stellar birth cluster if this cluster has a lower escape velocity than the Taurus cluster with $\mathrm{v}_{esc} = 1.4\,\mathrm{km}\cdot\mathrm{s}^{-1}$. Therefore, it is observationally difficult to detect such free-floating Brown Dwarfs at an advanced age like that of Taurus. On the other hand, it must be emphasized that for accretion rates that are not too high, the fraction of escapers with a lower escape velocity than $1.4\,\mathrm{km}\cdot\mathrm{s}^{-1}$ is, with about 50%, very high and one should therefore also expect many Brown Dwarfs to be retained in similar clusters at a younger age. The observed abundance of Brown Dwarfs in a young cluster also depends critically on the evolution of the entire cluster which is until today only well understood for a few of the sufficiently young star-forming regions, such as Taurus, the Pleiades and the ONC. This makes it hard to draw any conclusions about how Brown Dwarfs form from the observed abundance alone in other clusters, where there is little information

about the earlier cluster evolution.

4.4.4 Binary Semi Major Axis

The investigation of binary properties should give tighter constraints on the formation model, as at least for close binaries it is not expected that they change their orbital parameters a lot because of possible interactions with other members of the surrounding stellar cluster. If the surrounding cluster is virialized, then the encounter probability for sufficiently close encounters is only significant in regions with extreme stellar densities, such as the inner 0.4pc of the Trapezium cluster (compare to Clarke & Pringle (1991)).

The advantage of our simulations is the ability to investigate a large number of Brown Dwarf binaries as a result of the neglect of competitive accretion. As in reality, however, competetive accretion will take place to some degree, we investigated this effect by performing test calculations of accreting triple systems, where the same infalling mass is unequally distributed. We found a clear trend towards lower abundances of Brown Dwarf binaries with higher differences in the accretion rates, while the semi-major axis distribution did not change significantly. From the latter result and the assumption that the two heaviest bodies always form the binary, the reason for the lower abundance is simply a result of the binaries having higher masses for a given total energy at the time of decay which results in lower escape velocities.

In all of our runs, we got a few hundred up to more than 800 binary Brown Dwarfs, depending on the accretion rate, which makes it possible to obtain statistically meaningful results. In Fig. 4.8 the distribution of the semi-major axis of our obtained Brown Dwarf binaries is shown for the different types of accretion as well as for $M = 0.08\,\mathrm{M}_\odot$ systems of constant mass. In this plot it is remarkable that the separations of the heaviest possible Brown Dwarf binaries resulting from the decay of systems with constant mass are on average a lot higher, with its median being larger by a factor of 5, than the binary separations resulting from accreting lower mass triples. It can be clearly seen that the semi-major axis distribution for accreting triple systems is narrower and the peak is at lower values compared to systems of constant mass. The difference is again caused by the time dependence of the total energy for the different types of accretion compared to the $R = const.$ case. It is also responsible for reducing the median binary separation to 1/50th of its original value, R=200. In addition, from this plot one can infer that the more the momentum of the bodies is reduced, the narrower the semi-major axis distribution and the lower the peak position of the distribution become. We also found that the peak of the semi-major axis distribution does not change much with the accretion rate; only the cut-off is lower for higher rates. This is simply a result of only considering Brown Dwarf systems, because the final total energy is $\sim (M(t)/M_0)^n$, with n depending on the accretion model, which means that the total energy depends on the final mass of the fragments and not directly on the accretion rate. Therefore, choosing a maximum mass limit determines the available maximum energy that can be divided between the kinetic energy of the escaper and the energy of the binary. The lower cut-off of the distribution for higher accretion rates is mainly due to the fact that, at higher accretion rates, more massive Brown Dwarf binaries are formed, which causes the minimum total energy of the system to increase, thus decreasing the maximum semi-major axis.

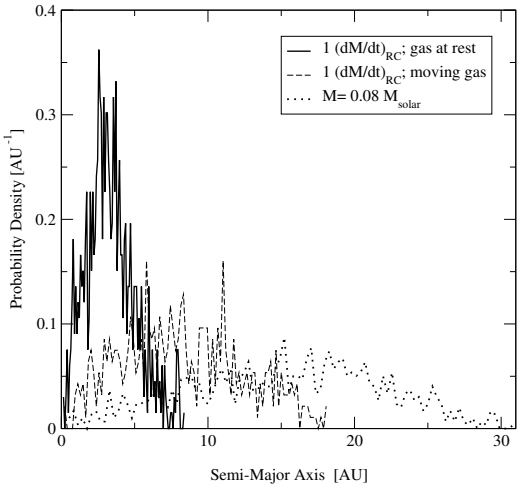

Figure 4.8: Semi major axis distribution for different kinds of accretion at $\dot{M} = \dot{M}_{RC}$ as well as for constant mass systems with $M = 0.08\,\mathrm{M}_{\odot}$. Due to the steeper decrease of the total energy in the case of accretion of gas at rest the resulting Brown Dwarf binaries have lower separations than in the case of accretion of gas in 'extreme' motion.

Surprisingly, the semi-major axis distributions resulting from accreting triple systems already bear some resemblance to the observed one by Bouy et al. (2003), as there is no Brown Dwarf binary with a wider separation than 20 AU, and the observed peak is at about the same value as the observed value $a_{peak} \approx 3\,\mathrm{AU}$. The observed sample, however, has the disadvantage that it is magnitude limited and therefore prone to biases.

To get an approximately unbiased sample it is better to choose the binary Brown Dwarfs over a finite volume within which both components can be fully resolved. For the sample of Bouy et al. (2003), this would include all binaries with a distance of less than 25 pc (W. Brandner 2004, private communication). The semi-major axis distribution of these objects is shown in Fig. 4.9 together with our numerically obtained distribution for decaying triples, accreting gas at rest. There is a remarkable agreement between these two distributions, as they both have the peak value at $a \approx 3\,\mathrm{AU}$ and approximately the same, rather steep, slope to both sides of it. That our distribution fits almost perfectly the one obtained from observations is certainly a coincidence, given the arbitrariness of our initial conditions. However, what we can predict is that, according to our model, the distribution cannot be flat for a semi major axis below the peak value, but must decrease. Because of the detection limit of the observations of Bouy et al. (2003), it is not clear whether or not the observed distribution will also decrease with decreasing a. This rather steep decline in our simulation is not a numerical artifact but rather seems to be a general property of binaries formed directly by decaying multiple systems without dissipative processes, such as tidal interactions between the fragments. These effects are known to form much harder, spectroscopic binaries resulting in a flatter semi-major axis distribution for small separations, as it was observed for G-stars

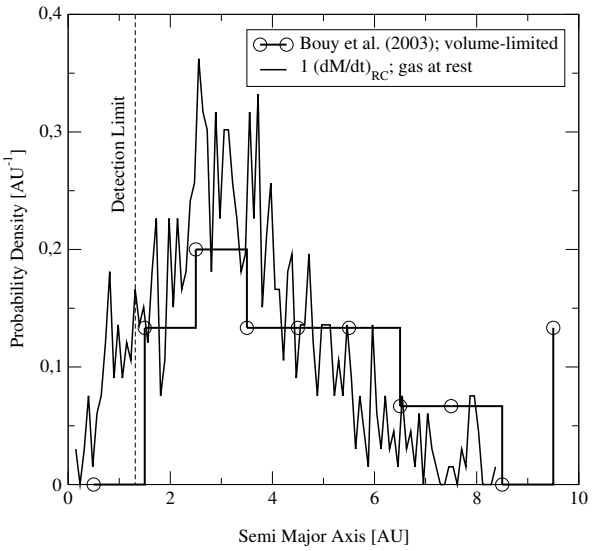

Figure 4.9: Semi major axis distribution of the Brown Dwarf binaries obtained in our simulation of decaying triple systems, accreting gas at rest, and the observed volume-limited sample distribution of Bouy et al. (2003). These two distribution match very well, given the uncertainties (Poisson noise) which are of the order of about a third for the observed distribution. Both distributions have a peak at about the same value of $a = 3\,\mathrm{AU}$ and show about the same degree of asymmetry around the peak.

by Duquennoy & Mayor (1991). If observationally confirmed, the decrease of the semi-major axis distribution to lower separations would indicate that tidal interactions are less important for the formation of Brown Dwarf binaries.

The asymmetric shape of our semi-major axis distribution is similar to the one in Sterzik & Durisen (1998, Fig. 9b), which was obtained by integrating constant mass triple systems with initial masses constrained by an observed stellar IMF as well as a clump mass spectrum for the total cluster mass and scaling the results assuming a constant virial speed. The interesting point here is that our decaying accreting triple systems with equal initial masses seem to *result* in a very similar total energy distribution after they stopped accretion without applying any constraints. It should be mentioned that our semi-major axis distribution is not strongly influenced by the deviation of our initial virial velocities from the $\mathrm{v}_{vir} = const.$-assumption of Sterzik & Durisen (2003). We found that even if we choose only triple systems which have their initial v_{vir} in any very narrow range within the flat part of our initial virial velocity distribution, the asymmetric shape of the semi-major axis distribution is recovered and, moreover, the obtained distributions hardly differ from the one shown in Fig. 4.9.

4.5 Summary and Discussion

In this work we investigated the influence of accretion and gas interaction on the decay of gravitating triple systems and its implications on the viability of the ejection scenario as

Brown Dwarf formation scenario. We have shown that accretion and consequent shrinkage of triple systems increases the velocities significantly compared to non-accreting systems. The high velocities of Brown Dwarfs should make it less likely to find them in star-forming clusters with a shallow potential well and a low escape velocity, but rather in an extended region around it, usually called the Brown Dwarf halo. This would, at a first glance, contradict the rather high abundance of Brown Dwarfs observed in Chamaeleon which have the same spatial distribution as the stellar population (López Martí et al., 2004), but one must also bear in mind that there is still a substantial fraction of Brown Dwarfs in our simulations having escape velocities that are rather low compared to typical escape velocities of low-mass star-forming clusters. These Brown Dwarfs should also share the same kinematics as the stars in the cluster, which would explain why the velocity dispersion of Brown Dwarfs in Chamaeleon is very similar to that of the stars (Joergens & Guenther, 2001). Given that the formation probability of Brown Dwarfs in the ejection scenario can be, in principle, rather high, the high abundance of them in Chamaeleon does not seem unreasonable as long as there is no reliable estimate of the combined potential of stars and the remaining gas. Since in this region there are only a few massive stars, gas removal should be less efficient, therefore increasing the influence of the gas potential. The abundance and spatial distribution of Brown Dwarfs within star-forming regions seems to depend on many parameters, which are observationally not easily accessible making it rather hard to argue convincingly for or against a Brown Dwarf formation model based on these criteria.

Tighter constraints on a Brown Dwarf formation model should be expected from Brown Dwarf binary properties. As already mentioned in section 5.1 the Brown Dwarf binary properties observed so far do not seem to be a natural extension of the binary properties obtained from the standard star-formation model of Kroupa & Bouvier (2003) for hydrogen-burning stars. In general the components seem to be very close and their semi-major axes are distributed in a rather narrow region below $\approx 20\,\mathrm{AU}$. As our simulations show such features are readily obtained if accretion is taken into account during decay. The median of the binary semi-major axis distribution in the case with accretion turned out to be up to 50 times smaller compared to the initial inter-particle distances. This reduction in scale made it possible to start with much larger fragment separations of a few 100AU in order to obtain the observed close Brown Dwarf binaries. This is also the typical length scale on which fragments are formed in collapse calculations of molecular cloud cores. To achieve the same Brown Dwarf binary properties without accretion the fragments must be brought initially in almost unreasonably close configurations as explained in section 4.1, because the typical binary separation is by a factor of up to 5 larger than in the case with accretion.

We were also able to represent the semi-major axis distribution of the volume limited sample of binary Brown Dwarfs of Bouy et al. (2003). A general feature of this distribution is a rather asymmetric shape which can also be obtained by decaying constant mass systems with masses constrained by observed clump and stellar mass spectra as well as assuming a constant virial speed (Sterzik & Durisen, 1998, 2003). The important point to make here is that we were able to *produce* such a semi-major axis distribution without any mass constraints other than our initial masses. Another feature of these distributions is a steep drop off to both sides of the median, which is not observed for G-type binaries (Duquennoy & Mayor, 1991). This is mainly because we did not include such dissipative processes such as tidal interaction between fragments as well as interactions between their disks, which tend to reduce

the binary separations further and circularize their orbits. On the other hand, if this drop-off to lower separations is confirmed observationally, it would provide some evidence that tidal interactions might be less important for the evolution of Brown Dwarf binaries than they are for G-type stars. In general the relative numbers of spectroscopic binaries and those near the median separation should provide evidence for or against a dynamical origin of an observed binary distribution. We also found that the Brown Dwarf binary distribution is not much affected by competitive accretion, as our test calculations of unequally accreting triple systems indicate. This would mean that the distribution depends only to a lesser degree on the detailed distribution of mass within the triple system, but this needs to be confirmed in future studies.

Given the similarities in our distribution to Sterzik & Durisen (1998),it is rather hard to judge from observations how large the influence may be of other constraints, such as the maximum total mass of the cluster determined by the mass of the molecular cloud core.

To answer this question, it would be necessary to investigate how the initial properties of forming clusters relate to the properties of their parental molecular cloud core. Recent studies seem to indicate that they depend strongly on the remaining turbulent velocity field Goodwin et al. (2004); Delgado-Donate et al. (2004), but there is yet no detailed investigation on how this influences the initial properties of the clusters. Delgado-Donate et al. (2004) find wider configurations in their simulations when the index of the turbulent power spectrum α is as high as -5, and closer ones for lower indices, but do not report on other quantities such as initial cluster energy or virial state of the cluster. They further find that for an index of -5 there are fewer Brown Dwarfs forming than at an index of -3. They explain this fact by the occurrence of wider configurations at the $\alpha = -5$-case. An alternative explanation could be given by our model of decaying triple systems accreting gas in 'extreme' motion, as in the case of $\alpha = -5$ the turbulent motion of the gas is on larger scales and, therefore, it is more likely that the accreted gas is adding some momentum to the bodies, even though not as high as we did in our simulations.

We have shown analytically as well as numerically that the probability of forming Brown Dwarfs should be high even for initially moderately compact systems. This is also true without considering competitive accretion, as competitive accretion will increase the number of Brown Dwarfs, which our test simulations of unequally accreting triple systems also indicate. Only if the accretion rate is very high, in our simulations of the order of $10^{-5}\,\mathrm{M}_{\odot} \cdot \mathrm{yr}^{-1}$, forming Brown Dwarfs by ejection seems less likely especially if the accreted gas changes the momentum of the bodies. Our analytical calculation furthermore showed that the reason why the ejection scenario is much more efficient than previously assumed lies in the shrinkage of the system, reflected by the time dependence of R, which causes the energy to decrease further (see eqn. 4.5). It turned out that the total energy, assuming accretion of gas at rest, is proportional to $[(\dot{M}/M_0) \cdot t]^5$ and, assuming gas in extreme motion, it is proportional to $[(\dot{M}/M_0) \cdot t]^3$ while the time dependence under the $R = const.$-approximation is only $\sim (\dot{M} \cdot t)^2/R$. This convincingly explains the very different formation probabilities, resulting from our numerical calculations for the different kinds of momentum transport during mass growth, even though our analytical results differ significantly from our numerical ones. The differences must be due to the fact that the assumption, that the time of the decay can be described as a single exponential function with a half-life directly proportional to the crossing time is not strictly valid, as even varying the half-life of the decay did not reduce this difference significantly.

We can conclude so far that accretion of gas and the kinematic properties of the accreted gas during dynamical interactions strongly influence the abundance as well as the dynamical properties of Brown Dwarfs, and because of the high formation probability and the agreement between our semi-major axis distribution and the observed one of Bouy et al. (2003), makes the ejection scenario a viable option for forming single as well as binary Brown Dwarfs if only three fragments are involved.

Chapter 5

Disks Around Ejected Brown Dwarfs

5.1 Introduction

In this Chapter we investigate disks around Brown Dwarfs that formed by an early ejection out of an unstable accreting triple system. As we already mentioned in Chapter 1, such an early ejection is usually accompanied by a very close encounter with other cluster members. First, this follows from the fact that an encounter leading to escape is usually a close one compared to the initial size of the multiple system (Aarseth et al., 1994). Second, in order for the decay to happen early in time, so that the Brown Dwarf cannot grow beyond the substellar limit, the crossing time of the multiple system has to be short, which in turn requires the initial system to be rather compact. Such encounters have a strong influence on the properties of the disks around the pre-stellar objects. From simulations of star-disk encounters performed by Hall (1997) it became clear that the resulting perturbed disks are truncated down to radii half the closest encounter distance. Consequently, the disks around ejected Brown Dwarfs should be very small and therefore their life times short (Reipurth & Clarke, 2001). On the contrary, active accretion disks have been detected around Brown Dwarfs with an age of up to 10 Myr(Sterzik et al., 2004), which is also the typical life-time of an accretion disk around a TT star (see e.g. Liu et al., 2003). At a first glance, this seems to contradict a severe truncation by close collisions, as due to their shorter life-times they should be less frequently detected, but accretion disks seem to be at least as common around Brown Dwarfs as they are around low-mass stars according to the occurance of $K-$band excess emission (Muench et al., 2001). However, from observations it was also found that the accretion rates of young Brown Dwarfs are about two magnitudes lower than for solar-type stars of the same age, and are typically in the range between $10^{-9}\mathrm{M}_{\odot}\cdot\mathrm{yr}^{-1}$ and $10^{-12}\mathrm{M}_{\odot}\cdot\mathrm{yr}^{-1}$ (Natta et al., 2004; Muzerolle et al., 2003). These low values make it possible, that even very low-mass disks, with masses as low as a few Jupiter masses, are able to survive for 10 Myr, and more, around Brown Dwarfs. Even more so, recent simulations of Padoan et al. (2005) seem to suggest that the observed accretion features, mainly Hα emission, and the accretion rates derived from them are not only due to viscous disk accretion but to a larger extent because of accretion of low-density gas on larger scales of the molecular cloud. Because of the Bondi-Hoyle type of this accretion process, the observationally long established relation between the accretion rate and the mass

of the accreting object, $\dot{M} \propto M^2$, is most elegantly accounted for. For the life-time of severely truncated disks around Brown Dwarfs, this means that the disk accretion rates could have much lower values than the rates derived from the observed line profiles, implying an even larger average life- time for Brown Dwarfs disks for a given disk mass. However, it is so far not very clear if there is enough gas mass on larger scales in typical low-mass star-forming regions to account for the certainly low but not negligible accretion rates (H.Klahr, Th. Henning; private communication). Still, it has to be shown whether close encounter of multiple systems leading to escape will leave disks around Brown Dwarfs massive enough to survive for 10 Myr.

So far, truncated disk sizes were determined after close two-body encounters (Hall et al., 1996; Hall, 1997), where the encounter orbits were usually parabolic ones. For large-N cluster, this type of encounter orbit is assumed to be the most likely one (Ostriker, 1994; Larson, 1990). For close encounter in bound small-N cluster, however, we will typically have more than two bodies approaching at the same time with the result, that these encounter orbits deviate significantly from simple two-body ones. As another consequence, the resulting disk profile should depend on the closest encounter distances of each of the approaching bodies. Although close triple approaches have been investigated extensively in the literature (e.g. Aarseth et al. (1994); Agekian & Anosova (1990, 1991); Anosova & Zavalov (1981)), the closest two-body encounter distances were unfortunately not considered.

The compactness of a multiple encounter also depends on the total size of the system, which is indirectly proportional to its total energy. For accreting triple systems, where this size is getting smaller with time and total mass, the size of the truncated accretion disks will, therefore, depend on the time of decay of that system. Thus, for a given accretion rate and initial compactness, there is a correlation between encounter distances and total mass of the system, with lower-mass systems suffering, on average, less close encounters. Given these additional parameters and the uncertainties regarding the closest two-body distances in the general three-body problem, we find it necessary to investigate this problem in more detail by means of numerical simulations.

The aim of our study is to investigate disk collisions in decaying triple systems that produce Brown Dwarfs by ejection and to estimate the life-times of these strongly perturbed disks around the ejected Brown Dwarfs. Given the computational expense of simulating the entire evolution of a triple system with a disk, we will only simulate the last encounter that finally leads to decay. Although at that time the disk might already have suffered some close triple encounter, the last one in an accreting triple system is, on average, the closest one due to the decreasing total system size.

In section 5.2 we will investigate the encounter parameters of triple approaches leading to escape. In section 5.3 we will describe our simulations of disk collisions in close triple encounters. As the outcome of such a collision depends on many parameters we will first simulate disk collisions in non-accreting triple systems, while we model the disk similar to Hall et al. (1996), i.e. we neglect the influence of gas pressure, viscosity and self-gravity. This way the results are scale-free, which enables us to apply them to accreting triple systems under a variety of initial conditions without the need for further simulations of disk collisions. To account for viscous evolution in strongly perturbed gaseous disks, we will use the result of Clarke & Pringle (1993), that the perturbed and highly eccentric disk material recircularizes quickly

after the encounter, and recircularize our post-encounter disks as well. We then present and discuss the resulting radial surface density profiles and derive relative disk masses for disks around ejected bodies. In section 5.4 we will apply our scale-free model to accreting triple systems and determine their post-encounter sizes. In order to get the absolute disk masses we use typical parameters of accretion disks around observed Brown Dwarfs and derive absolute disk surface densities. In section 5.4.4 we estimate the disk life-time by integrating the evolution equation of the surface density for a Keplerian disk (Lynden-Bell & Pringle, 1974), using the surface density distributions obtained from our disk collision simulations as initial condition. In section 5.5 we will discuss our results and draw conclusions about the evolution and life-time of disks around ejected Brown Dwarfs.

5.2 Close Triple Encounters Leading to Escape

5.2.1 Classification of Close Triple Approaches

Most of the work that has been done on disk collisions only dealt with the case of two-body encounter orbits characterized by periastron distance and eccentricity. As already mentioned in the Introduction, disk collisions in close triple approaches are characterized by at least two encounter distances and the encounter orbits deviate significantly from orbits in the two-body problem.

A classification of encounter orbits in close triple approaches for the general three-body problem with negative total energy is given in Anosova & Zavalov (1981) and Anosova & Orlov (1992). In these studies two basic types of orbits during close triple approaches, named 'fly-by' and 'exchange', have been found. Orbits of the 'fly-by' type are characterized by a close passage of one of the components to the center of mass of the system while the other two bodies form a binary that moves into the opposite direction. Fig. 5.1 and 5.2 show some typical examples. This type of approach leads in most of the cases to the escape of the body passing close to the center of mass (Anosova & Orlov, 1992). Anosova & Orlov (1992) further introduced four subtypes of the 'fly-by' approach based on the deflection angle, defined as the angle between the velocity of the ejected body before and after the triple encounter. They found, that the probability of escape decreases with increasing deflection angle. For close triple approaches of the 'exchange' type the escape probability is even lower. These orbits can be best described as a sequence of two close two-body collisions between the escaper and one body of the final binary, illustrated in Fig. 5.3.

However, the decay probability depends only to a lesser degree on the type of approach and mainly on its compactness, with closer approaches having a higher decay probability than wider ones. In the literature different definitions for the minimum size of a triple system have been used. Agekian & Anosova (1990) defined it as the minimum separation of the most distant body with respect to the center of mass, while Aarseth et al. (1994) determined several geometrical parameters, like the triangular perimeter, at the time when the moment of inertia is at minimum. Although the so obtained minimum sizes were defined at different times of the triple interaction, the average distance between the bodies at those times was always less than the viral system size, confirming that a triple approach leading to escape is always a

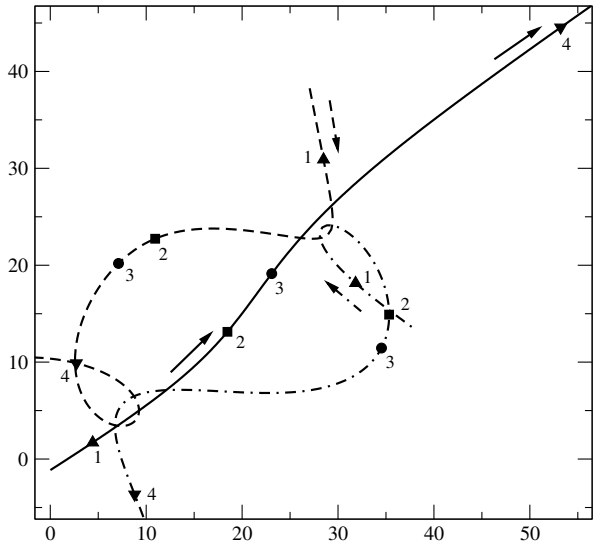

Figure 5.1: A typical example of a 'fly-by' triple approach leading to escape. The solid line shows the escaper orbit while the dashed and the dot-dashed line show the orbits of the bodies that form the binary. Each filled symbol shows the positions of the three bodies at a certain time, with the numbers reflecting the sequence in time. This particular example shows an example of a 'fly-by' of type 1a* according to the classification in Anosova & Orlov (1992), with a value of the deflection angle of the escaper orbit much lower than 20 degree.

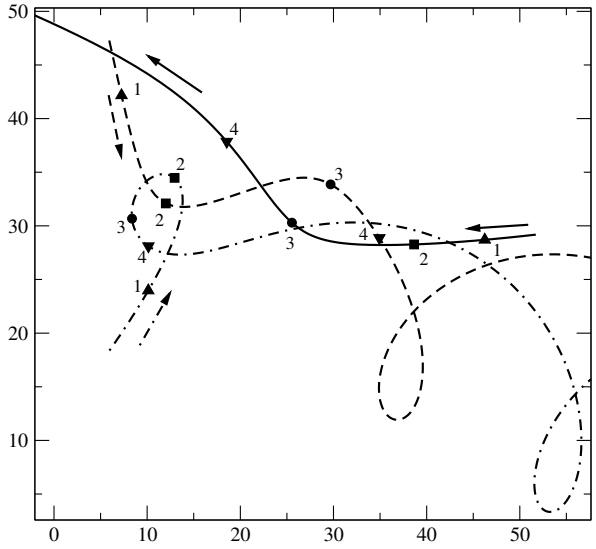

Figure 5.2: A typical example of a 'fly-by' triple approach leading to escape. The solid line shows the escaper orbit while the dashed and the dot-dashed line show the orbits of the bodies that form the binary. Each filled symbol shows the positions of the three bodies at a certain time, with the numbers reflecting the sequence in time. This particular example shows an example of a 'fly-by' of type 1b* according to the classification in Anosova & Orlov (1992), with a value of the deflection angle of the escaper orbit larger than 20 degree.

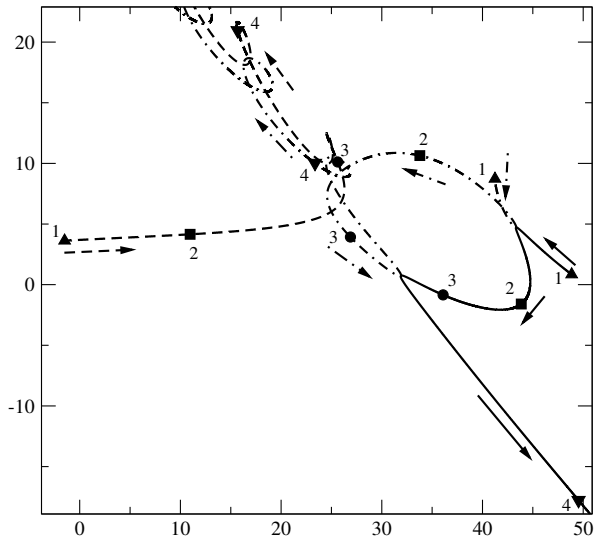

Figure 5.3: A typical example of an 'exchange' triple approach leading to escape. The solid line shows the escaper orbit while the dashed and the dot-dashed line show the orbits of the bodies that form the binary. Each filled symbol shows the positions of the three bodies at a certain time, with the numbers reflecting the sequence in time.

close one. From these minimum triple sizes and geometrical configurations at those minima, there is, however, no simple quantitative relation to the minimum two-body distances due to the complex orbits of the three bodies, and need to be determined by numerical simulations.

Qualitatively, one can already infer some basic properties of disk collisions in triple encounter from the general classification scheme. Here we assume that the disk mid-plane is in the orbital plane of the triple. From the orbits shown in Fig. 5.1 to 5.3 it becomes clear that a disk around the escaper suffers at least two collisions, a prograde and a retrograde one, for a given direction of rotation of the disk. Depending on the encounter distance between the escaper and each of the two other bodies, one of these collision types will dominate the interaction. This is most prominent for 'exchange' encounters, where the difference of these distances usually exceeds a factor of 20. Therefore, disk collisions in exchange encounters can generally be treated like the ones in two-body encounters. However, for encounters of the 'fly-by' type the two-body encounter distances of the escaping body are comparable in most of the cases and we expect that the resulting disk properties will be significantly different from the two-body disk collision results. As another consequence of the vastly different encounter distances in an exchange encounter, the two-body encounter distances are, on average, much smaller than in the 'fly-by' encounter for a given virial size. From the result of Agekian & Anosova (1990), it roughly follows that the minimum separation of the most distant body is always less than $0.65d$, with d being the viral system size, for *both* types of close triple encounters leading to escape. Also, from Fig. 5.3 it becomes clear that a disk around the escaping body in an exchange encounter will suffer two very close two-body encounters of the same kind, either prograde or retrograde, and with the same body of the final binary. Therefore, the results of Hall (1997) regarding multiple disk encounters should be directly applicable in this case.

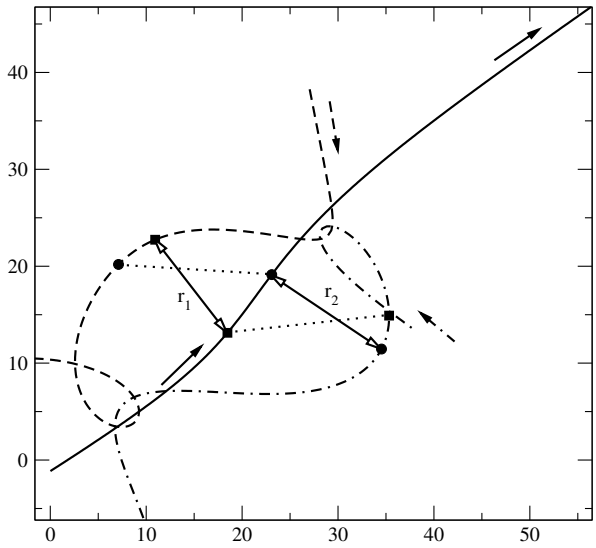

Figure 5.4: Parameterization of close triple approaches suitable for our investigation of disk collisions. r_1, r_2 are the closest two-body encounter distances. The different symbols show the triple configurations at the time a minimum of the distance between the escaper and one of the other bodies is reached.

5.2.2 Encounter Parameter for Disk-Collisions

As we found from the previous discussion, disk collisions in 'fly-by' encounters should deviate the most from pure two-body disk collisions, because of a prograde and retrograde disk encounter happening nearly at the same time with comparable strength. This deviation should be largest if these two encounter distances are equal and should get smaller when their difference gets larger. Therefore, we parameterize disk collisions in close triple approaches by the ratio of r_1/r_2 and r_{min}, with $r_{min} = r_1 < r_2$, where r_1, r_2 are the closest two body encounter distances between the escaper and the other two bodies. Fig. 5.4 shows an example of three-body configurations at the times of the closest two-body distances. For our simulations of disk collisions we do not consider the dependence of our results on the particular shape of an orbit as well as other parameters that influence the outcome of disk collisions. This is mainly because including other parameter would not only increase the parameter space significantly, but is also very difficult to do in a systematic way. For example, the eccentricity of the perturber orbit cannot be easily accounted for as it constantly changes during the encounter and its time dependence differs significantly for different encounters with similar values of r_1/r_2 and r_{min}. For our post-encounter disk models we average over these additional parameter and should, therefore, expect that our results will substantially scatter around the average model.

In order to get a statistically representative sample of encounter orbits of close triple approaches leading to escape, we generate the triple positions according to Anosova (1986, Fig. 1) where all three bodies are initially in the $x-y$-plane and two bodies are always placed at $x = -0.5$, $y = 0$ and $x = 0.5$, $y = 0$. The position of the third body is randomly chosen within a region lying in the positive quadrant and embraced by a unit circle around the point $x = -0.5$, $y = 0$. This arrangement of the bodies has been proven to be a representative sam-

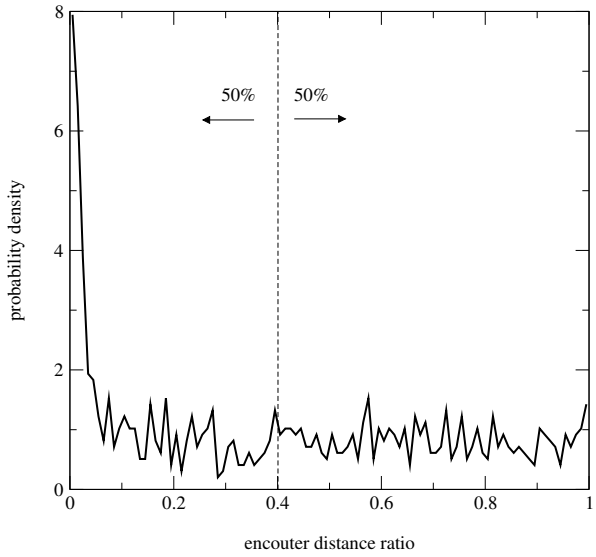

Figure 5.5: Distribution of the ratio of the closest two-body encounter distances r_1/r_2. The dotted line indicates the position of the median, which is at $r_1/r_2 \approx 0.4$.

ple for statistical studies of unstable triple systems by Anosova & Orlov (1994) and should, therefore, also lead to a representative sample of close triple approaches leading to escape. We set the velocities of the bodies to zero initially, as we later want to apply our scale-free results to the ejected Brown Dwarfs obtained in Chapter 4, where we have chosen the same initial conditions in the simulations of accreting triple systems. The integration of the equation of motion is carried out with the CHAIN code of Mikkola & Aarseth (1993) and is stopped if a binary and a single body are separated by more than $7d$ while they are gravitationally unbound to each other. In total we integrated 1000 triple systems and determined the minimum two-body distances and their ratios at the last triple approach.

Fig. 5.5 shows the distribution of r_1/r_2 of the last triple encounter before the triple system decays obtained from our simulation. As it can be clearly seen, r_1/r_2 is uniformly distributed in the range $(0.05, 1)$ and has a strong peak for values below 0.05. This strong peak was to be expected because all the close triple encounters of the 'exchange' type have very small minimum two-body distance ratios and exchange encounters make up 16% of all the close triple encounters leading to escape (Anosova & Orlov, 1992). Taking this into account, the distance ratios of the 'fly-by' encounters can then be assumed to be uniformly distributed in the whole range, which is also consistent with a median value of 0.4 for the entire distribution.

Finally, in Fig. 5.6 we plotted the closest two-body encounter distance r_{min} over the ratio r_1/r_2 for each close triple encounter that lead to escape in our simulation. As it can bee seen, for a given ratio of r_1/r_2 the minimum two-body distance is almost uniformly distributed between some maximum value and nearly zero. As mentioned earlier, due to the fact that there is a maximum size of a close triple encounter above which the triple system does not break up, there is a correlation between the maximum value of r_{min} and the ratio r_1/r_2, which in this case seems to be almost linear. The lower limit of r_{min} does not seem to depend on r_1/r_2 and may get arbitrarily close to zero.

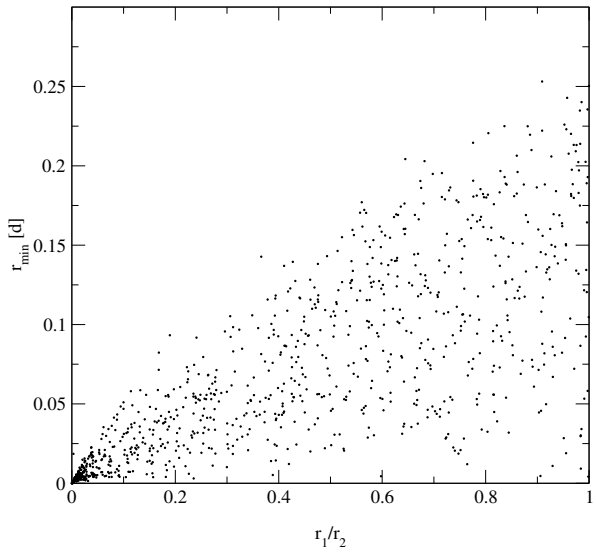

Figure 5.6: Minimum distance r_{min} in units of the mean harmonic distance (virial size) over the ratio r_1/r_2.

5.3 Disk Collisions in Close Triple Encounters

5.3.1 Initial Conditions

After determining the encounter parameter of close triple approaches suitable for the investigation of disk collisions, we now want to study the properties of the highly perturbed disks in dependence on r_{min} and r_1/r_2. We considered 5 different values of r_1/r_2, 0.9, 0.8, 0.6, 0.5 and 0.2. For each of these values we carried out more than 20 realizations of disk collisions in triple systems with varying r_{min}.

For our disks we choose a thin disk model, neglecting pressure forces and self-gravity which implies a low disk mass compared to the central mass, with $M_{disk}/M_{central} < 0.1$. In this case Pfalzner et al. (2005) have shown that the self-gravity and pressure forces of the disk can be neglected. Even for a mass ratio as high as $M_{disk}/M_{central} = 0.1$ the angular momentum and mass transfer is in principle very similar to lower-mass disks apart form a pronounced "eigen-evolution" of the disk after the collision which is due to its self-gravity. However, in our case we do not expect this eigen-evolution to be a dominant effect because our disks are much less massive after the encounter, owing to the much stronger interaction in a close triple encounter compared to the much wider encounter in Pfalzner et al. (2005).

The disk is composed of $10,000$ test particles initially placed on circular orbits and distributed axial-symmetrically according to a given radial surface density distribution, which we have chosen as $\Sigma = \Sigma_0 \cdot (r_0/r)$, with Σ_0 being the surface density at r_0. The structure of disks around very young, deeply embedded objects is still significantly influenced by the infall of matter from their accretion envelope and hydrodynamical simulations show that the surface density profiles of these disks are generally rather flat (see e.g. Lin & Pringle (1990) and Yorke

& Bodenheimer (1999)). Therefore, choosing $\Sigma \propto r^{-1}$ for our disk profile seems reasonable, especially compared to the profile $\Sigma \propto r^{-1.25}$ obtained by Lin & Pringle (1990). In addition, choosing a flat profile increases the amount of material that gets stripped off the disk as more particles are initially in the outer disk compared to steeper disk profiles.

In our simulations we only consider cases where the disk mid-plane coincides with the orbital plane of the triple system, making the disk collisions coplanar. As this type of collision is most destructive to the disk we overestimate the amount of material that gets stripped off the disk and consequently underestimate the final disk mass. However, the results of Hall et al. (1996) indicate that this effect should be rather small, as the amount of material that remained bound in their simulations hardly changed with inclination. The effect on the disk profile, however, should be larger because of the larger differences in the energy and angular momentum transport, and needs to be quantified for disk collisions in triple systems in a future study.

In absence of detailed hydrodynamical calculations of triple systems in collapsing molecular clouds we can only speculate about the initial size of the disk before the last encounter. It seems plausible to us that it should be less than the mean harmonic distance d of the triple and choose, therefore, an initial radius of $d/3$ for our calculations. Although it is likely that the escaping body already suffered a two-body collision that was closer than the one at the last triple encounter, we restrict ourselves to those cases where the last encounter dominates the resulting disk profile. If the disk is much smaller due to a previous encounter, the effect of the last encounter on the disk is rather low, so the properties of the disk in that case are mainly determined by triple encounters that do not lead to escape. The systematic investigation of the much larger parameter space of these encounter types is, however, beyond the scope of the present work. Apart from that, we might expect that due to the infall of material in a collapsing cloud core, the disk should constantly gain mass as long as it resides in the core, which should partly compensate the mass loss due to previous close encounters.

For all of our calculations we choose a fixed radial extent of the disk, ranging from 0.1 to 20 AU, covering more than two orders of magnitude in radius. We then adjust d, the mean harmonic size of the triple system, so that the outer radius of the disk corresponds to $1/3\,d$. In order to reduce the effect of the artificial inner boundary we only carry out disk collisions with $r_{min} > 1.5\,\mathrm{AU}$. We start our calculations at a time when the maximum separation between two bodies is $1d$ and stop if it is more than $4d$. Although we found that varying the initial separation influences our results significantly, there was no systematic change. This is mainly because of the rather chaotic motion of the triple system before the last encounter, resulting in very different initial orbital configurations at a given maximum separation of the bodies for different triple encounters even if those encounters have very similar values r_1/r_2 and r_{min}. Together with the neglect of all the other parameters mentioned in section 5.2.2 this should reduce the direct correlation between the post-encounter disk profiles and our set of encounter parameter. As we will find later, the correlation is still strong enough to allow for a scale-free model.

In order to integrate 10,000 test particles efficiently one has to make a compromise between accuracy and runtime. While the motion of the triple system can be integrated with a median accuracy of 10^{-12} in total energy within a very short time using the CHAIN algorithm (Mikkola

& Aarseth, 1993), to maintain such an accuracy level during the whole disk collision calculation for the motion of the test particles would require a huge amount of CPU time. The main reason for this is the rather large radial extent of our disk and the extremely small time scale of the motion of particles with small disk radii compared to the crossing time of the triple system. We therefore decided to integrate the test particle motion with the 5th order Runge-Kutta Cash-Karp scheme (see Press (1993)) with adaptive time-step control, which conserved the total energy of an undisturbed disk with an accuracy of 10^{-6} over 10 orbital periods of the outer rim of the disk. This makes it possible to integrate many realizations of disk collisions in triple encounters while still ensuring a reasonable accuracy of the particle motion over the time of integration, which was on average between 10 and 20 outer orbital periods in our simulation runs.

In our code we use two integration schemes to advance the entire system in time, the CHAIN algorithm for the triple system and the Runge-Kutta scheme for the mass-less disk particles. Because of the smaller time scale of the particle motion around the ejected body, the particles are advanced on smaller timesteps compared to the much larger time-steps of the triple system. To couple the particle motion to the motion of the triple system, the force of the triple system acting on the mass-less particles is treated as a time varying external force in the Runge-Kutta scheme. In order to obtain this force at a time required by the Runge-Kutta scheme, the triple system is integrated from a previous configuration of a regular CHAIN step up to this particular point. The triple configurations obtained at those times are, however, not used to advance the triple system further. This is to reduce the influence of accumulating round-off errors caused by having a much larger number of CHAIN steps than actually required by the corresponding accuracy criterion.

5.3.2 Disk Profiles

Fig. 5.7 shows a typical example of a recircularized radial surface density disk profile after a close triple encounter, together with its initial profile in a log-log diagram. Many features of the radial disk profile seen in this diagram are similar to the results for parabolic two-body encounters investigated by Hall (1997), e.g., the disks are severely truncated and the surface density drops by orders of magnitudes in the outer disk regions. Also, the inclusion of the viscous evolution of the disk by recircularizing the disk material further depletes the outer disk regions, because at larger radii the disk material looses much angular momentum and, therefore, ends up at smaller radii (Hall, 1997; Hall et al., 1996). This has also the effect that in the inner regions of the disk the surface density is enhanced relative to the initial density. We also find, as in Hall (1997), that the surface density of the outer parts of the disk can be described by an exponential function. However, Hall (1997) gave no detailed description of the radial structure of the inner disk, where most of the disk mass resides.

From our simulations we found that most of our disk profiles can be divided into three distinct regions, a power-law region with $\Sigma \propto r^{-1}$ for disk radii below $0.2 r_{min}$ and two regions, located between 0.2 and $0.7 r_{min}$and above $0.7 r_{min}$, where the surface density decreases exponentially as $\Sigma \propto \exp(\log(1/2)\, r/\tau)$, with the outer region being flatter, i.e. having a larger full-width-half-value τ, than the inner one. At $0.2 r_{min}$ Kobayashi & Ida (2001) also find that the structure of the disk is changing by investigating the eccentricity change of the disk material after a

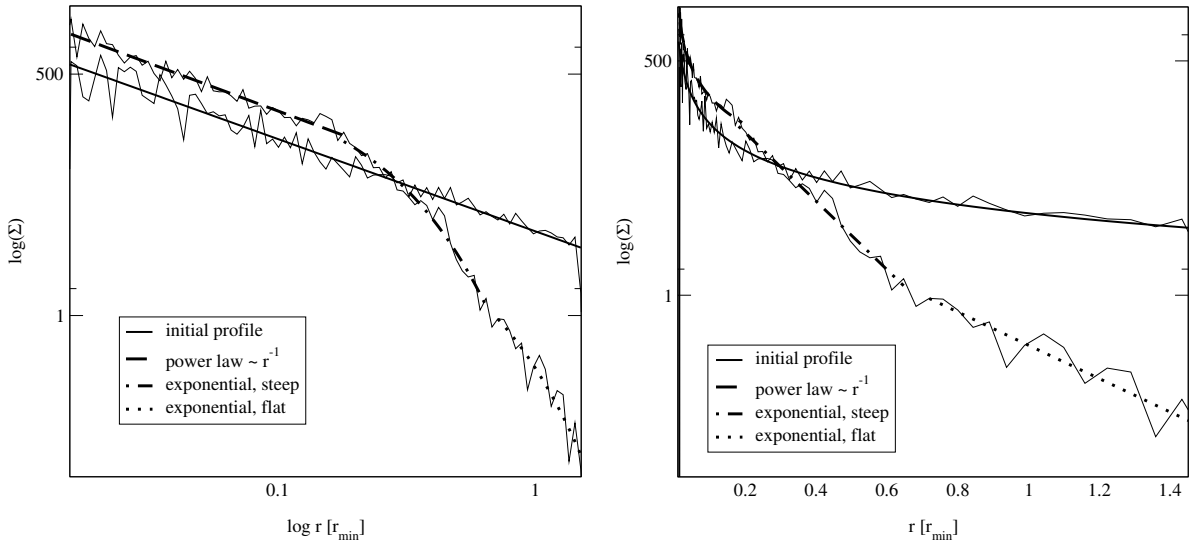

Figure 5.7: Model of the truncated accretion disk surface density profile. Shown is the initial as well as the truncated, recircularized profile, with the thin solid lines representing the profiles from one of our simulations and the bold lines the fitted curves on a log-log scale (a) and on a semi-log scale (b). The recircularized profile can be divided into three different regions. Below $0.2\,r_{min}$ it has the same power-law shape as the initial profile, but with Σ increased by a factor of ≈ 1.7. For larger disk radii there are two regions, between $0.2\,r_{min}$ and $0.7\,r_{min}$ and above $0.7\,r_{min}$, that can be fitted with an exponential profile, $\Sigma \propto \exp(\log(1/2)\,r/\tau)$, having different slopes, τ_1 and τ_2 (here $\tau_1 \approx 0.064 r_{min}$ and $\tau_2 \approx 0.2 r_{min}$).

prograde encounter. Inside that radius the disk is only weakly perturbed, whereas outside of it, resonances lead to strong perturbations. Although only strictly valid for parabolic encounters, they also find that this boundary is only weakly dependent on the eccentricity of the perturber. In our simulations the eccentricity of the perturber with the closest encounter distance was always below 2.5 at the time of closest approach and therefore the region was at most shifted to $0.24 r_{min}$ which can be neglected given the uncertainties in our fits.

As already mentioned, in the inner power-law region the surface density is enhanced relative to the initial surface density and as we can see here, it is increased by a constant factor, which varied in our simulations between 1.5 and 2. This factor is similar to the surface density enhancement for the parabolic, retrograde encounters of Hall (1997) at $r = 0.4 r_{min}$, although in all our runs we observed this increase at somewhat lower radii. This might be partly due to the influence of the prograde encounter, as Hall (1997) observes the enhancement at $0.25 r_{min}$ for this case, but also because of the, on average, higher eccentricity at the time of closest approach. Another consequence of the higher eccentricity of the orbits might be that the density enhancement never exceeded a factor of 2, in contrast to the prograde, parabolic encounters in Hall (1997), where the surface density was 5 times higher than its initial value. However, as we will see in section 5.3.3, even when the eccentricities are close to the parabolic case, the disks surface densities are not as strongly enhanced in the inner region as in that case, which indicates that the higher eccentricities have a rather limited influence on the disk structure. The reason for the lower surface density enhancement has rather something to do with the dynamics of the triple encounters that cannot be sufficiently described in terms of two-body encounters, as we will discuss in section 5.3.3.

In order to find out how the surface density profile is related to the encounter parameter r_{min} and r_1/r_2, we fitted for each of our obtained post-encounter disk profiles two exponential functions to the outer two regions and determined the full-width-half values τ_1, for the region between 0.2 and $0.7 r_{min}$, and τ_2, for the region outside $0.7 r_{min}$. We then plotted these values over r_{min} for each r_1/r_2 separately. We found that, while the uncertainties of the values for τ_1 where mostly between 2% and 10%, they were much larger for τ_2, mainly because of the much lower number of particles left in the outer regions of the disk. In those regions many particles are stripped off the disk and the remaining ones are recircularized to smaller radii, due to their much smaller angular momentum. Therefore, we can give for most of the r_1/r_2 values we investigated only upper limits for τ_2.

Fig. 5.8 to 5.12 show τ_1 in dependence on r_{min} for different values of r_1/r_2. In all cases τ_1 increases with increasing r_{min} which means that for larger r_{min} the radial surface density disk profile gets flatter in this region. Furthermore, τ_1 seems to depend linearly on r_{min}. However, we find that the scatter of the values around this function is much larger than the uncertainties in determining τ_1. As already mentioned in section 5.2.2 and 5.3.1 the reason for the large scatter is because of the reduction to only two parameters describing the much more complex triple interaction. Furthermore, we find no significant difference between triple collisions, where the disk suffered a retrograde or a prograde encounter at the time the ejected body reached the closest encounter distance r_{min}. This indicates that the orientation of the disk plays only a minor role and most of the uncertainty comes from the complexity of the encounter orbit.[1]

[1] Also, we did not find that the deviations of τ_1 correlate with any other parameter we investigated, like the

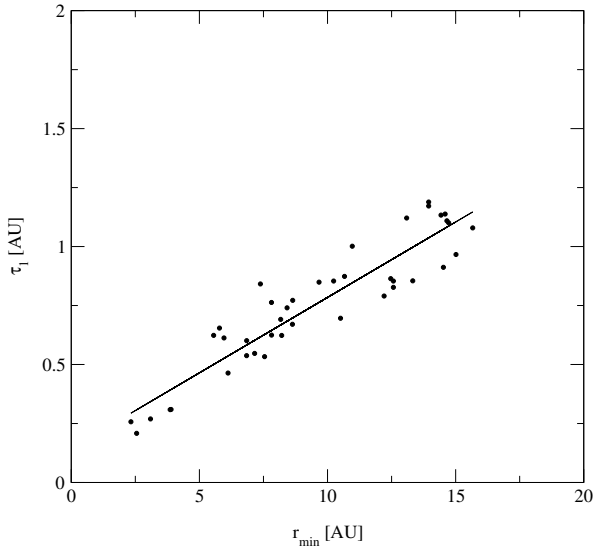

Figure 5.8: Full-width-half-value τ_1 over the smallest encounter distance r_{min} for $r_1/r_2 \approx 0.95$. The behavior can be approximately described by a linear function, with a slope of 0.064 ± 0.005. However, the deviations from this linear function cannot be explained by the errors of τ_1. For r_{min} larger than 10 AU τ_1 scatters more strongly than for values below 10AU, which cannot be directly correlated to any other change in the orbital parameters of the triple encounters.

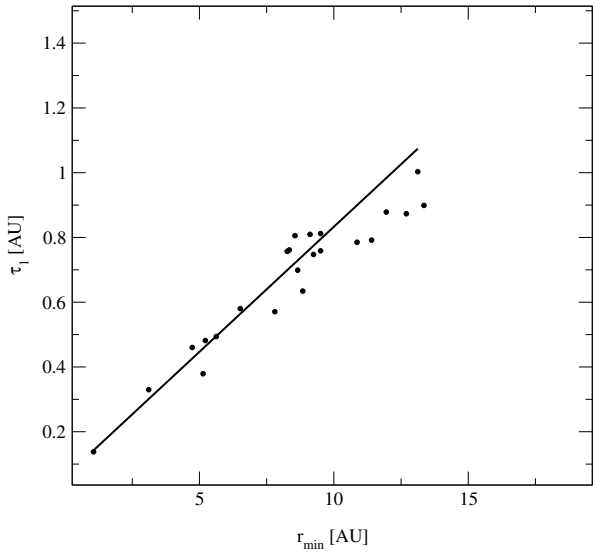

Figure 5.9: Full-width-half value $\tau_1$over the smallest encounter distance r_{min} for $r_1/r_2 = 0.8$. It can be approximately described as a linear function, with a slope of 0.076 ± 0.006. As in the case of $r_1/r_2 \approx 0.95$, for values of r_{min} above 10 AU the values of τ_1 seem to deviate more strongly, whereby here they are always below the average linear increase for $r_{min} < 10$ AU.

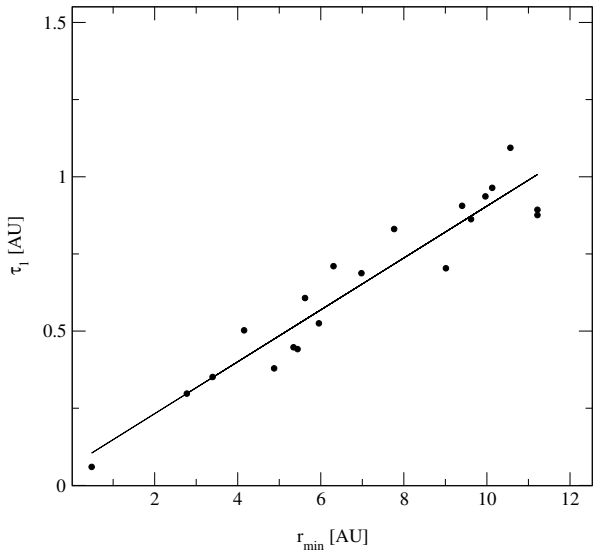

Figure 5.10: Full-width-half-value $\tau_1$over the smallest encounter distance r_{min} for $r_1/r_2 \approx 0.6$. The solid line is the linear fit to the data, with a slope of 0.084 ± 0.005. This value is very similar to the ones obtained for other r_1/r_2 in the same range of $r_{min} < 10\,\mathrm{AU}$.

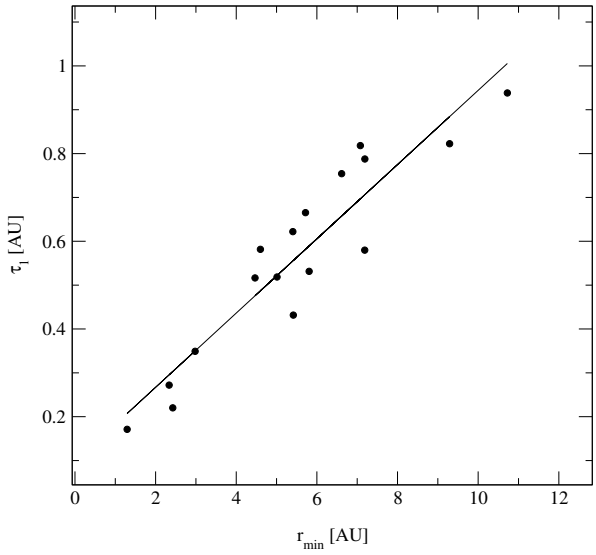

Figure 5.11: Full-width-half-value τ_1 over the smallest encounter distance r_{min} for $r_1/r_2 \approx 0.5$. The solid line is the linear fit to the data, with a slope of 0.085 ± 0.008. Although higher than for other values of r_1/r_2, the slope is not significantly different, given the rather large scatter of the data.

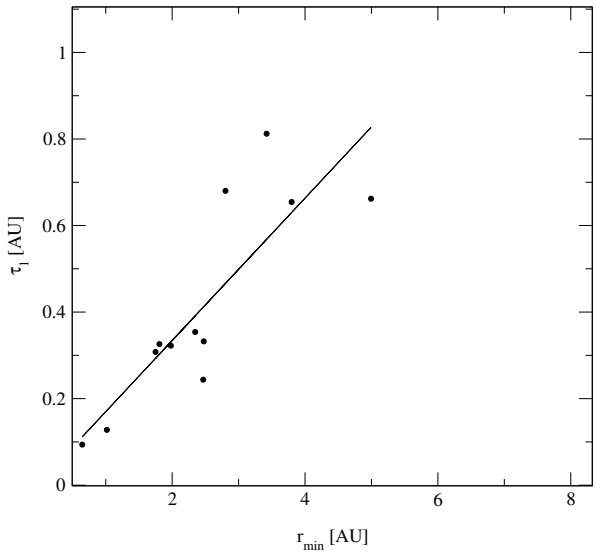

Figure 5.12: Full-width-half-value τ_1 over the smallest encounter distance r_{min} for $r_1/r_2 \approx 0.2$. The solid line is the linear fit to the data, with a slope of 0.16 ± 0.03. Despite the rather larger scatter, the slope is significantly higher than for larger values of r_1/r_2.

For each of the values of r_1/r_2 we determined the slope of the linear fit with the corresponding error and plotted these values over r_1/r_2 in Fig. 5.13 . As can be readily seen, for values of r_1/r_2 lower than 0.5 there is only a weak increase in the slope of $\tau_1(r_{min})$ and, considering the errors, it is not absolutely certain if the slope at $r_1/r_2 = 0.5$ is really larger than the one at $r_1/r_2 = 0.95$ or if this is an effect of the limited number of points available for the fit. In addition, one should also consider that the amount of angular momentum transferred from the orbit of the triple systems to the disk depends on the relative size of the disk, with respect to r_{min}, (Hall et al., 1996) and, therefore, influences the radius of the recircularized disk material as well as the overall density distribution. The results of Hall et al. (1996) clearly show that the angular momentum transport is not a simple function of the relative disk radius and, therefore, the dependence of the recircularized disk profile on the encounter radius is usually not the same for different r_{min}. Since the range of r_{min} was lower for $r_1/r_2 = 0.5$ than for $r_1/r_2 = 0.95$ as shown in section 5.2.2, the lower value of the slope of $\tau_1(r_{rmin})$ for $r_1/r_2 = 0.95$ could also be caused by a change of the functional dependence of the angular momentum transport for encounters with $r_{min} > 10\,\mathrm{AU}$ for our disks , which corresponds to disks radii lower than $2r_{min}$. This assumption is supported by the angular momentum transfer curves for prograde parabolic encounters in Hall et al. (1996, their Fig. 7b). For retrograde encounters there is no such change but since for $r_1/r_2 = 0.95$ the retrograde and prograde encounters are nearly of equal strength, the prograde encounter will always affect the disk profile significantly.

For encounters with $r_1/r_2 < 0.5$ we find that the slope of $\tau_1(r_{min})$ increases much stronger and nearly all values of τ_1 for $r_1/r_2 = 0.2$ were larger than the corresponding values for $r_1/r_2 \geq 0.5$.

eccentricity of the perturber and the escape velocity of the ejected body. We therefore come to the conclusion that the value of τ_1 must depend on many parameters in a rather complex way, which, in order to investigate further, would require us to cover a much larger parameter space than we can currently study.

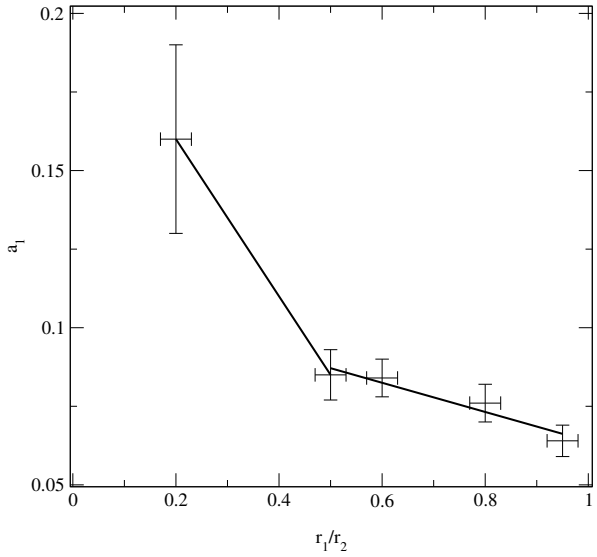

Figure 5.13: Slope of the linear change of τ_1 with r_{min} over r_1/r_2. The error bars of the slope represent the errors of the linear fit which were always larger than the errors of the individual τ_1. The horizontal error bars represent the r_1/r_2-intervals from which we have chosen the individual triple collisions.

This clearly shows that at least in this regime the radial surface density distribution depends strongly on the parameter r_1/r_2 and leads to disk profiles which are generally much flatter for lower values of r_1/r_2.

For the application of these results to encounters with different values of r_1/r_2 we fitted the data in the range $(0.5, 1)$ linearly and for lower values we interpolate between the points at $r_1/r_2 = 0.5$ and $r_1/r_2 = 0.2$, as shown by the solid lines in Fig. 5.13.

As mentioned earlier, the uncertainty in the values or τ_2 are much larger than they are for τ_1 because of the lower number of particles left in the outer disk regions. Only in the case of $r_1/r_2 = 0.2$ we could determine τ_2 with comparable accuracy as τ_1. Consequently, only in this case it was possible to determine the slope a_2 of $\tau_2(r_{min})$ with a value of 0.2 within an uncertainty of 15%. In all the other cases we can only say that a_2 must be between 0.1 and 0.2. Based on our data we did not find that the slope changes with r_1/r_2 and therefore assumed for the further discussion a value of $a_2 = 0.2$ for all r_1/r_2. Although, that is an overestimate for most of our disks after a triple encounter with $r_1/r_2 \geq 0.5$, this choice has little or no influence on our further simulations of the viscous evolution of the disk, as we will see that in those cases the outer parts of the disk contain less than 6% of the total disk mass.

From these results we can now construct a scale-free model of the post-encounter radial surface density profile by substituting $\tau_{1,2}$ with the linear fits we obtained for the different values of r_1/r_2 and taking into account the density enhancement relative to the original disk profile for the region below $0.2r_{min}$ by multiplying it with a constant factor k. Thus, the surface density

profile takes the following form:

$$\Sigma = \Sigma_0 \cdot k \cdot \begin{cases} \frac{r_0}{r} & ; r \leq 0.2 r_{min} \\ \frac{r_0}{0.2 r_{min}} \cdot \tilde{a} \cdot \exp\left(\log(1/2) \cdot \frac{r}{a_1 r_{min}}\right) & ; 0.2 r_{min} < r < 0.7 r_{min} \\ \frac{r_0}{0.2 r_{min}} \cdot \tilde{a} \cdot \tilde{b} \cdot \exp\left(\log(1/2) \cdot \frac{r}{a_2 r_{min}}\right) & ; r \geq 0.7 r_{min} \end{cases} \tag{5.1}$$

where r_0 is the radius at which the initial profile has a value of Σ_0 and $\tilde{a}$ and $\tilde{b}$ are constants chosen to ensure that Σ is a steady function and are given by

$$\begin{aligned} \tilde{a} &= \exp\left(\log(1/2) \cdot \frac{0.2}{a_1}\right)^{-1} \\ \tilde{b} &= \exp\left(\log(1/2) \cdot 0.7 \left(\frac{1}{a_1} - \frac{1}{a_2}\right)\right)^{-1}. \end{aligned}$$

The values of $a_{1,2}$ for a given value of r_1/r_2 are chosen according to our linear fits shown in Fig. 5.13. By replacing $\tau_{1,2}(r_{min})$ with $a_{1,2} r_{min}$ we neglect the small positive intercept of the linear fits for simplicity, underestimating the values of $\tau_{1,2}$ in our model. Therefore, the derived absolute disk sizes and masses represent lower limits.

5.3.3 Relative Disk Masses

From our model surface density profile we can now determine how the total disk mass changes with r_{min} for a given value of r_1/r_2 and calculate the size of the disk, where we define this size as the radius $r_{90\%}$ within which 90% of the total disk mass is contained. We can then compare the disk sizes with the result from parabolic two-body disk encounters of Hall et al. (1996), who found $r_{90\%} = 0.5 r_{min}$ [2].

In order to obtain the disk mass M_D from our model we integrate equation 5.1 over the radius r

$$M_D = 2\pi \cdot \int_0^\infty r \cdot \Sigma(r). \tag{5.2}$$

The general solution can then be written in the form

$$M_D = 2\pi \cdot k \cdot \Sigma_0 \cdot r_0 \cdot (0.2 + M_1(a_1) + M_2(a_1, a_2)) \cdot r_{min} \tag{5.3}$$

where $M_{1,2}$ are the relative masses of the outer, $r \geq 0.2 r_{min}$, disk regions with respect to the mass of a disk with $\Sigma \propto \frac{1}{r}$ extending to r_{min}. As it can be seen, in our model the disk mass is directly proportional to r_{min} for given values of $a_{1,2}$, which is also consistent with the disk masses we get from our simulations, shown in Fig. 5.14 to 5.18. In these figures we plotted for each value of r_1/r_2 the masses of the disks in units of the initial disk mass over r_{min} and found that the values are linearly correlated with a correlation factor larger than 95%. The values of $M_{1,2}$ together with $r_{90\%}$ for each value of r_1/r_2 we investigated are shown in table 5.1. Also shown is the fraction of the total post-encounter disk mass that is contained within

[2] Here r_{min} corresponds to the periastron distance.

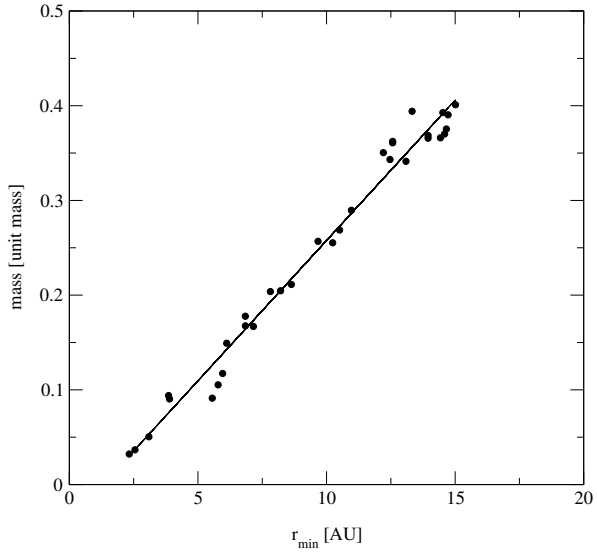

Figure 5.14: Disk mass in units of the initial disk mass over the smallest encounter distance r_{min} for $r_1/r_2 = 0.95$. The solid line is the linear fit to the data, with a slope of 0.0296 ± 0.0007.

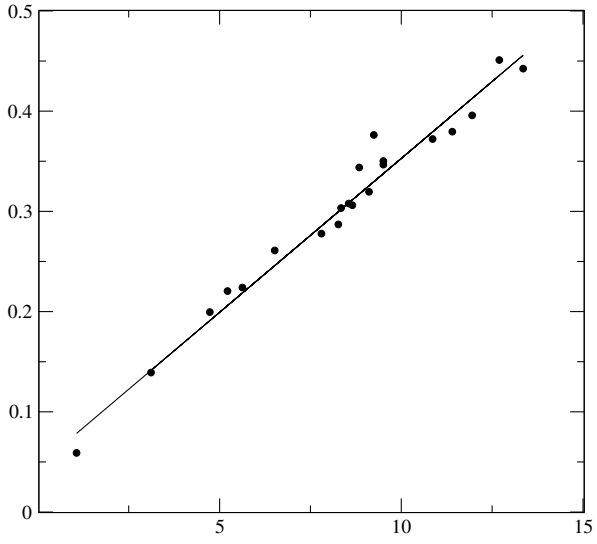

Figure 5.15: Disk mass in units of the initial disk mass over the smallest encounter distance r_{min} for $r_1/r_2 = 0.8$. The solid line is the linear fit to the data, with a slope of 0.031 ± 0.001.

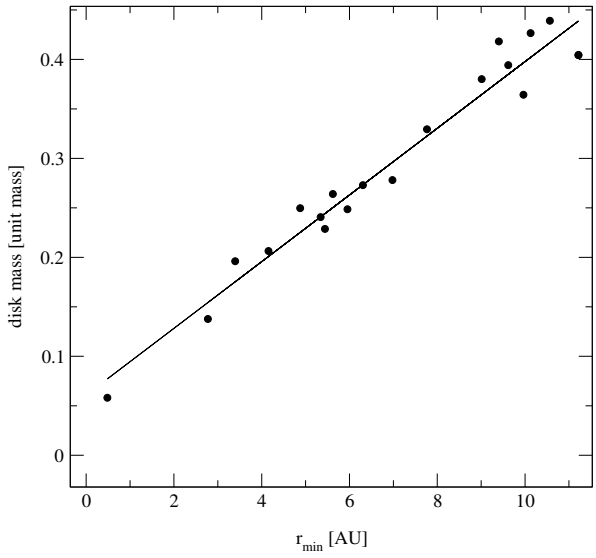

Figure 5.16: Disk mass in units of the initial disk mass over the smallest encounter distance r_{min} for $r_1/r_2 = 0.6$. The solid line is the linear fit to the data, with a slope of 0.034 ± 0.002.

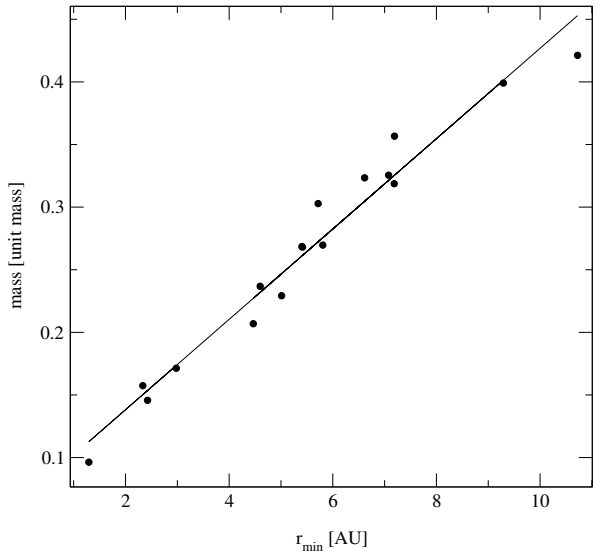

Figure 5.17: Disk mass in units of the initial disk mass over the smallest encounter distance r_{min} for $r_1/r_2 = 0.5$. The solid line is the linear fit to the data, with a slope of 0.036 ± 0.002.

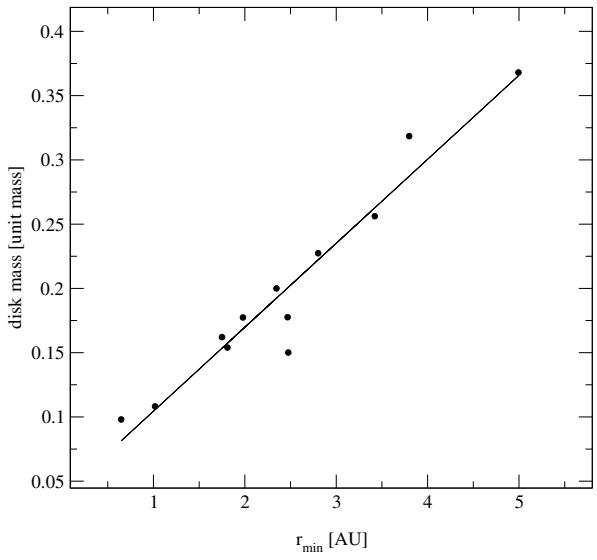

Figure 5.18: Disk mass in units of the initial disk mass over the smallest encounter distance r_{min} for $r_1/r_2 = 0.2$. The solid line is the linear fit to the data, with a slope of 0.065 ± 0.005.

r_1/r_2	M_i	M_1	M_2	$r_{90\%}(r_{min})$
0.95	0.2 (60%)	0.13 (38%)	<0.006 (2%)	0.38
0.8	0.2 (52%)	0.17 (44%)	<0.015 (4%)	0.49
0.6	0.2 (49%)	0.19 (46%)	<0.02 (5%)	0.52
0.5	0.2 (49%)	0.19 (46%)	<0.02 (5%)	0.52
0.2	0.2 (27%)	0.37 (51%)	0.16 (22%)	1.0

Table 5.1: Relative mass fractions $M_{i,1,2}$ with respect to the mass of a disk with $\Sigma \propto \frac{1}{r}$ and radius r_{min}, and the 90%-mass-radii $r_{90\%}$ for our disk models with different values of r_1/r_2. M_i is the mass contained in the inner region below $0.2r_{min}$ and $M_{1,2}$ are the masses in the outer two regions. In parenthesis the mass fraction with respect to the total post-encounter disk mass is given.

the three different disk regions.

This table clearly shows that for $r_1/r_2 \geq 0.5$ there is only a very small amount of mass contained in the outer region of the disk with $r \geq 0.7r_{min}$ and more than 95% of the disk mass is within $0.7r_{min}$, making the post-encounter disk very compact. Therefore, the outer part of the disk will have little effect on the further dynamical evolution of the disk we later want to investigate and, thus, the rather large uncertainty of the disk profile and mass for this region, which is of the order of 50%, does not have a significant influence. Furthermore, we find only a weak increase in mass in the region between $0.2r_{min}$ and $0.7r_{min}$ for decreasing $r_1/r_2 \geq 0.5$, as it was to be expected from the results of $\tau_1(r_{min})$. Comparing this mass with the mass that is contained within $0.2r_{min}$ we find that they are nearly equal, given the errors of about 10% for M_1. Only in the case with $r_1/r_2 = 0.95$ there seems to be more mass contained in the innermost region, with about 60% of the total disk mass.

Because of the strong increase of $\tau_{1,2}$ for $r_1/r_2 = 0.2$, as shown in section 5.3.2, we also have a strong increase in mass contained in the outer disk regions for this case. As a consequence, these disks are no longer strongly concentrated and appear to be much flatter, as now there are only about 78% of the total disk mass contained within $0.7r_{min}$ as opposed to more than 95% for $r_1/r_2 \geq 0.5$. In contrast to disk encounters with $r_1/r_2 \geq 0.5$ the outermost part of the disk now contains almost a quarter of the total mass of the disk and most of its mass is contained in the region between $0.2r_{min}$ and $0.7r_{min}$. This comes close to the corresponding values for a disk with $\Sigma \propto \frac{1}{r}$ truncated at a radius $1r_{min}$.

Up to this point, we completely specified the disk profile as shown in eqn. 5.1 apart from a constant k, which specifies how much the surface density in the inner disk region below $0.2r_{min}$ is enhanced relative to the initial surface density. As in that region we are severely limited by noise, fitting each single profile for that region to determine this constant is rather problematic. The reason for this is that the surface density in our simulation is rather noisy in the inner parts of the disk. Therefore the power-law indices of the fits usually deviate from -1 which makes the corresponding constant factor much more uncertain. We, therefore, determined k by exploiting eqn. 5.3 and the linearly fitted disk masses in Fig. 5.14 to 5.18, because the determination of the masses are based on a larger number of particles than that of the inner disk profile.[3] For the determination of k, we expressed eqn. 5.3 in terms of the initial disk mass $M_{init} = 2\pi \cdot \Sigma_0 r_0 \cdot (r_{out} - r_{in})$, where r_{out} is the outer and r_{in} the inner initial disk radius. We then inserted the values from table 5.1 for each r_1/r_2 and set the numeric value of the slope of $M(r_{min})$ equal to the corresponding slope of the fits, thus obtaining k. In all cases we found that $k = 1.7 \pm 0.1$, which lies also in the range we roughly expected from the disk profiles in section 5.3.2. Since this factor does not seem to depend on r_1/r_2, it follows that a flatter disk profile implies a larger total disk mass. From this it follows further, that in general the masses of the post-encounter disks increase with decreasing r_1/r_2, which also agrees with our results shown in Fig. 5.14 to 5.18.

If we consider the actual values of the masses we find than our disks have at most 40% of the initial disk mass and in most cases much less than 30%. To relate our masses to the disk masses after two-body collisions we use the result of Hall et al. (1996) who found that the post-encounter disk has only one third of the initial mass for a disk radius of $4r_{min}$. As

[3] We thus assume that the inner profile is strictly a power-law with index -1.

our disk radius is always 20AU this means that for each r_1/r_2 the corresponding disk mass in our case is the one at $r_{min} = 5$AU. From our model we find values ranging from 15% to 18% of the initial disk mass for $r_1/r_2 \geq 0.5$. For the case of $r_1/r_2 = 0.2 r_{min}$ it is 33%. This reflects the trend we intuitively would expect, as for larger values of r_1/r_2 we have roughly speaking two two-body encounters with similar strength and consequently more stripping of disk material, whereas for lower values of r_1/r_2 we are getting closer to a single two-body encounter. In addition, we also find that this trend is strongly non-linear and not a simple function of r_1/r_2. The fact that in a triple encounter we only find the same disk mass for $r_1/r_2 \leq 0.2$ has the direct consequence, together with the distribution of r_1/r_2 shown in 5.5, that the majority of close triple encounters is more destructive than the corresponding two-body ones and only in one third of the cases we should get at least comparable disk masses. However, the convergence of the disk masses for smaller r_1/r_2 is not as trivial as it might sound, because we also find that the influence of the third body in the case of $r_1/r_2 = 0.2$ is still significant. In order to demonstrate this effect, we carried out a calculation for one particular triple encounter where the disk is only affected by the escaper and the body with the closest encounter distance r_{min}, but otherwise leave the orbits of the bodies unchanged. In that example we find that the post-encounter disk mass is increased by almost 10% of the initial disk mass which makes the post-encounter disk mass 33% larger compared to the case, where the disk is affected by all three bodies. As we find that for the $r_1/r_2 = 0.2$-case the disk masses are comparable to the two-body case it directly follows that the orbits in a triple encounter tend to increase the mass of the disk while the presence of the third body reduces it. We therefore expect that for ratios $r_1/r_2 \leq 0.2$ the trend for higher disk masses at a given r_{min} is continued.

From our simulation we believe that this mass increase compared to the results of a two-body disk encounter is closely related to the formation of the final binary after the triple encounter. To show this, we compared in Fig. 5.19 the distance between the escaper and the body of the binary with the smallest encounter distance r_{min} and the distance, these bodies would have if they moved on a hyperbolic orbit with the same eccentricity at $r = r_{min}$. As it can be clearly seen, the distance between the bodies in the triple system is almost always lower than in the two-body case, leading to an enhanced interaction time which is much larger than 5 dynamical times found for the parabolic two-body case by Hall et al. (1996) (one dynamical time is the ratio of r_{min} over the velocity v_{min} at that point). The lower distances before the encounter are present because the bodies do not approach each other from an infinite distance but are in a bound system with finite size. The lower distances after the encounter are due to the formation of a binary where one of the two bodies is slowed down relative to the escaper because of the presence of the third body. For the disk around the escaper this means, on the one hand, that the disk starts loosing material earlier in the encounter than it would do in a hyperbolic encounter. On the other hand, due to the lower values after the encounter, particles that became unbound after the closest collision are slowed down again and could be re-captured by the escaper or the other two bodies depending on the direction of their ejection. Since much of the disk material is initially on smaller radii around the ejected body than after the encounter, the initial deviation from the hyperbolic encounter should only play a minor role, while the deviations after the closest encounter are more effective, because much of the disk material is distributed over a much larger area. Fig. 5.20 shows a snapshot of a disk after the final binary has formed and where the disk is only affected by the perturber with the closest encounter distance r_{min}. Although, at this time, after more than 20 dynamical times,

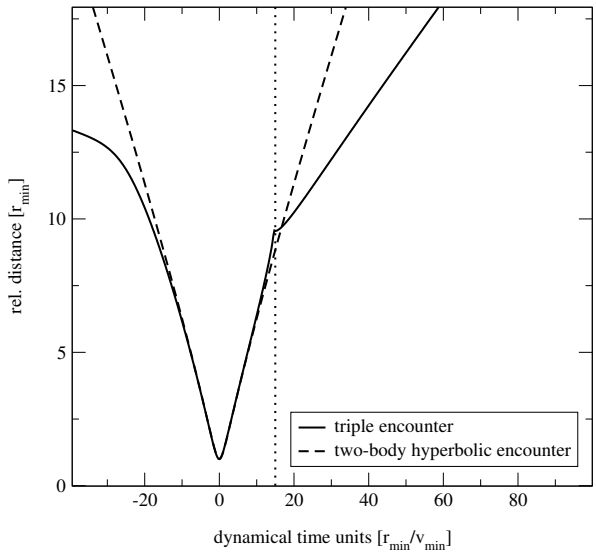

Figure 5.19: Distance of the escaping body to the body of the binary with the smallest encounter distance r_{min} over the time in units of r_{min}/v_{min} for one particular triple system, where v_{min} is the relative velocity of the two bodies at the time of r_{min} (solid line). The dashed line represents the corresponding distance if the bodies would strictly move on a hyperbolic orbit with an eccentricity of ≈ 1.4. The dotted line marks the time when the final binary forms from the triple system.

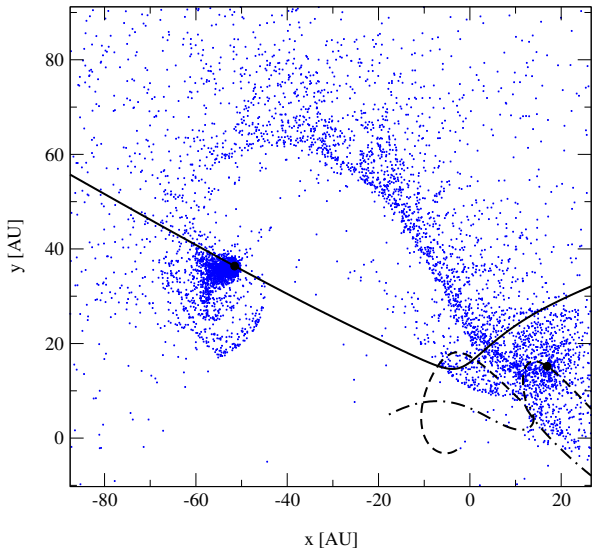

Figure 5.20: Snapshot of a disk after a triple encounter. Shown are the orbits of the escaper (solid line) and the binary (dashed and dotted dashed line) as well as the particles representing the disk material (blue dots).

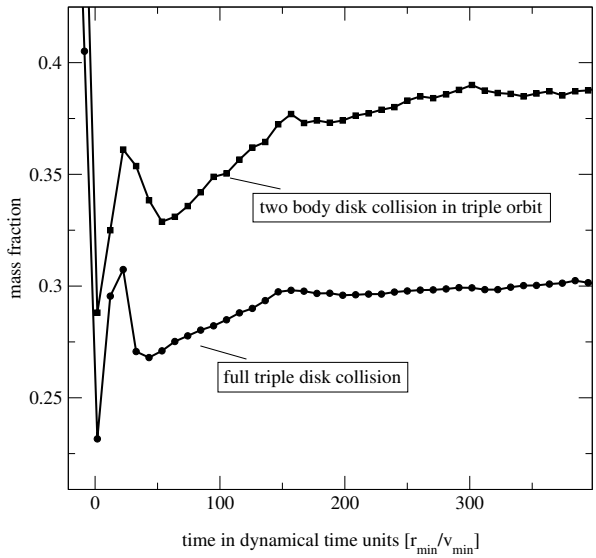

Figure 5.21: Mass of the disk around the ejected body in units of the initial disk mass over the time in dynamical time units for one particular triple system. Shown are the results for a triple collision where the disk is only affected by the escaper and its closest perturber (filled squares) and for a triple collision where the disk is affected by all three bodies (filled circles). Briefly after the time of the formation of the final binary ($\approx +15$ dynamical times) the disk mass rises significantly due to the abrupt slow down of the perturber during binary formation. Due to this deceleration of the perturber motion the disks gained about 10% of the total disk mass.

the particle states, i.e. whether they are gravitationally bound or unbound to any of the three bodies, would have been long evident in a two-body encounter (Hall et al., 1996), in a triple encounter there is a substantial amount of unbound material that gets captured later because of the perturber getting drastically slower when it forms a binary. The increased effect of the the perturber on the disk can bee seen by looking on the strong spiral arm that develops during the encounter, which, in a two-body encounter, is always pointing away from the perturber. In this figure, however, it is bent towards the binary because of the much lower velocity of the perturber after binary formation relative to the escaping body, making it possible that this otherwise unbound material gets captured by the escaper or by the perturber. Here we want to remind the reader that the effect is solely because of the deceleration of the closest perturber and not because of the mass of the third body, which the disk is not affected by in this particular simulation. The re-capture of disk material can also be seen in Fig. 5.21 where we plotted the change of mass of the disk around the ejected body. Here it can be clearly seen that first, the time required for the particle states to settle is much longer than in the two-body case, and, second, that just after the encounter and after the formation of a binary, much of the disk material lost is re-captured by the ejected body. From this figure it is also evident that the change of disk mass in an orbit of a triple system is no longer a simple function over time and a substantial amount of disk material changes its gravitational state more than once. Without the rather abrupt deceleration the disks would have masses very close to the corresponding minimum shown in Fig. 5.21. Therefore, the loss caused by the

presence of the third body is in that case compensated by approximately 10% of the initial disk mass, leading to the mass expected for only two masses in a nearly-parabolic two-body encounter.

In contrast to the behavior for the disk masses for lower r_1/r_2, the case $r_1/r_2 = 0.2$ does not converge towards the expected two-body result for the 90%-mass-radii $r_{90\%}$. Here we find that the disks after triple encounters are comparable or much larger than after slightly parabolic two-body ones. As shown in table 5.1 we also find the tendency for the post-encounter disks to become flatter with decreasing r_1/r_2 in the value of $r_{90\%}$. The dependence on r_1/r_2 is nearly the same as for the slope of $\tau_1(r_{min})$, i.e., only a weak increase for $r_1/r_2 \geq 0.5$ and a much stronger one for values below. As a consequence of the high mass concentration in the inner disk regions for $r_1/r_2 \geq 0.5$, the 90%-mass-radius has rather low values. However, compared to the results of Hall (1997), where we have $r_{90\%} = 0.5 r_{min}$, our values are not much different in the cases with $r_1/r_2 \geq 0.5$, although here we would expect to have a much stronger deviation. As already mentioned, for $r_1/r_2 = 0.2$ we do not get similar 90%-mass-radii and find that it is around $1 r_{min}$, that is, twice as large as in the parabolic two-body case. Considering that for the $r_1/r_2 = 0.2$-case we have about the same disk mass as for the corresponding two-body case, we come to the conclusion that parabolic two-body collisions produce disk with a much higher mass concentration in the inner regions and, therefore, also with a significantly increased average surface density.

We believe that the generally flatter mass distribution of disks after triple encounters is presumably caused by the capture process of unbound material after the final binary has formed, as we described in the previous few paragraphs. Since it is known that the unbound material carries most of the angular momentum away from the disk (Hall et al., 1996) the re-capture process brings some of this high-angular-momentum material back to the disk which recircularizes after the collision to larger radii, producing a flatter disk profile. In our example (Fig. 5.21) one third of the final disk material was re-captured for the case where all three bodies affect the disk, and should have a larger angular momentum thus ending up at larger radii.

5.3.4 Summary of Results

In Table 5.2 we summarized all the results of our post-encounter disk in dependence of the encounter parameters r_{min} and r_1/r_2. These values are then used to construct the recircularized surface density profile of a post-encounter disk for a given set of encounter parameters by using equation 5.1 and interpolating a_1 for a given r_1/r_2 as shown in Fig. 5.13. The only free parameter that remains to be specified is Σ_0, the value of the surface density of the initial disk at a radius of r_0, which must be provided by the problem one wishes to study.

5.4 Application to Accreting Triples

5.4.1 The Model

With the post-encounter disk model, developed in the previous section, we now want to determine the absolute sizes the disk should have if Brown Dwarfs form by early ejection from

r_1/r_2	k	$a_1\,[r_{min}]$	$a_2\,[r_{min}]$	M_i	M_1	M_2	$r_{90\%}(r_{min})$
0.95	1.7 ± 0.1	0.064 ± 0.005	0.1-0.2	0.2	0.13	<0.006	0.38
0.8	1.6 ± 0.1	0.076 ± 0.006	0.1-0.2	0.2	0.17	<0.015	0.49
0.6	1.7 ± 0.1	0.084 ± 0.005	0.1-0.2	0.2	0.19	<0.02	0.52
0.5	1.7 ± 0.1	0.085 ± 0.008	0.1-0.2	0.2	0.19	<0.02	0.52
0.2	1.7 ± 0.2	0.16 ± 0.03	0.2	0.2	0.37	0.16	1.0

Table 5.2: Summary of all numerical results for the half-width-values a_1, a_2, the constant k, the relative mass fractions $M_{i,1,2}$ with respect to the mass of a disk with $\Sigma \propto \frac{1}{r}$ and radius r_{min}, and the 90%-mass-radii $r_{90\%}$ for our disk models with different values of r_1/r_2. M_i is the mass contained in the inner region below $0.2r_{min}$ and $M_{1,2}$ are the masses in the outer two regions.

a molecular cloud core, using our simulations described in Chapter 4. In these simulations we assumed that a flattened cloud is collapsing and the central region accretes mass at a constant rate of $\dot{M}_{infall} \sim 6 \times 10^{-6}(T/10\mathrm{K})^{\frac{3}{2}}\mathrm{M}_{\odot}\mathrm{yr}^{-1}$. The central part of the cloud is then further assumed to fragment into 3 fragments and the infalling mass is equally distributed among them. Due to the fact that these fragments form in compact non-hierarchical configurations, these triple systems decay after some time, ejecting a single body and a binary system into opposite directions. Once outside of the cloud the fragments stop accreting and if that happens early enough a Brown Dwarf has formed. In our model we further accounted for the momentum the accreted gas carries onto the bodies and found that the amount of momentum transfered influences the properties of the resulting single and binary Brown Dwarfs significantly. We also found that, if the accreted gas is at rest with respect to the reference frame, i.e. it does not carry any additional momentum onto the bodies, the resulting semi-major axis distribution of the binary Brown Dwarfs matches the observed, volume-limited sample of Bouy et al. (2003). It is, therefore, invitingly to see whether it is possible to form these very compact binaries while the ejected single objects possess disks with a life-time comparable to the one of TT stars or if the existence of compact Brown Dwarf binaries contradicts the existence of long lived disks around the corresponding single escaper in the ejection scenario. Thus, our investigation provides a way to relate binary properties to disk properties and this relation can then be tested observationally.

In order to apply our scale-free results of disk collisions in triple systems to this particular model, we re-run these simulations and determined r_{min} and r_1/r_2. However, we also have to check if the encounter parameter for close triple approaches in accreting systems are comparable to the encounter parameter in non-accreting systems. Although the amount of mass that these system accrete during one crossing time is only 6% and one should, therefore, expect the system to contract adiabatically, it is not clear if the encounter parameter relative to the total system size are adiabatic invariants. Even if this might be the case, we still have to show whether the code we are using reproduces the encounter parameter shown in Fig. 5.5 and 5.6, because in this code we increased the masses stepwise, which might influence the dynamics at close collisions. Fig. 5.22 shows the distribution of r_1/r_2 for accreting and non-accreting triple systems and in Fig. 5.23 we plotted r_{min}, in units of the mean harmonic size d at the

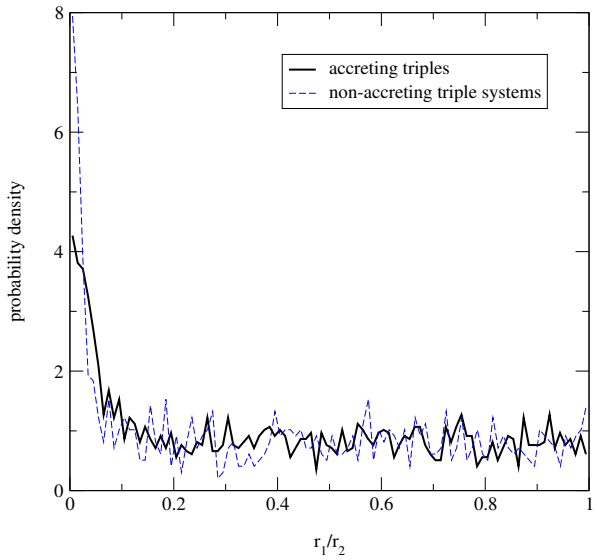

Figure 5.22: Distribution of the ratio of the closest two-body encounter distances r_1/r_2 for accreting triple systems accreting gas at rest (solid line) and for non-accreting triple systems (dashed line).

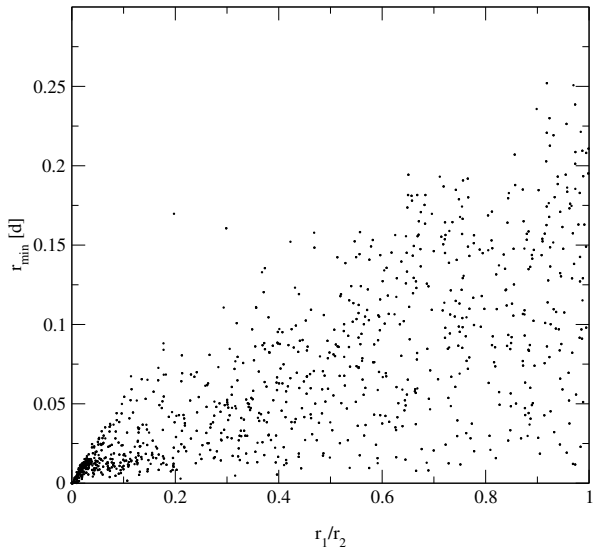

Figure 5.23: Minimum distance r_{min} in units of the mean harmonic distance (virial size) at the time of decay over the ratio r_1/r_2 for accreting triple systems accreting gas at rest.

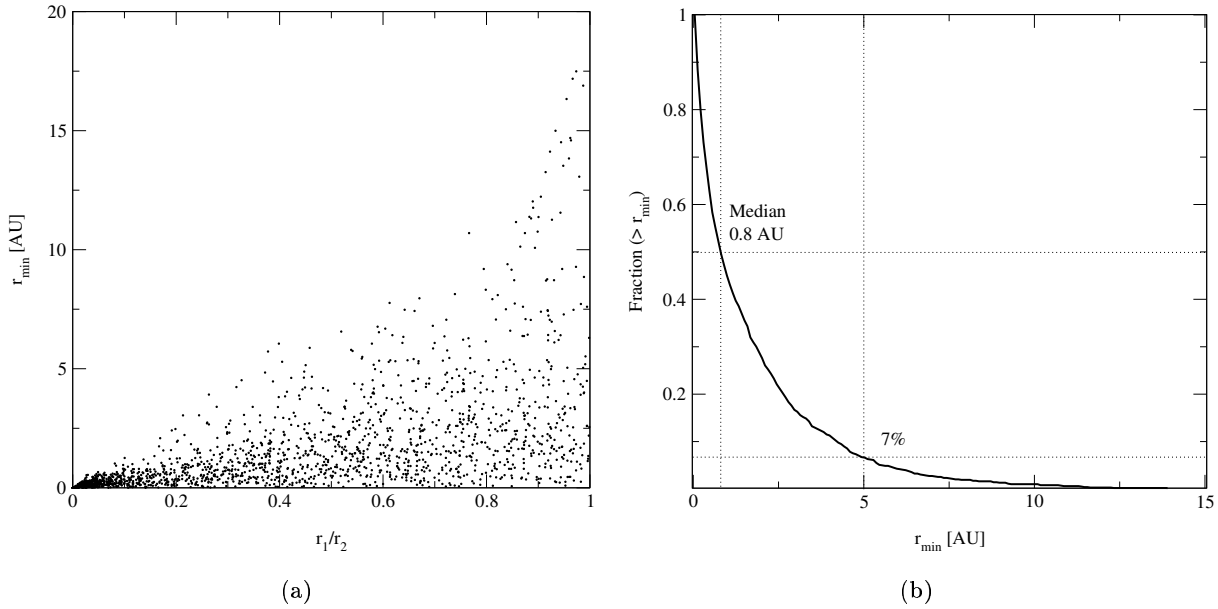

Figure 5.24: Absolute values of the encounter parameter r_{min} over r_1/r_2 for accreting triple systems accreting gas at rest (a) and the fraction of encounter that have larger r_{min} than a given value (b).

time of decay[4], over r_1/r_2 for accreting triple systems. As it can be seen the distribution of r_1/r_2 matches essentially the one for non-accreting systems, i.e. for $r_1/r_2 > 0.1$ the values are equally distributed and for lower r_1/r_2 they are strongly peaked. The only notable difference is that the peak for $r_1/r_2 < 0.05$ seems to be somewhat lower. This is because in accreting triple systems it becomes increasingly difficult to capture the minimum distances, as the time scales are decreasing rapidly which is especially a problem for encounter with $r_1/r_2 < 0.05$ as most of them have extremely small r_{min}. Apart from this slight difference in the distribution of r_1/r_2, the distribution of r_{min} over r_1/r_2 for accreting triple systems seems to be indifferent from the corresponding one of non-accreting systems. It seems therefore justified to apply our scale-free results of disk collisions in non-accreting triple systems to these accreting triple systems.

To get a first impression of the absolute sizes of the post-encounter disks we can expect in our sample of accreting triple systems we plotted r_{min} in AU over r_1/r_2 in Fig. 5.24 . As it can bee seen the majority of the encounter distances are extremely small and only a comparatively low fraction, approximately 7%, has $r_{min} > 5$AU . Making use of our previous result that the 90%-radii are mostly $0.5 r_{min}$, we, expect our disks also to be rather small with $r_{90\%} < 0.25$. Here we have to note, however, that for small r_1/r_2 these radii are becoming larger relative to r_{min}, as we found from section 5.3.3, which will lead to larger $r_{90\%}$. This effect will be considered in section 5.25.

[4]For non-accreting triple systems d is constant throughout the calculation but for accreting triples d is a function of time, so we take d at the time of the triple encounter.

Compared to the distribution of r_{min} relative to the size d of the triple system we find that the distribution of the absolute values of r_{min} differs significantly. This is because the mean harmonic size d depends on time in multiple systems with accretion, and the encounter distance scales with d. From Fig. 5.24 it can be seen that, first, r_{min} is no longer equally distributed between some maximum value and zero but tends on average to lower values, and, second, there seems to be a peak for encounters with $r_1/r_2 > 0.8$, while for $r_1/r_2 < 0.2$ the maximum value of r_{min} is generally lower than one would expect from the continuation of the corresponding values above 0.2. The much lower average value of r_{min} with respect to its maximum value for a given r_1/r_2 can be explained if one considers that the resulting distribution is the superposition of the distributions obtained from the scale-free one, as sown in Fig. 5.23, and scaled with different values of d reflecting the total energy distribution of our sample. Since the total energy depends on the fragment masses as $E \propto (M(t)/M_0)^5$ and these masses are nearly equally distributed between $0.05\mathrm{M}_\odot$ and 0.07M in our sample, it becomes clear that the distribution of the mean harmonic size d, which is indirectly proportional to the total energy, is strongly peaked towards small values. This has the consequence that there are more superimposed distributions with a lower d than with a larger one, and it is therefore that lower r_{min} are more frequent than larger ones for a given r_1/r_2.

The differences at both ends of the distribution shown in Fig. 5.24 compared to the scale-free one in Fig. 5.23 is an effect of the dependence of the decay probability on r_1/r_2. Anosova & Orlov (1992) found that the decay probability increases with decreasing deflection angle, defined as the angle between the direction of motion of the escaper before and after the encounter. This angle becomes, on average, larger for smaller values of r_1/r_2, as for small values the escaper is strongly deflected by the single body with the closest encounter distance, while the deflection by the third body that works in the opposite direction is very limited. For accreting triple systems, where the mass depends on time, this means that the average system mass becomes larger for smaller r_1/r_2. Since the size d depends strongly on the fragment masses, as the total energy is proportional to $\left(\frac{M}{M_0}\right)^5$, it becomes clear that the average value of r_{min} decreases much more for decreasing r_1/r_2 than for non-accreting systems, which is most visible at the extreme values of r_1/r_2.

In order to apply our results of disk collisions from section 5.3 to accreting triple systems in a collapsing molecular cloud core we must assume that the disk has a mass lower than 0.1 times the mass of the ejected Brown Dwarf. Although, from simulations of collapsing cloud cores it has been found that disks at such an early stage of formation should be more massive (Yorke & Bodenheimer, 1999; Lin & Pringle, 1990), in our case the disks should have already lost much of their material because of previous interactions in the triple system. In section 5.3.1 we assumed that the disk has an initial size of $\frac{1}{3}d$, with d being the mean harmonic size of the triple system at the time of decay. If we take the largest value for d from our sample of accreting triple systems at the time of decay with $d = 83.4$AUand fragment mass of $M = 0.048$, we find that the surface density at 1AUfor our $\Sigma \propto \frac{1}{r}$-disk profile must be less than $240\mathrm{g} \cdot \mathrm{cm}^{-2}$ in order to for the disk mass to be less than $0.1M$. This value seems to be roughly compatible with simulations of disks forming in collapsing molecular cloud cores (e.g. Laughlin & Bodenheimer (1994), Yorke et al. (1993)) and might even be an underestimate[5].

[5]In these simulations the disk was only resolved down to a radius of ≈ 6AU, so the value at 1AU depends on how one extrapolates.

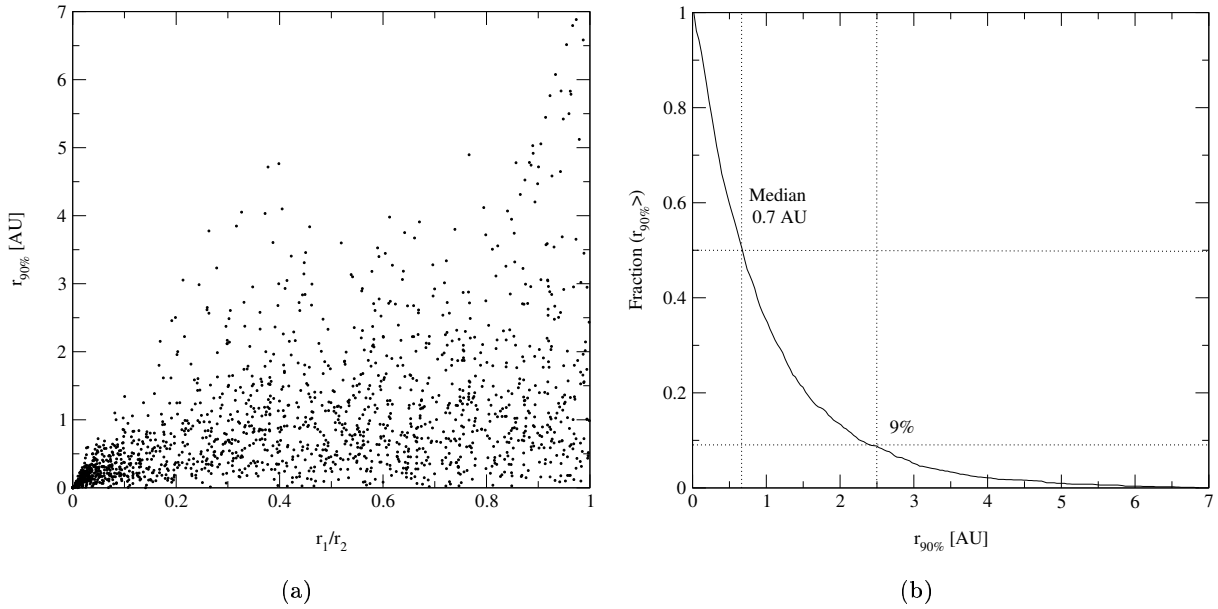

Figure 5.25: Disk sizes $r_{90\%}$, defined as the radius within which 90% of the disk mass is contained. Shown are the values of $r_{90\%}$ over r_1/r_2(a) and the fraction of encounter that produced a disk that has a larger size than a given $r_{90\%}$(b).

Therefore, our assumption of a low-mass disk before the last encounter seems to be justified and for simplicity we will set $\Sigma_0 = 240\text{g} \cdot \text{cm}^{-2}$ for all our disks. As most of the other accreting triple systems have a much smaller mean harmonic distance at the time of decay, we could, in principle, also allow for somewhat more massive disks similar to those in Lin & Pringle (1990), without that self-gravity in disks will influence our statistical results significantly. We, however, decided to take a low value for all disks in order to get a lower limit on the resulting post-encounter disks.

At this point we have fixed all parameters necessary to determine the physical sizes as well as the absolute masses of the post-encounter disks we will present in the next sections.

5.4.2 Post-Encounter Disk Sizes

Fig. 5.25 shows the distribution of $r_{90\%}$ over r_1/r_2 as well as the fraction of encounters that produced a disk that has a larger value than a given $r_{90\%}$. Compared to the distribution of r_{min} over r_1/r_2 in Fig. 5.24 there is no essential difference for $r_1/r_2 > 0.8$ apart from the fact that $r_{90\%}$ is only half of the value of r_{min}. For lower r_1/r_2, however, the dependence of the disk profile on r_1/r_2 becomes significant, as now the disks are getting flatter, resulting in larger values of $r_{90\%}$ with respect to r_{min}. As one can see, this effect causes the maximum value of $r_{90\%}$ for a given r_1/r_2 to remain roughly constant at 4AU while r_{min} is strongly decreasing in Fig. 5.24. For $r_1/r_2 < 0.4$ the increasingly flatter disk profile can no longer counterbalance the quickly decreasing r_{min} and the absolute value of $r_{90\%}$ decreases again.

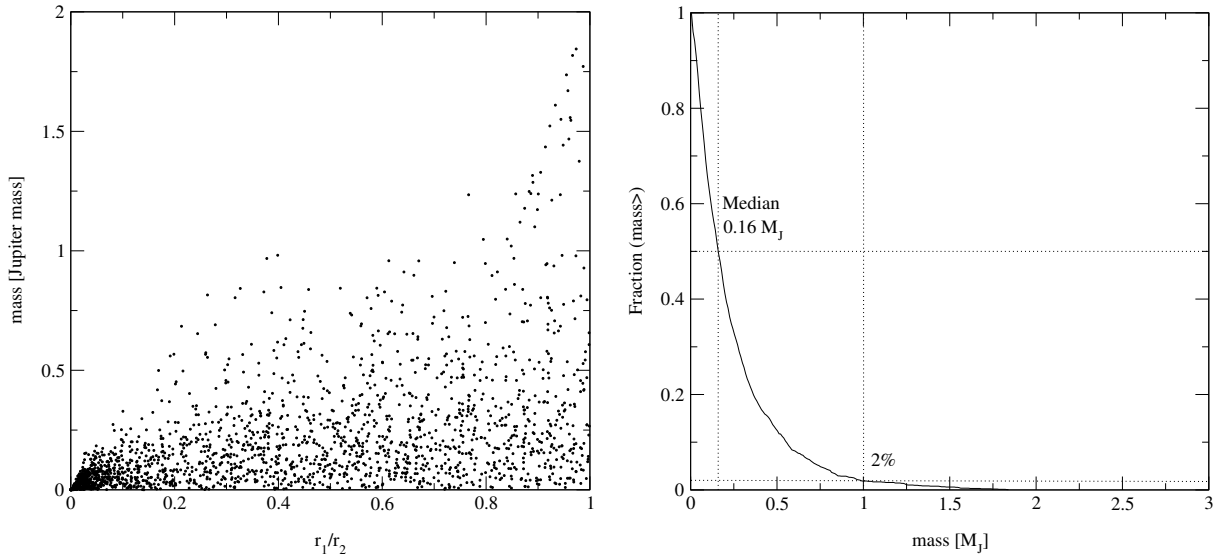

(a) (b)

Figure 5.26: Disk mass in units of M_J, the mass of Jupiter, over r_1/r_2(a) and the fraction of encounters that produced a disk with a larger mass than a given value (b). Here it is assumed that the initial surface density profile, $\Sigma \propto \frac{1}{r}$, has a value of $\Sigma_0 = 240\text{g} \cdot \text{cm}^{-2}$ at a radius of $r = 1\text{AU}$.

The overall effect of the increasingly flatter disk profile for lower r_1/r_2 on the distribution of the absolute values of $r_{90\%}$ is, however, limited compared to the influence of r_{min}. This can be easily seen, if one compares the distribution of r_{min} in Fig. 5.24(b) with the distribution of $r_{90\%}$ in Fig. 5.25(b). Assuming that $r_{90\%} \approx 0.5 r_{min}$, the resulting distribution of $r_{90\%}$ is only decreased by a few percent, as one can see by comparing the fraction of systems at $r_{min} = 5\text{AU}$ and at $r_{90\%} = 2.5\text{AU}$. This changes, however, for the closer encounter, as most of them have $r_1/r_2 < 0.5$ and, therefore, flatter disk profiles. As a consequence the median of these two distributions seems nearly identical.

In general we find that for the close encounter we investigate here, the majority of the resulting recircularized post-encounter disks have sizes of only a few AU.

5.4.3 Absolute Disk Masses

In Fig. the distribution of the post-encounter disk masses are shown. The distribution of the disk masses over r_1/r_2 shows the same features as the one for $r_{90\%}$ in Fig. 5.25 . This is because, as we already found from the discussion of the relative disk masses in section 5.3.3, a flatter disk profile corresponds to a higher mass for the same initial surface density distribution.

As already noted in section 5.4.1, in order to apply the scale free results from our disk-collision calculations we must ensure that the initial disk is of low mass with $M_{disk} < 0.1M$, which

is why we have chosen $\Sigma_0 = 240\mathrm{g} \cdot \mathrm{cm}^{-2}$. As a result, the post-encounter disk masses are, as the disk sizes, generally very low, with masses barely exceeding $1\mathrm{M_J}$. For our sample we find only 2% of the systems with masses larger than $1\mathrm{M_J}$ and half of the disks have masses larger than $0.16\mathrm{M_J}$. These masses fall in the lower range of the expected disk masses derived from millimeter observations of Klein et al. (2003), who found masses ranging from 0.4 to $2.4\mathrm{M_J}$ for the disk around CFHT-BD-Tau 4 in the Taurus star-forming region. At a first glance our results seem, therefore, to be consistent with observations. However, the age of the object should be around 1Myr, the approximate age of the Taurus cluster, and at this time the majority of our disks should have already accreted a substantial amount of material, as our fragments have an age less than $1 \cdot 10^5\mathrm{yr}$. Therefore, only a few percent of our disks should have a mass larger than $0.4\mathrm{M_J}$, but this depends strongly on the amount of viscosity in the disk, which is even for the well studied TTauri disks not very well constrained.

Concerning the expected disk life-time it appears that we could still cover the whole range of disk life-times as found for disks around TTauri stars, if one considers that Brown Dwarfs disks have rather low accretion rates, typically of the order of $\approx 10^{-10}\mathrm{M_\odot} \cdot \mathrm{yr}^{-1}$ (Natta et al., 2004). However, here one should also note that the accretion rate is decreasing with time and the observed accretion rates are around Brown Dwarfs with an age of usually more than $5 \cdot 10^5\mathrm{yr}$. Therefore, the accretion rate was initially much higher and taking an average value is not straight forward without some hydrodynamical modeling of the disk, which we will carry out in the next section.

5.4.4 Evolution of Ejected Disks

So far we determined the sizes and estimated the masses of disks around Brown Dwarfs just after they have left the cloud core. For our model this is approximately at a time when the ejected Brown Dwarfs have an age of $3-6 \cdot 10^4\mathrm{yr}$. As we noted previously, the observed Brown Dwarfs with disks have ages of usually more than $5 \cdot 10^5\mathrm{yr}$ (Muzerolle et al., 2003). In order to bridge this gap from our post-encounter disks to disks of that age we have to take into account their further, viscous evolution.

At the beginning of our disk collision simulations we assumed a disk that forms in a collapsing cloud core and should, therefore, possess a rather flat surface density profile, with $\Sigma \propto \frac{1}{r}$. Once the Brown Dwarf with its disk is ejected out of the cloud core, the disk profile will change as there is now no longer a strong infall of material that affects the evolution and structure of the disk. The disk evolves then rather isolated, only subject to the temperature of the ambient medium outside of the cloud core and to its own viscously generated heating. For simplicity we neglect the stellar irradiation from the central object, noting that it presumably is only an effective heating mechanism in the upper layers of the disk (see, e.g., D'Alessio et al. 1998), whose effects however are reduced by small disk scale heights (D'Angelo et al., 2003), which is the case for our disks.

Because the heating due to viscosity diminishes for larger disk radii, the temperature of the outer disk will be given by the temperature of the ambient medium outside of the cloud core. This temperature varies between different star-forming regions, ranging from $\approx 20\mathrm{K}$ for the rather cool Taurus regions up to 100K and more for the hotter Orion regions (Bell et al., 1997).

As we will find later, our rather small disks will expand significantly after about $2.5 \cdot 10^5$yr even if we initially assume very low temperatures throughout the disk. Therefore, most of the disk material is then at radii where it will evolve with the constant temperature of the ambient medium. In order to make predictions about the outer disk profile at a typical age of a young Brown Dwarf, we, therefore, can evolve the whole disk at this constant temperature.

However, we cannot use this approximation in order to determine the life-time of our post-encounter disks. From an observational point of view the life-time of a disk is determined with the time when the accretion rate drops below a value of $\approx 10^{-12}\mathrm{M}_\odot \cdot \mathrm{yr}^{-1}$, which is currently the detection limit for detecting H_α-emission (Muzerolle et al., 2003). As we will see in section 5.4.4.1, the inner disk inside $\approx$ 1AU becomes increasingly hotter, which increases the viscosity and, therefore, the accretion rate. Since most of our disks are initially inside that radius, their mass loss and life-times are strongly influenced by these much hotter conditions. Because taking the detailed temperature structure into account during the integration of the disk evolution is computationally rather expensive, we cannot calculate all our post-encounter disks with realistic temperature profiles. For this reason, we calculate only one such case and compare it to a calculation with the same initial conditions but at a constant temperature throughout the disk. We then increase this constant temperature until we match the mass loss of the more realistic calculation. As the temperature in the more realistic case is decreasing with time, and we match only the first 10^4yr with the approximate model resulting in a rather high value for the constant temperature, the mass loss will be generally overestimated at later times causing the accretion rate to drop much faster. Therefore, our statistical result on the life-times of our post-encounter disk represent lower limits.

We evolve our post-encounter surface density profile according to the evolution equation of a thin disk, given in Lynden-Bell & Pringle (1974)

$$\frac{\partial \Sigma}{\partial t} = \frac{3}{r}\frac{\partial}{\partial r}\left[\sqrt{r}\frac{\partial}{\partial r}\left(\nu\Sigma\sqrt{r}\right)\right]. \tag{5.4}$$

with ν being the kinematic viscosity. For ν we take the α-model of Shakura & Sunyaev (1973), giving

$$\nu = \alpha c_s H$$

where c_s is the speed of sound, H the pressure scale height and α a dimension-less parameter. The value of α is not very well constrained and typical values range from $1 \cdot 10^{-4}$ to $1 \cdot 10^{-1}$. Laughlin & Bodenheimer (1994) find in their simulations of the viscous evolution of disks in collapsing molecular cloud cores, that the surface density profile of their three-dimensional disk calculations can be best reproduced by a thin-disk model with an effective $\alpha = 0.03$. This value takes into account that the disk in a collapsing molecular cloud core is rather massive and, therefore, gravitational torques from spiral arms that develop as the disk becomes unstable, lead to an enhanced redistribution of angular momentum. However, for our post-encounter disks we find a very low mass compared to their central object, making our disks non-self-gravitating and, therefore, allows us to neglect the influence of spiral arms. This should in turn make the value of α much lower. Arguments based on the duration of FU Orionis outbursts, provided they are due to disk instability, also suggest a lower value for T Tauri disks (Bell & Lin, 1994), with α between $10^{-4}$and 10^{-3}. We therefore decided to take the upper limit and set $\alpha = 1 \cdot 10^{-3}$ for our calculations, which is also a value found for disks, where the

effective viscosity is caused by magneto rotational instability (MRI) (Abramowicz et al., 1996; Brandenburg et al., 1996; Balbus & Hawley, 1991).

For the vertical structure relative to the disk mid-plane the disk can be assumed to be in local, hydrostatic equilibrium leading to

$$H \approx \frac{c_s}{\Omega}$$

(Pringle, 1981), where Ω is the angular frequency and for a Keplerian, or low-mass, disk given by

$$\Omega = \sqrt{\frac{GM}{r^3}}$$

with G the constant of gravity and M the mass of the central object. Assuming an ideal gas, the isothermal sound speed is given by

$$c_s = \sqrt{\frac{k_B}{\mu m_p} \cdot T(r)}$$

where T is the temperature, μ the mean molecular weight, m_p the proton mass and $k_B$the Boltzmann constant.

As we mentioned previously, the evolution of the outer disk profile should happen at the constant temperature of the ambient medium of the molecular cloud. This allows us to write equation 5.4 in a non-dimensional form, where Σ, the time t and the radius r are given as follows:

$$\begin{aligned} \Sigma &= \Sigma' \cdot \frac{\Sigma_0 k\, r_0}{r_{min}} \\ t &= t' \cdot \frac{\sqrt{r_{min} \cdot GM}}{\alpha \cdot c_s^2}. \\ r &= r' \cdot r_{min} \end{aligned} \tag{5.5}$$

The dashed variables are the non-dimensional quantities and Σ is initially given by the model surface density profile obtained from our disk collision results:

$$\Sigma = \frac{\Sigma_0 \cdot k \cdot r_0}{r_{min}} \begin{cases} \frac{1}{r'} & ; r' \leq 0.2 \\ \frac{1}{0.2} \cdot \tilde{a} \cdot \exp\left(\log(1/2) \cdot \frac{r'}{a_1}\right) & ; 0.2 < r' < 0.7 \\ \frac{1}{0.2} \cdot \tilde{a} \cdot \tilde{b} \cdot \exp\left(\log(1/2) \cdot \frac{r'}{a_2}\right) & ; r' \geq 0.7 \end{cases}$$

The dimensionless form of equation 5.4 is then integrated for 60 different initial profiles varying in the non-dimensional half-width value a_1 of the exponential part of the initial disk profile located between $0.2 r_{min}$ and $0.7 r_{min}$, while the non-dimensional half-width value a_2 of the outer part is always $a_2 = 0.2$. For the non-dimensional calculations we integrate equation 5.4 on a radial, logarithmically spaced Eulerian grid with 1000 grid points where the inner and outer boundaries are at $r'_{in} = 1 \cdot 10^{-3}$ and $r'_{out} = 1 \cdot 10^{2}$ respectively. This allows us to resolve the rather small initial post-encounter disks, while still allowing to investigate the outer disk profile at later times, when the disks are much more extended, without being

strongly influenced by the outer boundary. At both boundaries we set $\Sigma = 0$ which allows the disk material to move freely out of our computational domain, corresponding to a 'no-torque' boundary condition (Lynden-Bell & Pringle, 1974). We do not consider the influence of an ordered magnetic field of the central object onto the disk via the disk-locking mechanism (e.g. Koenigl, 1991) which could lead to significant disk braking, shortening the disk life-time as expected for ejected T Tauri stars (Armitage & Clarke, 1997). We neglect it because from observations of the rotational evolution of Brown Dwarfs it is still unclear if the magnetic field around a Brown Dwarf will couple efficiently to the disk to cause significant braking (Eislöffel & Scholz, 2005).

In our test calculation where the detailed temperature structure is taken into account, we integrated the dimensional form of equation 5.4 on an Eulerian grid with 100 logarithmically spaced grid points and boundaries at $r_{in} = 0.1$AU and $r_{out} = 100$AU and the same 'no torque' boundary condition we used for the non-dimensional calculation. The radial temperature structure is determined at each integration step by requiring, that the locally generated viscous heating is balanced by the radiative losses, which is explained in greater detail in section 5.4.4.1.

Equation 5.4 is integrated using the "method of lines" described in Skeel & Berzins (1990). In this method the space derivatives are replaced by a second-order accurate spatial discretization, converting the partial differential equation into a system of first order ordinary differential equations in time. As this system of differential equations tend to be rather stiff, an implicit, variable-order multi-step scheme developed by Shampine & Reichelt (1997) is used to advance it in time.

5.4.4.1 Temperature Structure of Brown Dwarf Disks

In order to integrate equation 5.4, the kinematic viscosity ν needs to be determined at each time-step. As ν depends on the mid-plane temperature we need to find a way to obtain T. For a thin disk this temperature can be obtained by using that the thermal energy is only transported in vertical direction (Pringle, 1981). Therefore, the temperature only depends on the local energy balance at a given radius r. This balance requires that the viscously generated heat equals the radiative losses. Here we neglect the energy loss by convection as it is not expected to be a major energy carrier (Bell et al., 1997). Since in a thin disk with low α the disk maintains both thermal and hydrostatic equilibrium on a viscous time scale, the internally generated viscous heat is that of a steady disk and further assuming a Keplerian disk with 'central couple' (Lynden-Bell & Pringle, 1974) leads to

$$\sigma_R T_{eff}^4 \equiv \frac{3\dot{M}GM}{8\pi \cdot r^3}\left(1 - \sqrt{\frac{R_*}{r}}\right) \tag{5.6}$$

(Pringle, 1981) where we assigned the generated heat an effective Temperature T_{eff} at which a black body would radiate the same amount of energy[6]. Here σ_R is the Stefan-Boltzmann

[6]The radiation emerging from the disk surface can be described as black body radiation, as the disk is optically thick (Pringle, 1981).

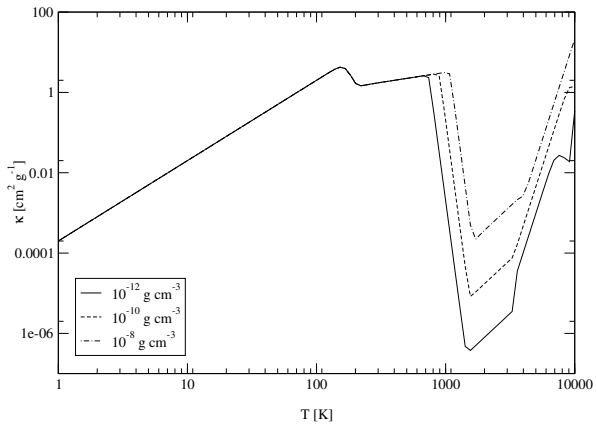

Figure 5.27: Rosseland mean opacity κ over temperature for three different densities ρ (taken from Bell & Lin (1994)).

constant, $\dot{M}(t,r)$ the accretion rate at a time t and disk radius r, and R_* is the (sub)stellar radius. For a steady disk we can further exploit that

$$\nu\Sigma = \frac{\dot{M}}{3\pi}\left(1-\sqrt{\frac{R_*}{r}}\right) \tag{5.7}$$

(Pringle, 1981) which we can substitute into equation 5.6 to give

$$T_{eff} = \left(\frac{9}{8}\cdot\frac{GM}{r^3}\cdot\frac{\Sigma\nu}{\sigma_R}\right)^{\frac{1}{4}}. \tag{5.8}$$

In order to obtain the radiative losses one has to account for the absorption of the gas which is dominated by the dust. The effect of absorption on the emitted radiation that emerges from the mid-plane and travels vertically through the disk is characterized by the optical thickness τ, which is for a thin disk approximately given by

$$\tau = \kappa(\rho,T)\rho H$$

(Pringle, 1981). Here ρ and T are the mid-plane density and mid-plane temperature respectively, and κ the frequency averaged Rosseland mean opacity. For κ we use the formulas derived by Bell & Lin (1994) that account for contributions from dust grains, molecules, atoms, and ions in eight temperature regimes. In Fig. 5.27 the temperature dependence of κ is shown for different values of the mid plane density ρ. As it can be easily seen, κ is for high temperatures above 100K a rather complicated function which is why it needs some numerical effort to obtain T as a function of κ and ρ when calculating the temperature profile. We should note here that these opacities were chosen for simplicity and more sophisticated models are available in Semenov et al. (2003) and include the improved grain opacity tables of Henning & Stognienko (1996).

As our disk variables are vertically integrated, the mid-plane density ρ is not readily available but can be approximately obtained by

$$\rho = \frac{\Sigma}{H}$$

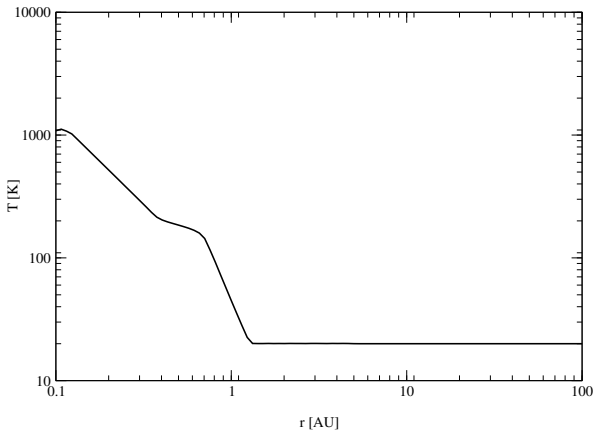

Figure 5.28: Temperature structure of a $\Sigma \propto \frac{1}{r}$-profile with a surface density of $\Sigma_1 = \Sigma_0 \cdot 1.7$at $r = 1$AU, $\Sigma_0 = 240\,\mathrm{g \cdot cm^{-2}}$ and a central object with mass $M = 0.08\,\mathrm{M_\odot}$. The temperature of the ambient interstellar cloud medium is $T_{amb} = 20$K.

(Pringle, 1981). To relate the viscously generated heat to the mid-plane temperature we use the theory of Hubeny (1990) who found

$$\sigma_R T_{eff}^4 = 2\sigma_R T^4 \left(\frac{3\tau}{8} + \frac{\sqrt{3}}{4} + \frac{\epsilon_H}{4\tau} \right)^{-1} \tag{5.9}$$

where $\epsilon_H$represents roughly the ratio of the total extinction, i.e. absorption plus scattering, and absorption (D'Angelo et al., 2003). For simplicity we set $\epsilon_H = 1$, therefore, neglecting the influence of radiation that is scattered while it emerges from the mid-plane of the disk.

We can now equate the viscous heating and the radiative cooling terms by inserting T_{eff} from equation 5.8 into equation 5.9 and solve for the mid-plane temperature. As we already mentioned, κ is a rather complicated function and cannot be easily inverted, which is why we have to solve equation 5.9 numerically. The method we are using is described in Forsythe et al. (1977) and is a combination of bisection, secant, and inverse quadratic interpolation methods.

In Fig. 5.28 we show the radial temperature profile of a disk with $\Sigma \propto \frac{1}{r}$ and absolute surface densities matching the power-law part in our post-encounter disk profile, where we assumed an ambient medium temperature of 20K. Here it can be seen that outside a radius of ≈ 1AU the disk temperature is set by T_{amb}, the temperature of the ambient medium, while for smaller radii the disk temperature raises quickly and reaches values as high as 1000K. Since ν, the kinematic viscosity, is directly proportional to T this means that the accretion rate at the inner disk is much higher than in the outer parts, causing the surface density in the inner disk to decrease much more rapidly. Because the accretion rate depends directly on the surface density Σ (eq. 5.7), $\dot{M}$ will also become lower, which in turn causes the temperature to decrease, in our test calculation down to ≈ 800K within $1 \cdot 10^4$yr at a radius $r \approx 0.1$AU. Because of the decreasing temperature in the inner disk, the region of the disk where the temperature is set by T_{amb} will extend down to less than 1AU. In addition, as we already mentioned in the last

section, viscous evolution will also transport disk material to larger radii where the viscously generated heat is low, thus the temperature is set by the ambient medium. Therefore, at later times most of the disk will finally evolve at the constant temperature T_{amb} and allows us to approximately investigate the outer disk profile as well as the size of the disk by integrating equation 5.4 at a constant $T = T_{amb}$. However, as in our test case we were only able to evolve the disk until a time of $1 \cdot 10^4$yr, we cannot determine to what extend this simplification is justified, but it seems to us a reasonable one.

As we noted earlier, with this approximation we cannot determine the life-time of the disk, as the accretion rate is dominated by the much hotter conditions in the inner disk and most of the disk material is for the majority of our disks inside the hot region below 1AU. From Fig. 5.28 it becomes clear that, in order to approximate these conditions with a constant temperature, it cannot be much larger than 1000K. Indeed, comparing the mass loss in our test calculation, where the detailed temperature structure is accounted for, with the corresponding one with constant temperature leads to the same mass loss within the first $1 \cdot 10^4$yr provided the constant temperature is set to $T = 1000$K. Because we expect the temperature in the inner disk to decrease with time, for the reasons we mentioned before, the case with constant $T = 1000$K will definitely over estimate the mass loss at later times, causing the accretion rate to drop much faster, which provides, therefore, only a lower limit on the life-time of the disk.

In order to cover the extreme cases we work with two constant-temperature approximations, one for predicting the outer disk profiles and sizes at the low ambient temperature, and the other one for predicting a lower limit on the expected life-times of Brown Dwarf disks at the much hotter $T = 1000$K.

5.4.4.2 Disk Sizes

As we have seen in section 5.4.2, the sizes of the recircularized disks are mainly of the order of a few AU just after the triple encounter. In this section we want to illustrate how quickly the disks re-expand and how large they should be at a typical age of a young Brown Dwarf. For this purpose we integrate equation 5.4 in its non-dimensional form for many profiles, differing in the non-dimensional half-width value a_1. We then calculate Σ' at many different times t'. For a given encounter r_{min}, r_1/r_2 the corresponding value a_1 is calculated according to the linear fit as shown in 5.13. We then choose the results of the integration run with the closest matching initial profile. After determining the viscous time-scale from equation 5.5, with M being the mass of our Brown Dwarf at hand, we select the resulting $\Sigma'(r', t')$ that corresponds to a physical time t we wish to obtain $r_{90\%}$ at, and determine $\Sigma(r, t)$ in order to get $r_{90\%}$. As we here neglect the hotter conditions in the inner disk, our $r_{90\%}$ are smaller and represent lower-limits on the sizes of our disks. However, we do not expect the effect to be significant for disks with $r_{90\%}$ larger than 5AU, as the hot inner region is for those disks comparatively small.

Fig. 5.29 shows for two different ambient temperatures, the fraction of our Brown Dwarf disks that have a 90%-radius larger than a given $r_{90\%}$ at 0.25Myr, 0.5Myr and 1Myr. As it can bee seen, for low ambient temperatures of $T_{amb} \approx 20$K, typical for low-mass star-forming regions similar to Taurus, the majority of the post-encounter disks remain compact at an age between

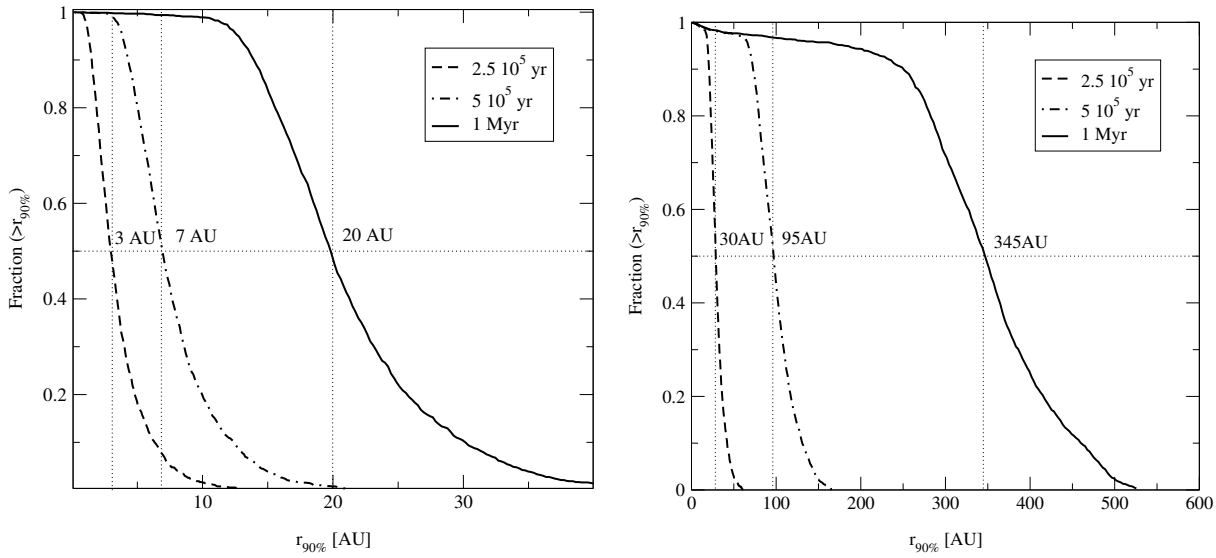

Figure 5.29: Fraction of ejected Brown Dwarf disks with 90%-mass-radii larger than a given $r_{90\%}$ at different times. Shown are disks evolving with the constant ambient temperature $T_{amb} = 20$K (a) and $T_{amb} = 100$K (b).

0.25Myr and 0.5Myr, with $r_{90\%}$ generally less than 20AU. This is, despite the fact that, compared with their initial size shown in Fig. 5.25, the disks increased their size on average by a factor of more than 4. We find, that most of our ejected disks remain significantly smaller than one would expect from ordinary T Tauri stars, with only 20% exceeding a size of 10AU at an age of 0.5Myr, which could be an important observational discriminant for the ejection scenario.

After about 1Myr, the approximate age of the Taurus star-forming region, the disks expanded further with half of them having now sizes of more than 20AU and almost all of them have $r_{90\%}$ larger than 10AU. As this already falls into the lower range of sizes expected for typical TTauri stars, it should be rather difficult to make a distinction between Brown Dwarfs formed by ejection and isolated Brown Dwarfs based on their size. Only if the disks around a Brown Dwarfs in a cool low-mass star-forming region turn out to be much more extended than 50AU at an age of $\sim$ 1Myr then one should not find many close Brown Dwarf binaries. If, however, large Brown Dwarf disks and close Brown Dwarf binaries exist in the same star-forming region then it is seems very unlikely that both formed by ejection and the ejection scenario cannot be the primary Brown Dwarf formation mechanism for that region.

While for cool low-mass star-forming regions it seems possible to distinguish between a formation by ejection and a more or less isolated one based on disk sizes, for the hotter regions similar to Orion, with $T_{amb} \sim 100$K, no such distinction can be made. For $T_{amb} = 100$K already after 0.25Myr almost all disks are larger than 20AUand after 0.5Myr almost 50% are larger than 100AU.

We therefore come to the conclusion, that only observations of disks around the youngest Brown Dwarfs in rather cool star-forming regions might be able to constrain Brown Dwarf formation scenarios. However, one should also note that in our disk collision simulations we have considered the presumably most destructive configuration, as the disk was always in the orbital plane of the triple system, thus we only considered coplanar encounter. It might be, therefore, possible that at least some of the disks are larger if the disk encounter are non-coplanar, which should be investigated in a future study.

5.4.4.3 Evolution of the Surface Density Profile

As we found from section 5.4.2, the outer disk profile of our post-encounter disks is steeply decreasing with $\Sigma \propto \exp\left(-\frac{r}{\tau}\right)$ and has rather small half-width values τ of mostly less than 1AU. As such a profile clearly deviates from the expected power-law profile of a thin, steady, viscous disk (D'Alessio et al., 1998), it would be interesting to know for how long it can in principal be observed before it reaches its equilibrium structure. From the previous section we found that, if the disk evolves in a hot star-forming environment, it expands within a short time to much larger radii. Therefore, it should reach its equilibrium structure already at an age much less than $2.5 \cdot 10^5$yr and it is, therefore, rather unlikely to observe possible signatures of an encounter in the disk profile at typical ages of observed young Brown Dwarfs. This is why we restrict ourselves to the investigation of disk profiles at rather cool ambient temperatures and choose $T_{amb} = 20$K. Here we only want to illustrate the general evolution of our post-encounter disks, looking at two examples with different initial profiles. For better comparison we choose their r_{min} values such that they have the same masses. Thus we investigate two disks with different profiles and approximately the same life-time. For the encounter parameter that produce the steeper disk profile we choose $r_{min} = 5$AUand $r_1/r_2 \approx 0.95$, resulting in a half-width value $\tau_1 = 0.064 \cdot 5\text{AU} = 0.32\text{AU}$, while for the flatter profile $r_{min} = 2.3$AU and $r_1/r_2 = 0.2$, resulting in $\tau_1 = 0.16 \cdot 2.3\text{AU} = 0.368\text{AU}$.

Fig. 5.30 to 5.32 show the evolution of the surface density for the two disks at $t = 2 \cdot 10^4$yr, $2.5 \cdot 10^5$yr and $5 \cdot 10^5$yr.

At times as early as a few 10^4yr the outermost profiles are still rather steep and can be described as a single exponential function. For the $r_1/r_2 \approx 0.95$ encounter (Fig. 5.30 left panel) one can even distinguish the two disk regions with different half-width values, but their difference is rather small and it should be extremely difficult to observe such a structure in a real disk.

From the detailed structure calculations of D'Alessio et al. (1998) we know that our profiles will eventually approach the $\Sigma \propto r^{-1.5}$-profile for constant temperature disks which is steeper than the $\Sigma \propto r^{-1}$-profile of the inner part of our initial disk profiles. As we can see from Fig. 5.31 and 5.32, after a time of more than $2.5 \cdot 10^5$yr the inner part of our disks are already close to the steeper $\Sigma \propto r^{-1.5}$-profile. This was to be expected, as that time corresponds to half the viscous time, given by $t_\nu \approx r^2/\nu$, at 1AU, indicating that at small radii the disk is already viscously more evolved. In the outer parts of the disk, on the other hand, the surface density still seems to decrease exponentially but much less steeply than initially, because the disk has expanded. Closer inspection, however, reveals that this decrease can only be poorly

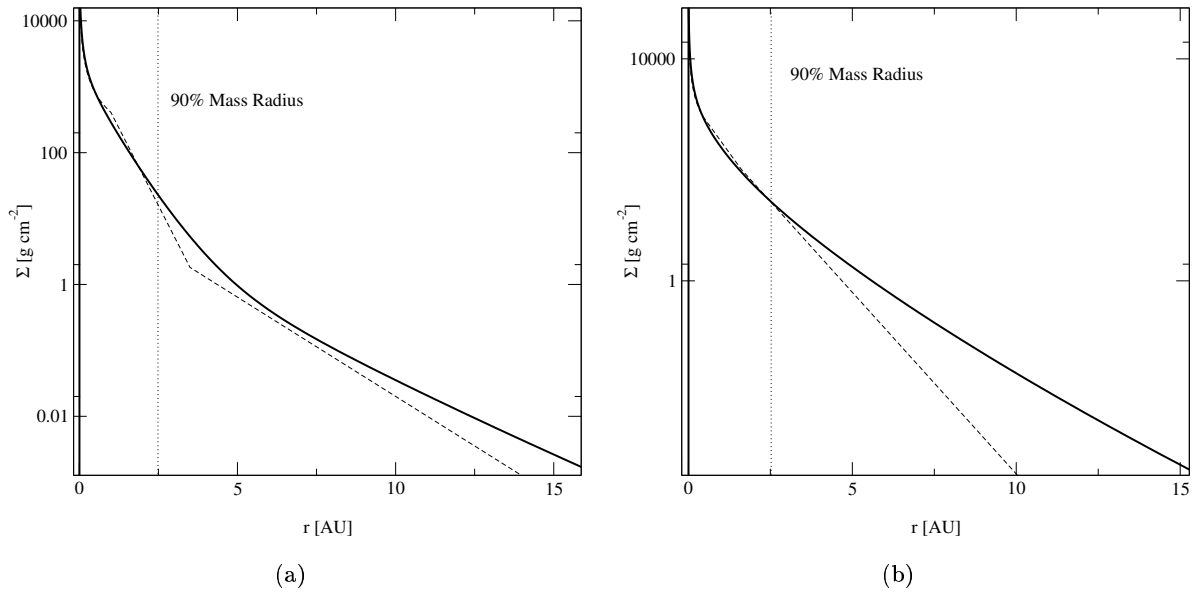

Figure 5.30: Radial Surface density profiles at a time of $\approx 2.5 \cdot 10^4$yr (solid line) together with their initial profiles (dashed line), plotted semi-logarithmically. Shown are the profiles for a disk with a steep initial profile ($a_1 = 0.064$) and $r_{min} = 5$AU (a), and a flatter profile ($a_1 = 0.16$) with $r_{min} = 2.3$AU (b). The parameters were chosen that both disks have initially the same mass. The disk are evolved at an ambient temperature of $T_{amb} = 20$K.

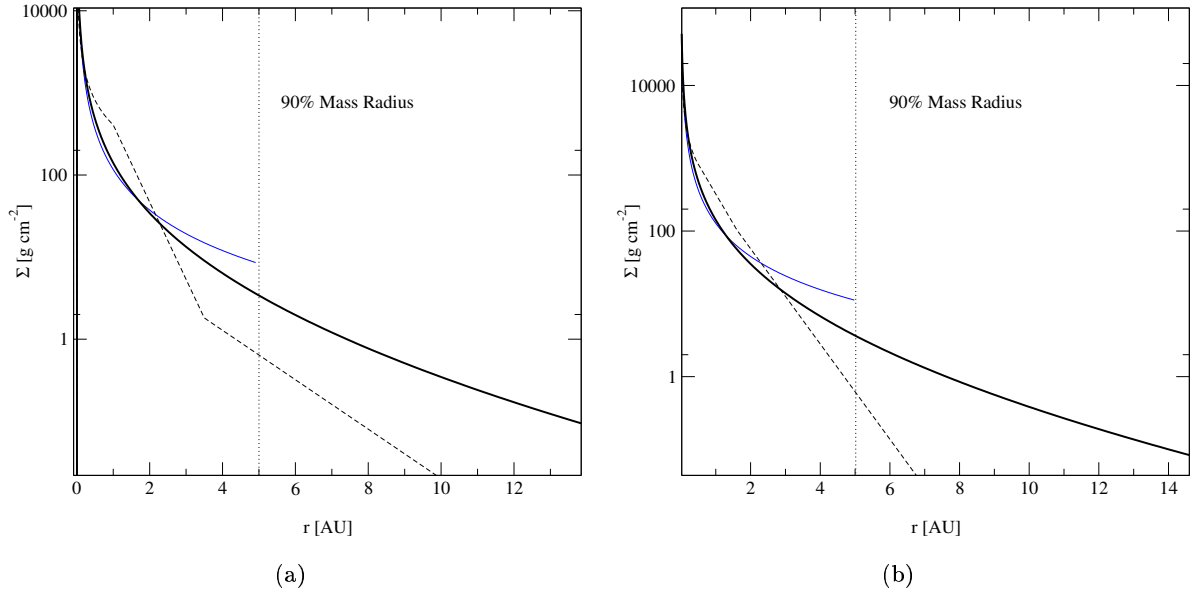

Figure 5.31: Radial Surface density profiles at a time of $\approx 2.5 \cdot 10^5$yr (solid line) together with their initial profiles (dashed line), plotted semi-logarithmically. Shown are the profiles for a disk with a steep initial profile ($a_1 = 0.064$) and $r_{min} = 5$AU (a), and a flatter profile ($a_1 = 0.16$) with $r_{min} = 2.3$AU (b). The disk are evolved at an ambient temperature of $T_{amb} = 20$K. The blue solid line represents the power-law profile of the steady, constant temperature disk solution of D'Alessio et al. (1998). The parameters were chosen that both disks have initially the same mass.

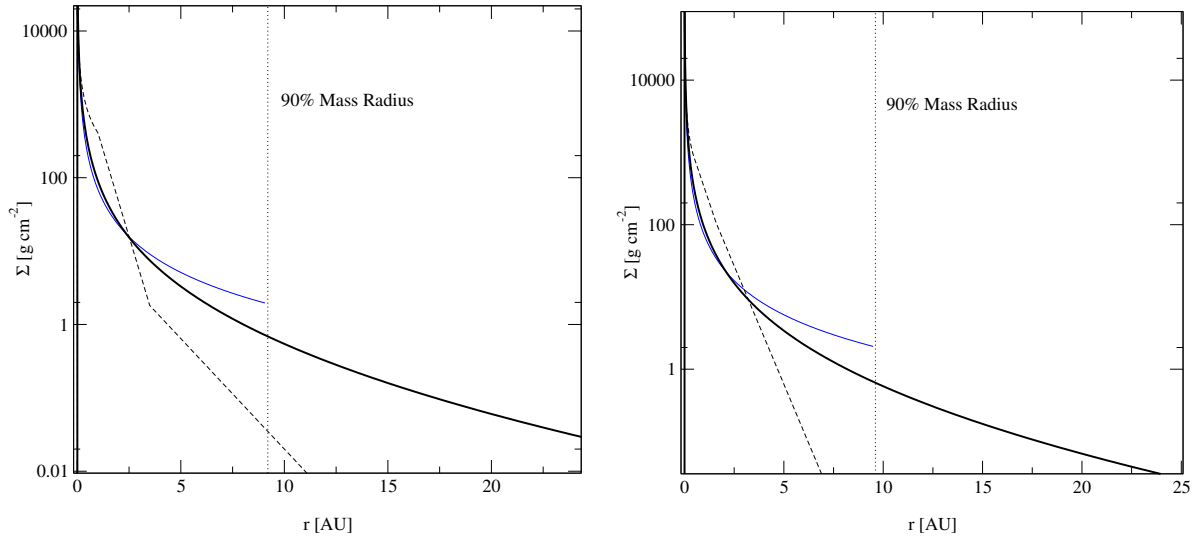

Figure 5.32: Radial Surface density profiles at a time of $\approx 5 \cdot 10^5$yr (solid line) together with their initial profiles (dashed line), plotted semi-logarithmically. Shown are the profiles for a disk with a steep initial profile ($a_1 = 0.064$) and $r_{min} = 5$AU (a), and a flatter profile ($a_1 = 0.16$) with $r_{min} = 2.3$AU (b). The disk are evolved at an ambient temperature of $T_{amb} = 20$K. The blue solid line represents the power-law profile of the steady, constant temperature disk solution of D'Alessio et al. (1998). The parameters were chosen that both disks have initially the same mass.

fitted with one exponential function, but it is rather similar to the asymptotic solution of the viscously spreading ring for large radii, as shown in Lynden-Bell & Pringle (1974), although in our case it is not identical, because ν is not constant. We also find that at a time $t = 2.5 \cdot 10^5$yr and later the two, initially different, profiles can now hardly be distinguished.

Therefore, we come to the conclusion that after $1 - 2 \cdot 10^5$yr any signatures of the initial profile vanish. This is also true for our largest disk with $r_{min} = 17.5$AU that evolve on larger time scales (see eq. 5.5). At later times, an outer disk profile similar to the viscously spreading ring for large radii develops which is also the disk profile one would expect from isolated disks (Hartmann et al., 1998). Therefore, directly from the structure of the disk the signatures of a close collision can only be observed within the first 10^5yr after the encounter.

5.4.4.4 Estimated Life-Time of Brown Dwarf Disks

The limit to detect active accretion disks around Brown Dwarfs is given by the observability of the broad accretion components of the Hα-line profile, which currently means that only disks with an accretion rate larger than $\sim 10^{-12} \mathrm{M}_\odot \cdot \mathrm{yr}^{-1}$ can be identified(Muzerolle et al., 2005). We, therefore, define the disk life-time as the time after which the accretion rate drops below this minimum value. As we mentioned in section 5.4.4.1, the value of the accretion rate in a viscous disk is dominated by the much hotter conditions at lower disk radii. As evolving the disk to a time of a few Myr and calculating the detailed temperature structure at every time-step is computationally too expensive, we assume a very high constant temperature throughout the disk with $T = 1000$K, which should overestimate the mass loss as explained in section 5.4.4.1. This allows us to integrate the non-dimensional form of equation 5.4 for different profiles and then scale the results for each of our post-encounter disks according to equation 5.5.

Fig. 5.33 shows the fraction of Brown Dwarf disks with a life-time larger than a given value for two different limiting accretion rates (left panel) as well as the distribution of accretion rates at a time of 1Myr. As it can be seen, we find no Brown Dwarf disk in our sample with a life-time larger than 2.5or 5Myr (depending on the detection limit) and the majority of our disks have life-times less than 1Myr. Such low life-times are in direct contradiction to the observations of Sterzik et al. (2004) who find an active accretion disk around a Brown Dwarf with an age of ≈ 10Myr.

On the other hand, Kenyon et al. (2005) suggest a typical time-scale for Hα-emission to become undetectable of less than the age of σOri (3-7 Myr). Although this would roughly agree with our results, our accretion rates at earlier times similar to the age of Taurus or IC-348 (both $\approx 1 - 3$Myr) appear to be very low compared to the observed accretion rates of Brown Dwarf disks in Muzerolle et al. (2003) which are mostly above $1 \cdot 10^{-11} \mathrm{M}_\odot \cdot \mathrm{yr}^{-1}$. For our disks we find that only 4% have accretion rates larger than $1 \cdot 10^{-11} \mathrm{M}_\odot \cdot \mathrm{yr}^{-1}$ and none with $\dot{M}$ larger than $4 \cdot 10^{-11} \mathrm{M}_\odot \cdot \mathrm{yr}^{-1}$ at an age of 1Myr. It, therefore, seems that in our model, we can only account for Brown Dwarfs with very low accretion rates.

The overall disk fraction among Brown Dwarfs at an age of 1Myr seems also much lower than observed in star-forming regions with similar age (e.g. Jayawardhana et al., 2003).

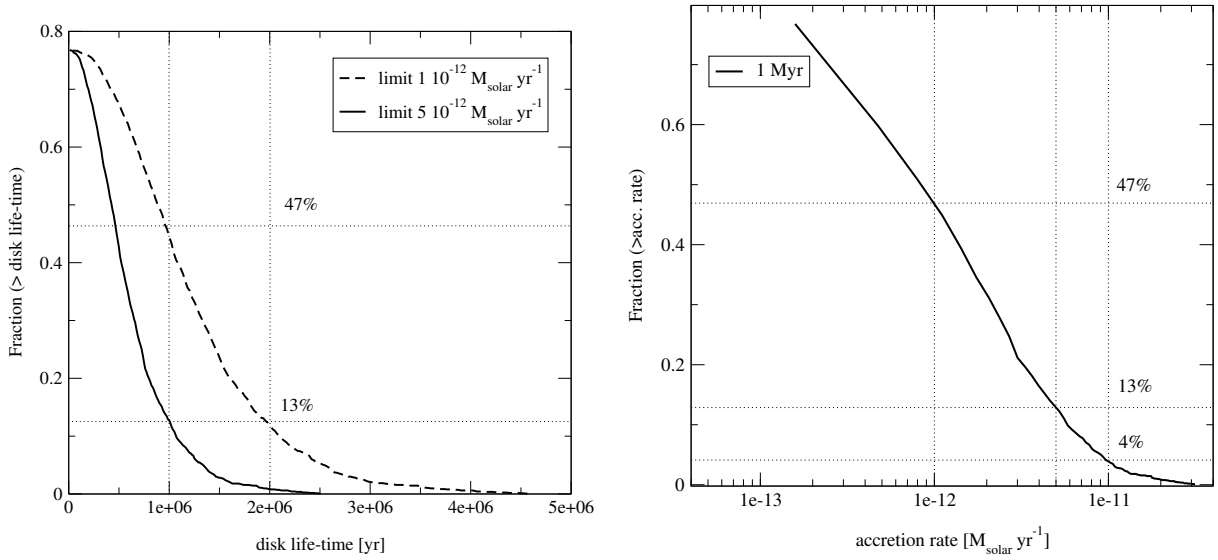

Figure 5.33: Fraction of Brown Dwarf disks with a life-time lager than a given value, for two different limiting accretion rates (a). Panel (b) shows the fraction of Brown Dwarf disks with an accretion rate larger than a given value at a time of 1Myr. Encounter of the 'exchange' type (see section 5.2) have been assumed to produce too small disks to be considered here.

Here we find that at 1Myr only 13% of the disks should have detectable accretion signatures (assuming $5 \cdot 10^{-12} \mathrm{M}_{\odot} \cdot \mathrm{yr}^{-1}$ as the detection limit), while the disk fraction in Taurus, IC 348 and Cha I is $\approx 50\%$(Jayawardhana et al., 2003). This difference can, however, be explained if one considers that disks are more easily detected than accretion signatures (Natta et al., 2004). Therefore, the number of confirmed substellar accretors is generally much lower than the number of detections of circumstellar disks. If we assume that the seemingly non-accreting Brown Dwarf disks are accreting ones, but with accretion rates lower than $5 \cdot 10^{-12} \mathrm{M}_{\odot} \cdot \mathrm{yr}^{-1}$ down to $1 \cdot 10^{-12} \mathrm{M}_{\odot} \cdot \mathrm{yr}^{-1}$, then one can easily see from Fig. 5.33 (a) that for this lower detection limit we get about the same disk fraction as actually observed. However, this result should be taken with some care, as we implicitly assumed that the observed disks in these clusters have ages of exactly 1Myr. If they turn out to be only a few 10^5yr older, than such a high fraction cannot be reproduced with our model. This is especially true as the age spread of the Brown Dwarfs in Taurus and Cha I is of the order of 2Myr (Jayawardhana et al., 2003; Barrado y Navascués, 2005). In addition, the number of accretors, i.e. Brown Dwarf disks with $\dot{M} > 5 \cdot 10^{-12} \mathrm{M}_{\odot} \cdot \mathrm{yr}^{-1}$, is for Cha I at $(28 \pm 6)\%$ (Natta et al., 2004), which is more than twice as much as we predict from our model.

It, therefore, seems to us that the accretion rates of our post-encounter disks at an age of $\approx$ 1Myr is much lower than has actually been observed in low-mass star-forming regions. This would further imply that, if all Brown Dwarfs form by ejection in accreting triple systems then the fraction of these systems that produce the very close binaries must be less or equal the fraction of Brown Dwarfs around which disk material was detected but not any accretion signatures. However, due to the rather large age spread of the observed objects and the strong time dependence of disk fraction in our model, we do not want to give any numeric constraints on the close Brown Dwarf binary fraction for any particular star-forming region, as it would be highly uncertain. Instead, a much more detailed comparison, taking into account the age of each individual observed object and the, hopefully, well constraint accretion rate close to $1 \cdot 10^{-12} \mathrm{M}_{\odot} \cdot \mathrm{yr}^{-1}$ could constrain our model much better.

Nevertheless, we want to remind at this point, that our model underestimates the disk fraction in many ways, with two being most significant: first, we evolve the disks at the maximum temperature, which should, in reality, decrease significantly with time, reducing the mass loss and therefore extending the life-time of our disks; second, compared to collapse calculations of Lin & Pringle (1990), our disks have rather low initial surface densities Σ_0 , and this by almost a factor of 4. Therefore, it seems plausible to us, that the disk fraction can be significantly higher at later time for more realistic initial conditions, which would in turn also increase the accretion rates and bring them much more in line with observations.

5.5 Summary and discussion

In this chapter we investigated disk collisions in triple systems and applied these results to disk collisions in accreting triple systems that produce Brown Dwarfs by ejection and estimated the sizes and life-times of these strongly perturbed disks around the ejected Brown Dwarfs.

Different from two-body disk encounters, we find that disk encounter in triple systems can no longer be sufficiently characterized by encounter distance and eccentricity of the perturber

orbit, as the disk in a close triple approach is strongly influenced by the motion of two bodies, instead of only one. We, therefore, introduced a simple parameterization that considers this fact and consists of the ratio of the closest encounter distances to each of the perturbers, r_1/r_2, and the minimum value of r_1 and r_2, r_{min}. For larger values of r_1/r_2 we would expect our results to be very different from two-body disk collisions, while for lower values our results should be rather similar to the two-body case.

From our disk collision simulations we find that, in most of our recircularized post-encounter disk profiles there are three distinct regions, a power-law region in the innermost disk and two regions further outside where the surface density drops off exponentially with different half-width values. The extent of these regions is determined by r_{min}, while only the half-width value of the middle region depends also on r_1/r_2. We find for low values of r_1/r_2 that the disks are much flatter than for larger values, which is reflected by a larger half-width value of the exponential drop-off in the middle region. From these data we constructed a model surface density profile that only depends on our encounter parameter r_{min} and r_1/r_2. We then used this model and calculated disk radii, relative to r_{min}, and relative disk masses in order to compare to the two-body results of Hall (1997).

Intuitively one would expect that these results converge for low values of r_1/r_2, as mentioned above. However, for low r_1/r_2 we find that $r_{90\%}$ for our disks is twice as large as the value of $r_{90\%} = 0.5 r_{min}$ obtained by Hall (1997), while for larger r_1/r_2 it surprisingly reaches quickly $r_{90\%} = 0.5 r_{min}$. On the other hand, for the disk masses we find that for lower r_1/r_2 the results are comparable to the two-body results while the disk masses are quickly decreasing for larger values of r_1/r_2, as in the latter case there are two encounters with comparable strength. Together with the larger disk radii this has the effect that in a triple encounter either less mass is distributed over the same disk area, or the same amount of material is distributed over a larger area, compared to disks from two-body encounters. It follows that, disks after triple encounters have flatter radial profiles and are much less concentrated than after two-body encounters.

The reason for the much flatter profile is the fact that in a triple encounter the ejected body is after the encounter dramatically slowed down when the two perturber form the final binary. This causes much of the material, that was initially unbound, to be re-captured by the ejected body. Because this material has also a larger specific angular momentum its recircularized radius will also be larger, causing the flatter disk profile. Here we want to note, that this process is not specific to disk collisions in triple encounters but also applies to encounter in higher order multiple systems.

Our model of the post-encounter surface density disk profile allowed us to make predictions about the disks around Brown Dwarfs that were ejected from accreting triple systems. It was thus possible to investigate the problem if we can form the close Brown Dwarf binaries as obtained from our earlier simulations, while still having disks with life-times as inferred from observations.

As we applied our disk model to the very close encounter in accreting triple systems we found that after such collisions the disks have very small sizes, with only 2.5% of the Brown Dwarf disks having $r_{90\%}$ larger than 2.5AU. Consequently their masses are extremely low, with the majority of the Brown Dwarf disks having $M < 1\mathrm{M_J}$. Although, these values are within

the range of masses determined for observed Brown Dwarf disks (Klein et al., 2003), these observed disks are, however, already at an advanced age ($\approx$ 1Myr). Our disks, on the other hand, have ages less than $\approx 10^5$yr, as in the ejection scenario the decay happens well before one free-fall time of the molecular cloud core (Reipurth & Clarke, 2001). Therefore, we expect that most of our disks have much lower masses at a time of 1Myr. It must, however, be mentioned, that we fix our disk masses by requiring the initial disk before the encounter to have a mass lower than 1/10 times the mass of the central Brown Dwarf. This is because, we simulated disk encounter for low-mass disks, and as soon as the disks become more massive the self-gravity of the disks becomes important and our results from section 5.3 are no longer applicable. Therefore, we think Σ_0 can be in principal much higher than we assumed, and it should be possible that the disks had initially higher masses and thus the post-encounter disks would also be much more massive, which could better fit the observed disk masses.

In order to relate our results to observations of Brown Dwarf disks we let our post-encounter disks evolve viscously until a time of a typical age of observed young Brown Dwarfs. We found, that the outer disk profile is mainly dominated by the temperature of the ambient interstellar cloud medium and, therefore, the disks expand much slower for cooler, low-mass star-forming regions like Taurus than hotter ones, similar to the Orion Nebular cloud. We found that only in cooler low-mass star forming regions we can expect that the sizes of disks around ejected Brown Dwarfs are, on average, significantly smaller than they are expected around T Tauri stars, provided the Brown Dwarfs have an age of less than 1Myr. We also investigated, if the profiles of the ejected disks can be used to determine if the disk suffered a close encounter which is necessary to form a close Brown Dwarf binary. Our results show, that the peculiar signatures of the initial disk-profile vanish on time-scales usually much less than $2 \cdot 10^5$yr even if one assumes a rather cool environment. After that time the outer profile is much flatter than initially and does not appear to be strongly truncated. It should be, therefore, rather difficult to distinguish such a profile from that of an isolated disk observationally.

From this we follow further, that only the disk sizes, but not the disk profiles, of disks around very young Brown Dwarfs in cool low-mass star-forming region could be used to distinguish between a formation by ejection and a more isolated formation. However, one should also note that in our particular case the encounters that truncate the disks are very close, owing to the rather strong decrease of the total energy for the accretion-of-gas-at-rest approximation, as shown in section 4.2.2. A less stronger decrease in total energy, as e.g. for the gas-in-motion approximation (see Fig.4.1), would lead to, on average, larger encounter distances and, therefore, to larger disks. Thus disk sizes much larger than we found at an age of less than 1Myr do not generally rule out a formation by ejection. All we can say here is that from our model the existence of mainly very close Brown Dwarf binaries in a star-forming region implies very small disk sizes around ejected Brown Dwarfs at an age of less than 1Myr.

So far the sizes of disks around Brown Dwarfs are not very well constrained by observations and only the detection of millimeter dust emission (Klein et al., 2003) has shown that they must extend to larger radii where the disk temperature is low ($10 - 20$K) and, therefore, dominated by the ambient medium. This means in our case a radius larger than typically $\approx 1 - 2$AU. For the accretion rates and life-times of Brown Dwarf disks on the other hand, there is much more data available to compare our results with.

Using as definition of the disk life-time, the time where the accretion rate drops below $\sim$

$10^{-12}\mathrm{M}_{\odot} \cdot \mathrm{yr}^{-1}$(Muzerolle et al., 2005), we find from our simulations that there is no disk with a life-time larger than 5Myr, even if we apply our lowest threshold value for $\dot{M}$. Although this might seem to reflect the time scale for Hα-emission to become undetectable as mentioned in section 5.4.4.4, comparing the values of $\dot{M}$ at earlier times, it becomes clear that our model can only account for the lowest accreting Brown Dwarfs with $\dot{M}$ mostly less than $10^{-11}\mathrm{M}_{\odot} \cdot \mathrm{yr}^{-1}$ at an age of 1Myr. In addition, our disk-fraction at 1Myr with about 13% seems also to be too low compared to the observed fraction of $\approx 50\%$ in clusters at a similar age, like Taurus. However, as we find, this difference can in part be explained if we account for the fact that not in all Brown Dwarf disks accretion features have been detected. If we apply our lower threshold value for $\dot{M}$ we find a disk fraction that is very close to 50%. Still, our model cannot explain the rather high fraction of Brown Dwarf disks with much higher accretion rates than $5 \cdot 10^{-12}\mathrm{M}_{\odot} \cdot \mathrm{yr}^{-1}$ at an age of $\approx$ 1Myr.

On the other hand, we should also note here that the assumptions about initial conditions of our disks are rather "pessimistic". As we mentioned earlier, we had to restrict ourselves to low-mass disks just before the triple encounter, as otherwise these simulations would be computationally too expensive. However, from the collapse calculations of Lin & Pringle (1990) we find that these densities can be a factor of 4 larger than the one we assumed here. Such large values should make the masses of our post-encounter disks much larger and consequently their life-times as well as accretion rates. However, here we can only speculate about how the life-time increases, as we expect that the evolution of a triple system, where the disk's gravity can no-longer be neglected, is not only different from triple encounter without a massive disk, but should be also much more complex to treat systematically in order to obtain meaningful statistics, because of the much increased parameter space.

In addition to the low initial densities, we fixed the temperature at all times to the maximum initial temperature which we obtained from the calculations in section 5.4.4.1. As mentioned earlier, the temperature in the inner disk will decrease with time for the more realistic model. Therefore, we overestimated the accretion rates at later times dramatically. It seems plausible to us that, if we assume a realistic temperature distribution, our disks will have significantly larger life-times. However, future simulations of the evolution of all our post-encounter Brown Dwarf disks need to show to what extent we can expect much larger life-times.

Given that we have chosen very conservative initial conditions and temperatures for our disks and that we still get a disk fraction of 13% at 1Myr, inspires confidence that in more realistic simulations we can have both, very close Brown Dwarf binaries and long lived accreting disks around Brown Dwarfs, although probably not as long lived as 10Myr, like the Brown Dwarf disk found by Sterzik et al. (2004). Currently, however, it seems that our disks around ejected Brown Dwarfs generally have too low accretion rates and life-times to account for most of the observed disks at ages of typical star-forming regions. This does not necessarily mean that Brown Dwarfs cannot have formed by ejection in these regions but excludes for many of these disks our initial conditions that produce the very close Brown Dwarf binaries observed in the galactic field.

5.6 Limitations and Future Prospects

In this section we want to remind the reader that our model is based on many simplifying assumptions. This is especially with regard to the initial conditions of the disk before the encounter, as already pointed out previously. Here we want to make some additional remarks that have been left out in the discussion so far.

First, we should remind that in the entire chapter we only considered disk collisions in decaying triple systems, where the triple systems had zero total angular momentum. Although we do not believe that our results regarding the disk structure change dramatically if rotation is taken into account, the effect of an initial uniform rotation of the triple system on the resulting disks around the ejected body should, nevertheless, be quantified in a future study. Also, the effect of non-coplanar encounter, where the disk mid-plane is no longer in the orbital plane of the triple system, should be investigated, as it might change the disk structure as well as the amount of material that gets stripped off the disk. However, we think that these effects should not change our main results significantly, whereas the following might be much more important.

We chose, for simplicity reasons, a $\Sigma \propto 1/r$-profile but it is currently unclear how the disk will evolve during the interaction in the triple system and how its profile will be before the last encounter. As we already mentioned, this would require to investigate the much larger parameter space of encounter that do not lead to escape. Even if we restrict ourselves to the last encounters before the break-up of the system, we find, that it becomes already difficult to describe the outcome of a disk collision in terms of only two encounter parameter, as can bee seen by the rather large errors of our model parameter in Fig. 5.13. Therefore, to investigate disk collisions in a systematic way during the whole interaction in a bound triple system and determining the structure of the remaining disk in dependence on the properties of these triple systems is already a large computational challenge, even without considering the permanent infall of disk material due to the collapse of the molecular cloud core.

Another simplifying assumption in our model is, that the disk material is recircularized after the encounter. This assumption is based on results of simulations that treat the viscous evolution in a very simplified way (Clarke & Pringle, 1993). Much more detailed hydrodynamical simulations of perturbed disks need to justify this. Such calculations then need to take into account the non-Keplerian velocity profile of these disks, caused by the eccentric orbital motion of the disk material, but also the non-axis-symmetric structure, which makes two-dimensional simulations necessary. These investigations are very important for the further evolution of the disk, as they determine the time-scale of recircularization. In our simulations we assumed that this time-scale is much shorter than the time-scale the disk expands. We, therefore, started our disk evolution calculations with a completely recircularized disk. In reality we expect that recircularization could, in principal, take place on longer time-scales which causes a competition between viscous expansion and contraction due to recircularization. It is, therefore, possible that the disks do not become that much concentrated, which in turn should reduce the accretion rate, as there is less material in the inner regions and $\dot{M} \propto \nu\Sigma$. From this it follows that longer recircularization time-scales will increase the life-time of our disks, whereas our model, once again, tends to reduce it.

Finally, the value of the viscosity parameter α is still rather uncertain and we can only say here that our value chosen seems to be reasonable based on MHD simulations of Abramowicz et al. (1996); Brandenburg et al. (1996). This seems even more so as our disks have rather low surface densities and can be easily ionized by cosmic X-rays, making ideal MHD applicable (Hubertus Klahr, private communication). Further constraining the value of the viscosity parameter is, however, vital for the determination of the life-time of our disks, because increasing it by only a factor of 2 would have the same effect as increasing the temperature of the inner disk by the same factor, which would reduce the life-time of our disks dramatically.

For the future we plan to resolve at least some of these issues. The less complex task seems to us, of course, to calculate the evolution of all our disks with the more realistic temperature profile to get a better estimate of the life-time of our disk. Then we should determine the time-scale of recircularization of the perturbed disk material. Although, it is computationally rather challenging, as we now have to carry out two-dimensional simulations, one should already be able to estimate the time-scale of recircularization after calculating a few extreme cases of perturbed disks.

On contrary, the investigation of the disk structure during the interaction in a triple system is much more complex and challenging, both to do systematic as well as computationally. First, the encounter parameter have to be re-determined for triple encounter that do not lead to decay, which is not so challenging, but then it needs to be shown that the outcome of disk collisions in such encounters can really be sufficiently described by only two parameter or if one needs to consider more parameter. Second, and more importantly, the disks are very unlikely to be of low-mass compared to the masses of the central object at the beginning of the simulation, as the infalling material will first accumulate in the disk (e.g. Lin & Pringle, 1990). This will significantly change the dynamics of the triple system and will probably also have an effect on the statistics and relative importance of the encounter parameters. In addition, as the disks are no longer of low mass, pressure forces and self-gravity need to be considered during the calculations which is already a challenging task for isolated disks and even more so for a parameter study. Therefore, such a study seems not tractable to do in the near future but higher resolution runs of collapsing, turbulent, molecular clouds, similar to Bate & Bonnell (2004), could give already a glimpse on what to expect, although, in absence of a realistic thermodynamical treatment of the disk, needs to be taken with some care.

Chapter 6

Conclusions

In this thesis we investigated the influence of accretion and gas interaction on the decay of gravitating triple systems and its implications on the viability of the ejection scenario as Brown Dwarf formation scenario. We carried out N-body calculations where the bodies are gaining mass according to a given accretion rate and derived statistics of escaping Brown Dwarfs and Brown Dwarf binaries and compared these to our analytical model. For the integration of motion we used a modified chain regularization routine that also allowed for mass growth of the fragments during their gravitational interaction.

We considered the kinematics, the abundance as well as the binary properties of the ejected fragments in dependence of the relative motion of the accreted gas with respect to the bodies. In these calculations we treat the gas interaction in an approximate fashion by specifying *ad hoc* the momentum the accreted mass adds to the stellar fragments. This modeling of dynamical interaction of the fragments allowed for a better statistical description of the resulting single and binary Brown Dwarf properties, because of the increased number of systems that can be integrated within a reasonable amount of time.

We also carried out simulations where the ejected body is surrounded by a mass- and pressure-less disk which allowed us to construct a model of the radial surface density profile that is fully determined by two encounter parameter of the triple collision that lead to decay. This model was then applied to determine the sizes and masses of disks around ejected Brown Dwarfs from accreting triple systems, while these triple systems also produce the very close Brown Dwarf binaries that match the observations. Furthermore, we investigated the viscous evolution of these strongly truncated disks in dependence of their inter-stellar environment, which allowed us to make predictions about the disk profiles, sizes and accretion rates at ages, at which young Brown Dwarfs in star-forming regions have been observed. From these simulations we further obtained lower limits on the life-time of accretion disks around ejected Brown Dwarfs and estimated disk fractions for typical low-mass star-forming regions, which we compared to observations.

6.1 Summary of Results

Our main results can be summarized as follows:

- We have shown that accretion and consequent shrinkage of triple systems increases the escape velocities significantly compared to non-accreting systems. The high velocities of Brown Dwarfs from our simulations should make it less likely to find them in star-forming clusters with a shallow potential well and a low escape velocity, but rather in an extended region around it, usually called the Brown Dwarf halo.

- In addition, a substantial fraction of Brown Dwarfs in our simulations have escape velocities which are rather low compared to typical escape velocities of low-mass star-forming clusters. These Brown Dwarfs should also share the same kinematics as the stars in the cluster, which would also agree with observations of low-mass star-forming regions.

- Because of ongoing accretion and consequent shrinkage of the systems, the binary separations are decreased by a factor of 5 compared with non-accreting systems and the median of the binary semi-major axis distribution in the case with accretion turned out to be up to 50 times smaller compared to the initial inter-particle distances. This reduction in scale made it possible to start with much larger fragment separations in order to obtain the observed close Brown Dwarf binaries.

- We were also able to represent the semi-major axis distribution of the volume limited sample of binary Brown Dwarfs of Bouy et al. (2003). In contrast to G-type binaries (Duquennoy & Mayor, 1991), the components in Brown Dwarf binaries seem to be very close and their semi-major axis distribution drops off steeply to both sides of the median. If this drop off to lower separations is confirmed observationally, it would provide some evidence, that tidal interactions might be less important for the evolution of Brown Dwarf binaries than they are for G-type stars.

- We have shown analytically as well as numerically that the probability of forming Brown Dwarfs should be high even for initially moderately compact systems. This is also true without considering competitive accretion, as competitive accretion will increase the number of Brown Dwarfs, which also our test simulations of unequally accreting triple systems indicate. Only for increasing accretion rates forming Brown Dwarfs by ejection seems less likely.

- Our analytical calculation showed that the reason why the ejection scenario is much more efficient than previously assumed lies in the shrinkage of the system, reflected by the time dependence of the mean harmonic size of the triple system. It turned out that the total energy is, depending on the amount of momentum transfer of the gas onto the bodies, strongly decreasing if this time-dependence is taken into account, while it is much less so if the system size remains constant. This convincingly explains the very different formation probabilities, resulting from our numerical calculations for the different kinds of momentum transport during mass growth.

- We found from our simulations of disk collisions in close triple encounter that the resulting recircularized disks are generally flatter and less massive than after similar two-body encounter with the same minimum encounter distance r_{min}. The difference in the disk profiles is related to the significant slow down of the ejected body after the close triple encounter, caused by the formation of the final binary, which causes some of the unbound high-angular momentum material to be re-captured by the ejected body.

- The disks around Brown Dwarfs ejected from accreting triple systems have very low masses mostly below $1\mathrm{M_J}$ and sizes typically less than 2AU at a time just after the ejection. These low masses are currently in contradiction to observations of Klein et al. (2003), considering that our disks will have lost a substantial amount of mass until they reach the age of the observed objects.

- A difference in disk size between disks around ejected Brown Dwarfs and Brown Dwarfs that might have formed similar to isolated T Tauri stars can only be expected in rather cool low-mass star-forming regions at an age less than 1Myr.

- Any signature of the initial post-encounter profile vanishes after $\approx 2 \cdot 10^5$yr and the disk does no longer appear to be strongly truncated. It should be then rather hard to distinguish it from a disk profile of an isolated disk that did not suffer a collision.

- The life-times of disks around ejected Brown Dwarfs, in our current model, do not exceed 5Myr. It seems, therefore, very unlikely that accreting disks around older Brown Dwarfs have suffered close triple encounter that also lead to the formation of very close Brown Dwarf binaries.

- Our model can currently only account for the accreting Brown Dwarfs with the lowest accretion rate mostly below $1 \cdot 10^{-11}\mathrm{M}_\odot \cdot \mathrm{yr}^{-1}$ at an age of $\approx$ 1Myr.

- The disk fraction of accreting Brown Dwarfs with accretion rates larger than $5 \cdot 10^{-12}$ is in our model too low to account for many of the observed disks in typical low-mass star-forming regions. From our model we can only conclude that the fraction of very close Brown Dwarf binaries must be less than the fraction of Brown Dwarfs around which disk material was detected but not any accretion signatures in those regions.

6.2 Discussion and Conclusions

Our results as laid out above have helped to arrive at a clearer picture of the consequences as well as the feasibility of the ejection scenario as Brown Dwarf formation scenario presented by Reipurth & Clarke (2001). This especially applies to the properties of Brown Dwarf binaries. In contrast to previous work, we found that the formation of close Brown Dwarf binaries, as observed in the galactic field (Bouy et al., 2003), might be a common byproduct of the ejection if the accretion process is not very competitive. Although Sterzik & Durisen (2003) come to similar binary properties without considering accretion during the interaction, their choice of the initial compactness of the multiple systems seems to be problematic for Brown Dwarfs, as it would require them to start on initial separations that are very close to the initial sizes of the opacity-limited fragments of about 10AU (compare to Bate et al., 2002a).

It seems, therefore, very likely that these Brown Dwarfs will merge to a single object, rather than interact like point-masses. We, on the other hand, have shown that the initial separation can be more than an order of magnitude larger to achieve the same compactness for binary Brown Dwarfs, if accretion and momentum transfer of the accreted gas is accounted for.

Therefore, in our model very close Brown Dwarf binaries can form under a much larger variety of initial separations than in similar models without accretion. This has also the consequence that the properties of molecular cloud cores have a larger influence on the outcome of the ejection scenario than just setting the initial conditions. This, in turn, means that from Brown Dwarf binary properties one cannot relate, in a simple way, to the initial separations of the multiple system they might have formed in. This is also reflected by the dependence of the total energy of triple systems (eqn. 4.12) , as it depends only linearly on the initial compactness of the system, given by the initial energy E_0, whereas its dependency on the accretion rate is much stronger.

However, from our simulation we cannot draw any conclusions about how efficient the ejection scenario can produce binary Brown Dwarfs, as we did not extensively explore the influence of competitive accretion. As we found from our test calculations, the higher the difference in the accretion rates between the members of the triple is, the lower is the number of Brown Dwarf binaries. From simulations of Bonnell et al. (1997) it turned out that the competitiveness of the accretion process also depends on the number of fragments in a multiple system, with smaller- N systems having a lower maximum mass ratio of their members at a given time than for larger- N systems. This would simply mean that it might be more likely to form Brown Dwarf binaries in triple rather than in higher order systems. In addition, observations of Brown Dwarf binaries indicate that their mass ratios are close to one (Bouy et al., 2003), supporting the idea that Brown Dwarf binaries could have formed in decaying accreting triple systems, where competitive accretion did not play a big role. However, this needs to be confirmed by more detailed hydrodynamical simulations.

Since we found initial conditions for our accreting triple systems that resulted in the close Brown Dwarf binary distribution that match the observations, we can further study the consequences for the single ejected Brown Dwarfs with the same initial conditions and compare these to observations of Brown Dwarfs in low-mass star-forming regions. This allows us then to speculate, if we could expect very close Brown Dwarf binaries in these regions, as so far only close Brown Dwarf binaries could be resolved at distances not greater than ≈ 105pc.

Considering the results of our simulations of disks around ejected Brown Dwarfs, the general impression is that currently the chances to find the very close Brown Dwarf binaries in low-mass star-forming regions as Taurus, IC348 and Chamaeleon are rather limited, as there seem to be too many Brown Dwarf disks with too high accretion rates. Therefore, a null-result for close Brown Dwarf binaries in these regions would be in complete agreement with the ejection scenario. If, however, there might be some close Brown Dwarf binaries much more detailed modeling is required in order to relate the number of very close Brown Dwarf binaries to the number of single Brown Dwarfs with accretion disks. Such modeling then needs to take into account the influence of competitive accretion and needs better constraints on the accretion rates as well as initial masses, when the fragments start to significantly interact with each other. This can only be done with fully hydrodynamical models of collapsing cloud cores, where the initial conditions are self-consistently obtained.

However, so far such models could not produce any close Brown Dwarf binaries and much more effort needs to be invested in order to understand why that is so. The other problem with such models is, that it is rather difficult to get meaningful statistics. Therefore, a refined approximative model based on the results of a few of such fully hydrodynamical calculations seems to be a good way to have both, sensible initial conditions and a good statistical description of the resulting distribution of Brown Dwarf properties. This would also lead to a much better understanding of the relation between initial cloud properties and the properties of the embedded accreting clusters.

We conclude that accretion of gas and the kinematic properties of the accreted gas during dynamical interactions strongly influence the abundance as well as the dynamical properties of Brown Dwarfs and, that the ejection scenario seems to be a promising scenario to produce both, close Brown Dwarf binaries as well as single Brown Dwarfs, whereas it seems less likely to find very long-lived accretion disks around them.

Bibliography

Aarseth, S. J., Anosova, J. P., Orlov, V. V., & Szebehely, V. G. 1994, Celestial Mechanics and Dynamical Astronomy, 60, 131

Abramowicz, M., Brandenburg, A., & Lasota, J. 1996, MNRAS, 281, L21+

Agekian, T. A. & Anosova, Z. P. 1990, Celestial Mechanics and Dynamical Astronomy, 49, 145

—. 1991, AZh, 68, 1099

Allen, L. E., Myers, P. C., Di Francesco, J., Mathieu, R., Chen, H., & Young, E. 2002, ApJ, 566, 993

Anosova, J. P. & Orlov, V. V. 1994, Celestial Mechanics and Dynamical Astronomy, 59, 327

Anosova, J. P. & Zavalov, N. N. 1981, Trudy Astronomicheskoj Observatorii Leningrad, 36, 109

Anosova, Z. P. 1986, Ap&SS, 124, 217

Anosova, Z. P. & Orlov, V. V. 1992, A&A, 260, 473

Anosova, Z. P., Orlov, V. V., Chernin, A. D., & Kiseleva, L. G. 1989, Ap&SS, 158, 19

Apai, D., Pascucci, I., Henning, T., Sterzik, M. F., Klein, R., Semenov, D., Günther, E., & Stecklum, B. 2002, ApJ, 573, L115

Armitage, P. J. & Clarke, C. J. 1997, MNRAS, 285, 540

Béjar, V. J. S., Martín, E. L., Zapatero Osorio, M. R., Rebolo, R., Barrado y Navascués, D., Bailer-Jones, C. A. L., Mundt, R., Baraffe, I., Chabrier, C., & Allard, F. 2001, ApJ, 556, 830

Béjar, V. J. S., Zapatero Osorio, M. R., & Rebolo, R. 1999, ApJ, 521, 671

Balbus, S. A. & Hawley, J. F. 1991, ApJ, 376, 214

Barrado y Navascués, D. 2005, Memorie della Societa Astronomica Italiana, 76, 348

Basri, G. 2000, ARA&A, 38, 485

Bate, M. R. & Bonnell, I. A. 2004, MNRAS, 728

Bate, M. R., Bonnell, I. A., & Bromm, V. 2002a, MNRAS, 332, L65

—. 2002b, MNRAS, 336, 705

—. 2003, MNRAS, 339, 577

Bell, K. R., Cassen, P. M., Klahr, H. H., & Henning, T. 1997, ApJ, 486, 372

Bell, K. R. & Lin, D. N. C. 1994, ApJ, 427, 987

Binney, J. & Tremaine, S. 1987, Galactic dynamics (Princeton, NJ, Princeton University Press, 1987, 747 p.)

Boffin, H. M. J., Watkins, S. J., Bhattal, A. S., Francis, N., & Whitworth, A. P. 1998, MNRAS, 300, 1189

Boldyrev, S., Nordlund, Å., & Padoan, P. 2002, ApJ, 573, 678

Bonnell, I. A., Bate, M. R., Clarke, C. J., & Pringle, J. E. 1997, MNRAS, 285, 201

—. 2001, MNRAS, 323, 785

Boss, A. P. 2001, ApJ, 551, L167

Bouvier, J., Stauffer, J. R., Martin, E. L., Barrado y Navascues, D., Wallace, B., & Bejar, V. J. S. 1998, A&A, 336, 490

Bouy, H., Brandner, W., Martín, E. L., Delfosse, X., Allard, F., & Basri, G. 2003, AJ, 126, 1526

Boyd, D. F. A. & Whitworth, A. P. 2005, A&A, 430, 1059

Brandenburg, A., Nordlund, A., Stein, R. F., & Torkelsson, U. 1996, ApJ, 458, L45+

Briceño, C., Luhman, K. L., Hartmann, L., Stauffer, J. R., & Kirkpatrick, J. D. 2002, ApJ, 580, 317

Bulirsch, R. & Stoer, J. 1966, Numerische Mathematik, 8, 1

Burkert, A., Bate, M. R., & Bodenheimer, P. 1997, MNRAS, 289, 497

Burkert, A. & Bodenheimer, P. 1993, MNRAS, 264, 798+

Chabrier, G. 2002, ApJ, 567, 304

Clarke, C. J. & Pringle, J. E. 1991, MNRAS, 249, 584

—. 1993, MNRAS, 261, 190

Close, L. M., Siegler, N., Freed, M., & Biller, B. 2003, ApJ, 587, 407

Comerón, F., Neuhäuser, R., & Kaas, A. A. 2000, A&A, 359, 269

D'Alessio, P., Canto, J., Calvet, N., & Lizano, S. 1998, ApJ, 500, 411

D'Angelo, G., Henning, T., & Kley, W. 2003, ApJ, 599, 548

Delgado-Donate, E. J., Clarke, C. J., & Bate, M. R. 2003, MNRAS, 342, 926

—. 2004, MNRAS, 347, 759

Duquennoy, A. & Mayor, M. 1991, A&A, 248, 485

Eislöffel, J. & Scholz, A. 2005, Memorie della Societa Astronomica Italiana, 76, 331

Elmegreen, B. G. 2000, ApJ, 530, 277

Forsythe, G. E., Malcolm, M. A., & Moler, C. B. 1977, Computer Methods for Mathematical Computations (Prentice Hall Professional Technical Reference)

Gizis, J. E., Reid, I. N., Knapp, G. R., Liebert, J., Kirkpatrick, J. D., Koerner, D. W., & Burgasser, A. J. 2003, AJ, 125, 3302

Goodman, A. A., Benson, P. J., Fuller, G. A., & Myers, P. C. 1993, ApJ, 406, 528

Goodwin, S. P., Whitworth, A. P., & Ward-Thompson, D. 2004, A&A, 414, 633

Hall, S. M. 1997, MNRAS, 287, 148

Hall, S. M., Clarke, C. J., & Pringle, J. E. 1996, MNRAS, 278, 303

Hartmann, L., Calvet, N., & Boss, A. 1996, ApJ, 464, 387+

Hartmann, L., Calvet, N., Gullbring, E., & D'Alessio, P. 1998, ApJ, 495, 385

Henning, T. & Stognienko, R. 1996, A&A, 311, 291

Hubeny, I. 1990, ApJ, 351, 632

Jayawardhana, R., Ardila, D. R., Stelzer, B., & Haisch, K. E. 2003, AJ, 126, 1515

Joergens, V. & Guenther, E. 2001, A&A, 379, L9

Kenyon, M. J., Jeffries, R. D., Naylor, T., Oliveira, J. M., & Maxted, P. F. L. 2005, MNRAS, 356, 89

Kirkpatrick, J. D., Reid, I. N., Liebert, J., Cutri, R. M., Nelson, B., Beichman, C. A., Dahn, C. C., Monet, D. G., Gizis, J. E., & Skrutskie, M. F. 1999, ApJ, 519, 802

Kirkpatrick, J. D., Reid, I. N., Liebert, J., Gizis, J. E., Burgasser, A. J., Monet, D. G., Dahn, C. C., Nelson, B., & Williams, R. J. 2000, AJ, 120, 447

Klein, R., Apai, D., Pascucci, I., Henning, T., & Waters, L. B. F. M. 2003, ApJ, 593, L57

Klessen, R. S. 2001, ApJ, 556, 837

Kobayashi, H. & Ida, S. 2001, Icarus, 153, 416

Koenigl, A. 1991, ApJ, 370, L39

Kroupa, P. & Bouvier, J. 2003, MNRAS, 346, 369

Kroupa, P., Bouvier, J., Duchêne, G., & Moraux, E. 2003, MNRAS, 346, 354

Kroupa, P., Tout, C. A., & Gilmore, G. 1993, MNRAS, 262, 545

López Martí, B., Eislöffel, J., Scholz, A., & Mundt, R. 2004, A&A, 416, 555

Lada, C. J. & Lada, E. A. 1991, in Astronomical Society of the Pacific Conference Series, 3–48676

Lada, C. J. & Lada, E. A. 2003, ARA&A, 41, 57

Landau, L. D. & Lifshitz, E. M. 1969, Mechanics (Course of Theoretical Physics, Oxford: Pergamon Press, 1969, 2nd ed.)

Lang, B. 2003, PhD thesis, University of Heidelberg

Larson, R. B. 1981, MNRAS, 194, 809

Larson, R. B. 1990, in ASSL Vol. 162: Physical Processes in Fragmentation and Star Formation, 389–399

Laughlin, G. & Bodenheimer, P. 1994, ApJ, 436, 335

Lin, D. N. C., Laughlin, G., Bodenheimer, P., & Rozyczka, M. 1998, Science, 281, 2025

Lin, D. N. C. & Pringle, J. E. 1990, ApJ, 358, 515

Liu, M. C., Najita, J., & Tokunaga, A. T. 2003, ApJ, 585, 372

Luhman, K. L., Rieke, G. H., Young, E. T., Cotera, A. S., Chen, H., Rieke, M. J., Schneider, G., & Thompson, R. I. 2000, ApJ, 540, 1016

Luhman, K. L., Stauffer, J. R., Muench, A. A., Rieke, G. H., Lada, E. A., Bouvier, J., & Lada, C. J. 2003, ApJ, 593, 1093

Lynden-Bell, D. & Pringle, J. E. 1974, MNRAS, 168, 603

Martín, E. L., Basri, G., Zapatero-Osorio, M. R., Rebolo, R., & López, R. J. G. . 1998, ApJ, 507, L41

Martín, E. L., Barrado y Navascués, D., Baraffe, I., Bouy, H., & Dahm, S. 2003, ApJ, 594, 525

Mikkola, S. & Aarseth, S. J. 1990, Celestial Mechanics and Dynamical Astronomy, 47, 375

—. 1993, Celestial Mechanics and Dynamical Astronomy, 57, 439

Moraux, E., Bouvier, J., & Cuillandre, J.-C. 2002, in SF2A-2002: Semaine de l'Astrophysique Francaise, 469–+

Motte, F., Andre, P., & Neri, R. 1998, A&A, 336, 150

Muench, A. A., Alves, J., Lada, C. J., & Lada, E. A. 2001, ApJ, 558, L51

Muench, A. A., Lada, E. A., Lada, C. J., & Alves, J. 2002, ApJ, 573, 366

Muzerolle, J., Hillenbrand, L., Calvet, N., Briceño, C., & Hartmann, L. 2003, ApJ, 592, 266

Muzerolle, J., Luhman, K. L., Briceno, C., Hartmann, L., & Calvet, N. 2005, ArXiv Astrophysics e-prints

Nakajima, T., Oppenheimer, B. R., Kulkarni, S. R., Golimowski, D. A., Matthews, K., & Durrance, S. T. 1995, Nature, 378, 463

Natta, A. & Testi, L. 2001, A&A, 376, L22

Natta, A., Testi, L., Muzerolle, J., Randich, S., Comerón, F., & Persi, P. 2004, A&A, 424, 603

Ostriker, E. C. 1994, ApJ, 424, 292

Padoan, P., Kritsuk, A., Norman, M. L., & Nordlund, Å. 2005, ApJ, 622, L61

Padoan, P. & Nordlund, Å. 2002, ApJ, 576, 870

—. 2004, ApJ, 617, 559

Pascucci, I., Apai, D., Henning, T., & Dullemond, C. P. 2003, ApJ, 590, L111

Pfalzner, S., Umbreit, S., & Henning, T. 2005, ArXiv Astrophysics e-prints

Pickett, B. K., Durisen, R. H., Cassen, P., & Mejia, A. C. 2000, ApJ, 540, L95

Press, W. H. 1993, Science, 259, 1931

Pringle, J. E. 1981, ARA&A, 19, 137

Reipurth, B. & Clarke, C. 2001, AJ, 122, 432

Salpeter, E. E. 1955, ApJ, 121, 161+

Semenov, D., Henning, T., Helling, C., Ilgner, M., & Sedlmayr, E. 2003, A&A, 410, 611

Shakura, N. I. & Sunyaev, R. A. 1973, A&A, 24, 337

Shampine, L. F. & Reichelt, M. W. 1997, SIAM J. Sci. Comput., 18, 1

Shu, F. H. 1977, ApJ, 214, 488

Skeel, R. D. & Berzins, M. 1990, SIAM J. Sci. Stat. Comput., 11, 1

Sterzik, M. F. & Durisen, R. H. 1995, A&A, 304, L9

—. 1998, A&A, 339, 95

—. 2003, A&A, 400, 1031

Sterzik, M. F., Pascucci, I., Apai, D., van der Bliek, N., & Dullemond, C. P. 2004, A&A, 427, 245

Stiefel, E. L. & Scheifele, G. 1971, Linear and regular celestial mechanics; perturbed two-body motion, numerical methods, canonical theory (Berlin, New York, Springer-Verlag, 1971.)

van Albada, T. S. 1968, Bull. Astron. Inst. Netherlands, 20, 57

Watkins, S. J., Bhattal, A. S., Boffin, H. M. J., Francis, N., & Whitworth, A. P. 1998a, MNRAS, 300, 1205

—. 1998b, MNRAS, 300, 1214

Whitworth, A. P. & Goodwin, S. P. 2005, Memorie della Societa Astronomica Italiana, 76, 211

Whitworth, A. P. & Zinnecker, H. 2004, A&A, 427, 299

Yorke, H. W. & Bodenheimer, P. 1999, ApJ, 525, 330

Yorke, H. W., Bodenheimer, P., & Laughlin, G. 1993, ApJ, 411, 274

Zapatero Osorio, M. R., Béjar, V. J. S., Martín, E. L., Rebolo, R., Barrado y Navascués, D., Mundt, R., Eislöffel, J., & Caballero, J. A. 2002, ApJ, 578, 536

Zinnecker, H., McCaughrean, M. J., & Wilking, B. A. 1993, in Protostars and Planets III, 429–495

List of Figures

Danksagung

Hiermit möchte ich allen danken, die mich während meiner Promotion privat oder auch beruflich unterstützt, angeregt, ermutigt und auch sonst dazu beigetragen haben, dass die hier nun vorliegende Arbeit vollendet werden konnte. Großen Dank gebührt ...
Many thanks go to ...

Meinem Betreuer Prof. Dr. Thomas Henning, für das sehr heiß diskutierte Thema meiner Arbeit, das mir dadurch auch viel Spaß bereitete. Desweiteren möchte ich ihm für die zahlreichen Diskussionen, Anregungen und Ideen sowie fuer seine Geduld und Unterstützung sehr herzlich danken.

Dr. Andreas Just für die Begutachtung meiner Arbeit und seiner Geduld.

Prof. Dr. Andreas Burkert für die Co-Betreuung und vor allem für die 'Initialzündung' dieser Arbeit. Ich möchte ihm auch sehr für seine Unterstuetzung und anregenden Diskussionen danken.

Prof. Dr. Rainer Spurzem für seine großartige Hilfe, ohne die diese Arbeit kaum so zustande gekommen wäre, und vor allem für seine Bereitschaft sich intensiv damit auseinanderzusetzen. Es war mir eine große Freude mit ihm zusammenzuarbeiten!

Dr. Seppo Mikkola for the invaluable discussion about how to implement accretion into the chain. Especially I would like to thank him for the development of the unique code, taylor-made for our purposes, which speeded up my whole thesis project significantly.

Dr. Hubertus Klahr für seine wertvollen Anregungen bezüglich der Thermodynamik der Scheiben und die tolle Zusammenarbeit, was die Arbeit wesentlich bereichert hat.

I would also like to thank Dr. Seppo Mikkola and Dr. Sverre Aarseth for giving our small N-body workshop during their visit in Heidelberg and for the interesting discussions we had.

Sami Dib for the many insights into the physics of the inter-stellar medium and for good company.

The whole theory group, old and new, for interesting discussions.

Konrad, Marc und Vernessa, für viel Ablenkung vom ernsten Doktorandenalltag und der guten Atmosphäre in unserem Zimmer.
Also thanks to all the others: Boris, Jens, Angela, Sabine, Michael, Bernd, Nadine, Thorsten, Stephan, Sigi, Daniel, Ilaria, Gerhard, Oliver, Alessandro, Andrea, Micaela and many more for sharing lunch and coffee and all the fun we had.

Johny Setiawan für seine hervorragenden Kochkünste, die ich wohl schwer vermissen werde!

Dem Berserker, dem Wizzard und dem Novizen, Goetz, Stefan und Andre, für die vielen gemeinsamen Skatabende, die legendären Spiele und den vielen Spaß den wir hatten.

Christian Maier, für seine unzähligen Partytipps und beharrlichen Überredungskünste in den Tanzkurs zu gehen, die nachhaltig (im positiven Sinne!) mein Leben veränderten (siehe nächster Punkt ;)

Shohreh ... Vielen Dank fuer die vielen glücklichen Stunden die ich mit Dir erleben durfte!

Meinen allergrößten Dank gilt meiner Familie und vor allem meinen Eltern fuer ihre Geduld und Unterstuetzung bei meiner Arbeit - und Shohreh die immer fuer mich da ist.